1-5-2017

Understanding and Overcoming Antifolate Resistance in Methicillin-resistant Staphylococcus aureus

Stephanie M. Reeve
University of Connecticut - Storrs, stephanie.reeve@uconn.edu

Understanding and Overcoming Antifolate Resistance in Methicillin-resistant *Staphylococcus aureus*

Stephanie Michelle Reeve, PhD

University of Connecticut, 2017

Resistance to every class of antibiotics has been identified clinically. The rapid development and spread of resistance is responsible for the diminished lifetime of many once efficacious therapeutics. Trimethoprim (TMP), a clinically important dihydrofolate reductase (DHFR) inhibitor, remains a first line treatment for *Staphylococcus aureus* infections but its continued use is threatened by the emergence of resistance. Identifying and understanding the mechanisms of trimethoprim resistance is crucial for the development for novel antibiotics to overcome the contemporary clinical resistances. Trimethoprim resistance is conferred through both the acquisition of mutations in the endogenous DHFR enzyme and of innately resistant enzymes. Guided by structure based drug design, a novel class of DHFR inhibitors, known as propargyl-linked antifolates (PLAs), has been developed to directly overcome trimethoprim resistance in *Staphylococcus aureus*. By doing this, we identified the contemporary mechanisms of antifolate resistance, developed a molecular understanding of reported and prospective mutational resistance mechanisms and generated a class of potent inhibitors against both wild type and TMP^R DHFR enzymes and *S. aureus* strains. In addition to their potent activity, these inhibitors also reveal unique binding and plasticity of both the inhibitor and co-factor binding sites, leading to the discovery of a novel NADPH configuration. In all, these efforts led to a comprehensive understanding of antifolate *S. aureus* and the development of potent inhibitors that overcome these resistance mechanisms.

Understanding and Overcoming Antifolate Resistance in Methicillin-resistant *Staphylococcus aureus*

Stephanie Michelle Reeve

B.S., DePaul University, **2011**

A Dissertation

Submitted in Partial Fulfillment of the

Requirements for the Degree of

Doctor of Philosophy

at the

University of Connecticut

2017

APPROVAL PAGE

Doctor of Philosophy Dissertation

Understanding and Overcoming Antifolate Resistance in Methicillin-resistant *Staphylococcus aureus*

Presented by

Stephanie Michelle Reeve, B.S.

Major Advisor

_____

Dennis L. Wright

Associate Advisor

_____

Victoria L. Robinson

Associate Advisor

_____

Jeffrey R. Aeschlimann

University of Connecticut
2017

This dissertation is dedicated to my family and friends for their unconditional support and in the memory of Dr. Amy Anderson, whose dedication and passion for science continues to inspire me.

Table of Contents

Chapter 1

The Clinical Burden of *Staphylococcus aureus*

Prior the introduction of penicillin in the 1940's, infections from minor cuts and scrapes could lead to blood poisoning and death. In fact, mortality rates of greater than 85% for blood infections during that time have been reported[1]. Penicillin, a beta-lactam antibiotic, was discovered by Alexander Fleming in London in the late 1920's and introduced to the clinic in the 1940's. Its discovery is regarded as one of the most significant advances in medicine. As the first accessible antibiotic, penicillin reduced the amount of infection related deaths and played a historic role in World War II, where the number of wounded soldier fatalities decreased significantly[1]. After its mass production and wide spread use, penicillin resistant bacteria began presenting a significant clinical burden in the mid 1940's and its spread to communal settings in the 1950's sparked the development of new antibiotics. The clinical introduction of methicillin in the 1960's reduced the burden of penicillin resistant bacteria, but like penicillin, resistance to methicillin developed rapidly[2]. The first methicillin-resistant *S. aureus* (MRSA) isolate was reported in England in 1961[3] and later appearing in the US in 1968[4]. Unlike penicillin, the development of methicillin resistance conferred broad resistance to the entire class of beta-lactam antibiotics[2].

Every year, approximately 700,000 people worldwide die of drug resistant infections[5]. According to the *Antibiotic Threat Report* released by the Centers for Disease Control released in 2013, more than 2 million Americans contract a drug resistant infection and at least 23,000 people die directly of the disease[6]. The urgent nature of drug resistance has prompted Presidential Priority in the 2016 Science and Technology Fiscal Budget in which it was declared that funding should be prioritized to the development of new

antibiotic resistance countermeasures including vaccines, small molecule inhibitors, synergists as well as implementing increased stewardship and surveillance measures[7]. The continued rise of antibiotic resistance and multi-drug resistant bacteria, a result of clinical and agricultural antibiotic misuse, is diminishing the efficacy of once powerful antibiotics. Therefore, the need to develop new, robust antibiotics is met with the need to understand the current state of clinical resistance and a strategy to overcome these resistances.

1.1 The Impact of *Staphylococcus aureus*

Methicillin resistant *Staphylococcus aureus* (MRSA), an opportunistic gram-positive bacterium, is the leading cause of invasive systemic infections, pneumonia as well as skin and soft tissue infections (SSTIs) worldwide. MRSA is the most common cause of healthcare-associated infections occurring during or shortly after inpatient care[8]. The Centers for Disease Control (CDC) reports over 80,000 invasive MRSA infections annually in the United States, more than 11,000 of these infections are fatal. The widespread and often critical nature of these infections prompted the CDC to classify drug resistant MRSA as a 'Serious Threat', as it poses a significant risk to public health[6]. As of 2005, *S. aureus* accounted for 18.7% of inpatient bacterial specimens and 14.7% of outpatient bacterial specimens. Of those strains, 55% of ICU isolates, 59% of general hospital and 48% of outpatient infections were resistant to methicillin[9].

MRSA infections can be healthcare (HA-MRSA) or community (CA-MRSA) associated; CA-MRSA and HA-MRSA are genetically distinct. Community associated MRSA can infect healthy populations that have no defined risk factors, specifically children and young adults. About 90% of CA-MRSA infections are uncomplicated skin and soft tissue

infections (SSTIs) such as cellulitis, however due to increased virulence often affiliated with these strains, they are able to advance in severity to necrotizing fasciitis, necrotizing pneumonia and even death[2,10]. The ability of CA-MRSA to cause severe infections is highly correlated with the presence of Panton-Valentine leukocidin (PVL) genes. Panton-Valentine leukocidin is a cytotoxin that causes leukocyte destruction, allowing for its evasion from immune system and allowing for infection advancement.[11,12]

Healthcare or hospital associated MRSA infections are considered those that occur in response to hospitalization and are often associated with biofilm formation[14]. Patients who have undergone surgery, dialysis, require a catheter or reside in a long-term medical care facility are said to be predisposed to HA-MRSA; if a patient does not possess one of these risk factors, they are considered to have a CA-MRSA infection[13]. However, since CA-MRSA has become an epidemic within health care systems, the epidemiological distinction between CA-and HA-MRSA isolates becomes complicated[8, 11]. HA- and CA-MRSA genotypes can be determined by identifying the staphylococcal chromosomal cassette *mec* (SCC*mec)*, a genetic feature common to all MRSA isolates and unique to the epidemiological lineage of the strains[12].

The antibiotic combination, trimethoprim and sulfamethoxazole, is the first line therapy for uncomplicated MRSA infections. However, these uncomplicated MRSA infections can also be successfully treated with non-penicillin antibiotics including tetracyclines, macrolides, fluoroquinolones, aminoglycosides and linezolid. Complicated SSTIs and systemic infections that require hospitalization are treated with intravenous vancomycin or daptomycin, both glycopeptide antibiotics; *with* the most severe and complicated infections requiring combination therapies[15]. In addition to having a major clinical

presence, the ability of MRSA to rapidly develop antibiotic resistance is especially concerning as it has significantly limited the available treatment options; clinical resistance to all aforementioned antibiotics has been reported in *S. aureus*.

1.2 The Folic Acid Cycle and Antifolates

1.2a The Folic Acid Cycle

Both trimethoprim and sulfamethoxazole belong to a class of antibiotics called antifolates as they inhibit enzymes within the folic acid cycle. Folate metabolism, via the folic acid cycle, is essential for the production of deoxythymidine monophosphate (dTMP), purine nucleotides, methionine and histidine; all of which are required for successful DNA replication and protein synthesis (Figure 1). During the cycle, *p*-amino benzoic acid and dihydropteroate pyrophosphate are consumed by dihydropteroate synthase for the generation of dihydropteroate. Dihydropteroate is then used for the synthesis of dihydrofolate (DHF) by reaction with dihydrofolate synthase. DHF is then reduced to tetrahydrofolate (THF) via the oxidation of NADPH by dihydrofolate reductase followed by a cyclization to N^5,N^{10}-methylene THF by a serine hydroxymethyl transferase. DHF is regenerated by the thymidylate synthase from N^5,N^{10}-methylene THF resulting in the methylation of dUMP to dTMP, a nucleotide used in DNA synthesis. Additionally, N^5,N^{10}-methylene THF is further reduced downstream of serine hydroxymethyl transferase by N^5,N^{10}-methyleneTHF reductase for methionine generation and N^5,N^{10}-methylenyl THF reductase for both histidine and purine nucleotide synthesis (Figure 1)[16]. Unlike bacteria where DHF is synthesized *de novo*, eukaryotic cells rely on dietary intake as their source of folate and actively transport folic acid across the plasma membrane via Reduced Folate Transporters (RFT). Once in the cell, DHFR reduces folic acid to dihydrofolate,

which then undergoes a second enzymatic reduction by DHFR to THF prior to completion of the cycle[17].

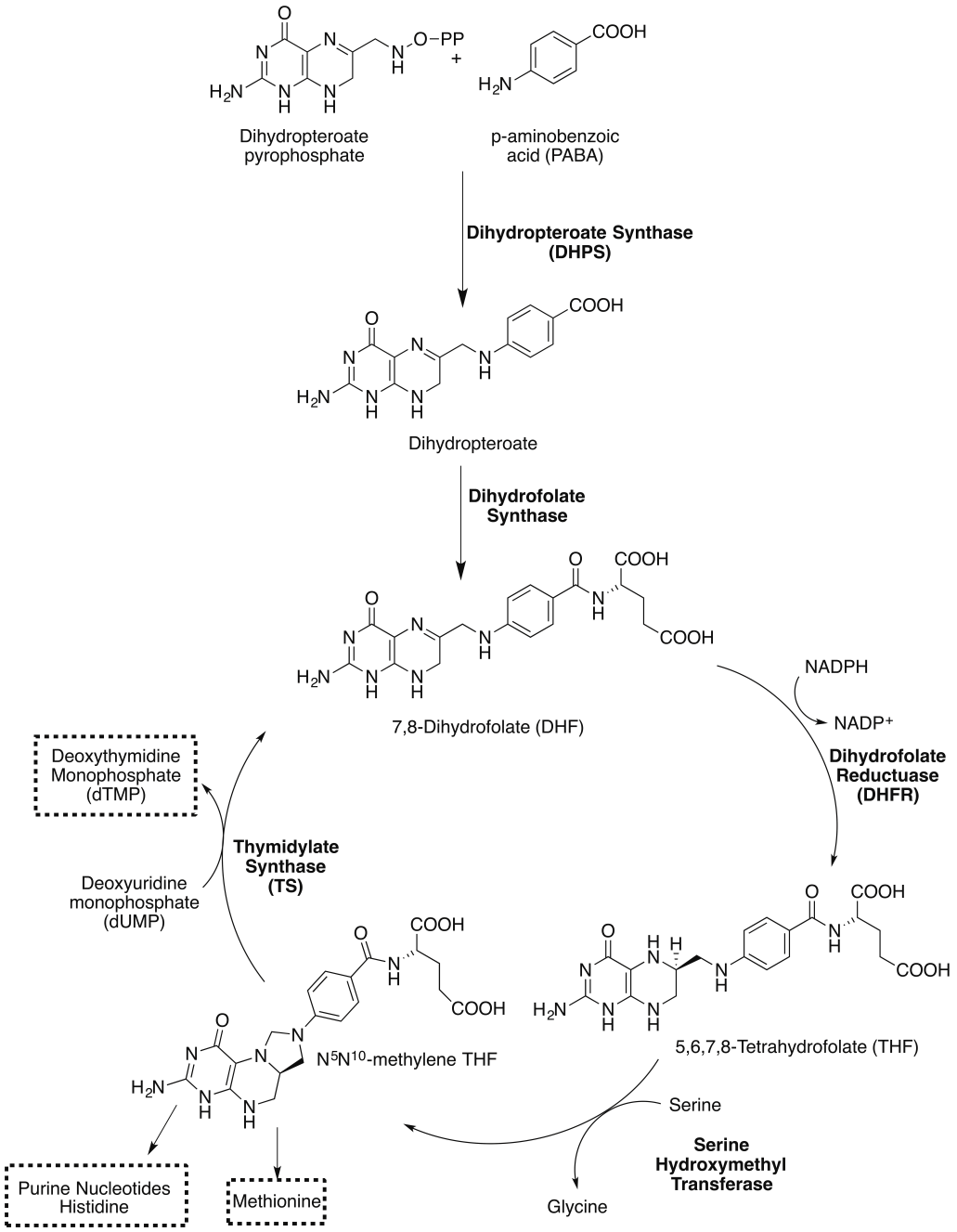

Figure 2 Bacterial folic acid cycle; enzymes are in bold and end products (dTMP, amino acids and nucleotides) are boxed[16].

1.2b Dihydrofolate Reductase

Dihydrofolate Reductase is an essential enzyme within the folic acid cycle responsible for the reduction of dihydrofolate to tetrahydrofolate via the oxidation of NADPH to $NADP^+$(Figure 2a). *S. aureus* DHFR, is 158 amino acids with a molecular weight of 17.4 kDa. The ternary protein structure features an 8- strand beta sheet surrounded by four alpha helices all connected through flexible loop regions. The substrate (DHF) forms several ionic interactions between the pterin moiety and the side chain of Asp 27 and backbone carbonyl of Phe 92 as well as a hydrophobic interaction with the side chain of Leu 28 and the amino benzoate ring (Figure 2b). The pterin amine group forms a hydrogen bond with a water molecule involved in an extensive water network coordinated throughout the protein as well extensive van der Waals interactions with the nicotinamide ring. Additionally, two crucial hydrogen-bonding interactions are formed between the glutamate tail and guanidinium moiety of the Arg 57 (Figure 2b)[18].

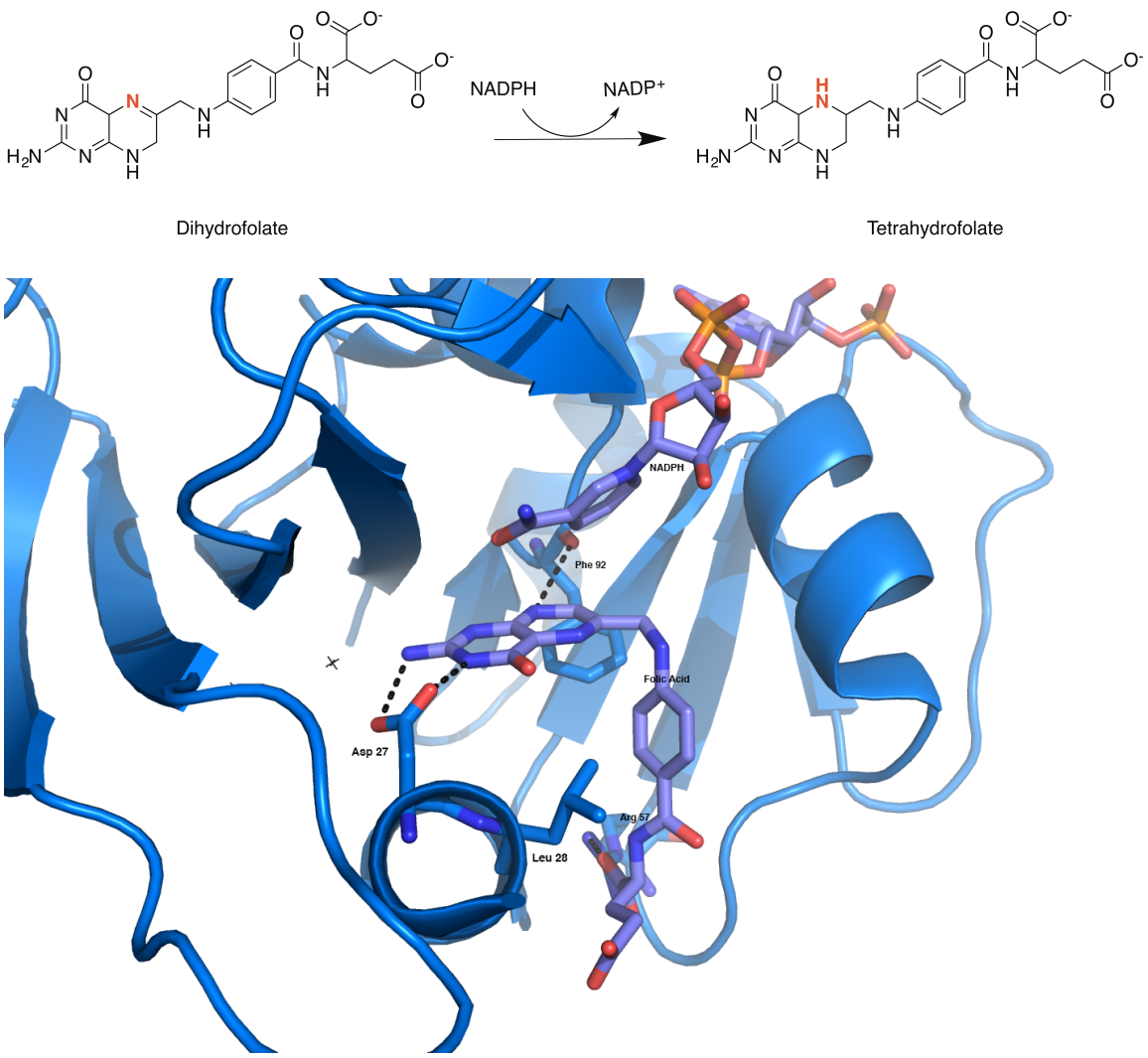

Figure 2 a) The mechanism of DHFR b) Folate and NADPH (purple) bound in the *S. aureus* DHFR (blue) active site. The amino acids and interactions made with DHF are highlighted (PDB ID: 3FRD).

During its catalytic cycle, DHF and NADPH form a ternary structure with DHFR. Upon reduction of DHF to THF through the oxidation of NADPH, $NADP^+$ is released from the active site leaving a binary complex of DHFR and THF. NADPH then binds the binary complex, releasing THF and allowing a new DHF molecule to bind, perpetuating catalysis[19]. After its release from the enzyme, THF is transformed into methylene-THF and continues through the folic acid cycle until it is regenerated by thymidylate synthase.

DHFR is the only source of THF for bacterial cells, therefore its inhibition results in arrested cell proliferation. As such, DHFR is a considered an essential enzyme and validated drug target exploited for the treatment of cancer, autoimmune disease as well as bacterial and parasitic infections.

1.2c Clinical Antifolates

Antifolates are inhibitors of folic acid enzymes including dihydrofolate reductase, thymidylate synthase (TS) and dihydropteroate synthase (DHPS). This class is clinically important for the treatment of cancers, infectious diseases and autoimmune disorders. Trimethoprim (TMP) is the only DHFR inhibitor approved for the treatment of bacterial infections (Figure 3). TMP is often prescribed in combination with sulfamethoxazole (SMX) and branded as Bactrim. Sulfamethoxazole is an antifolate targeting dihydropteroate synthase, an enzyme upstream from DHFR in the folic acid cycle. Both trimethoprim and sulfamethoxazole are bacteriostatic antibiotics, but together act synergistically resulting in a potent, bactericidal combination[16]. TMP has activity against gram-negative and gram-positive bacteria and TMP/SMX combination is first line treatment for CA-MRSA infections[20-23]. Trimethoprim is highly selective for susceptible, pathogenic DHFR over the human isoform (>8,600-fold) resulting in low-toxicity. In addition to its general tolerability, the combination is both orally bioavailable and available at minimal costs, increasing its clinical appeal[23]. In fact, prescriptions of TMP-SMX numbered more than 21 million in 2013, putting it in the group of top ten oral antibiotics prescribed in 2013[24].

Unlike beta-lactam antibiotics, whose drug class is made up of many generations of inhibitors, no major effort to generate second-generation antifolate antibiotics has been

successful. Iclaprim, a TMP derivative, showed potent activity against gram-positive bacteria including staphylococci and streptococci and went through clinical trials for complicated SSTIs and hospital acquired pneumonia infections[25-27]. However in 2009, Iclaprim was denied FDA approval upon completion of Phase III trials due a lack of efficacy and safety, as it possessed a potent inhibitory activity of hERG channel[28].

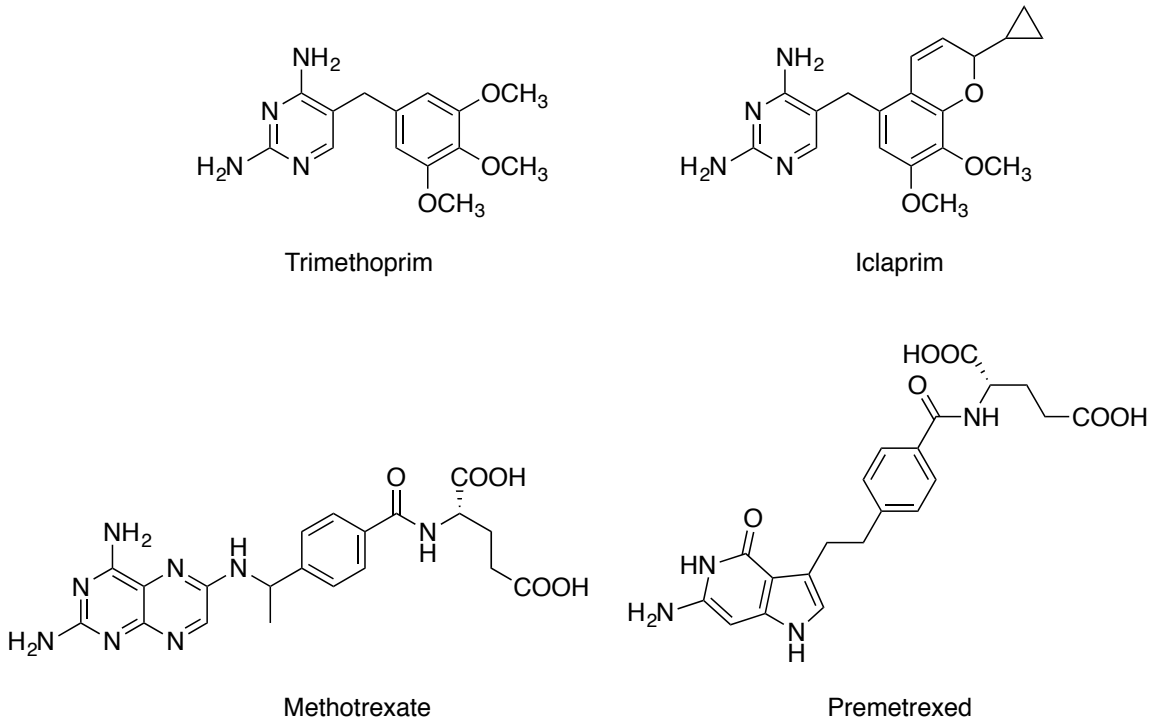

Figure 3 Structures of Clinically Approved and Relevant DHFR Inhibitors

In addition to its role as anti-bacterial therapeutics, DHFR has been exploited as the target for anti-cancer drugs, methotrexate (MTX) and pemetrexed, referred to as *Classical Antifolates*. Methotrexate is marketed for treatment of cancer, alone and in combination therapies, as well as for autoimmune disorders including rheumatoid arthritis, psoriasis and lupus. However, MTX is believed to work through different mechanisms of action for these non-cancer indications[29]. Pemetrexed is most recently approved DHFR inhibitor and is indicated for the treatment of non-small cell lung cancer and pleural mesothelioma

in combination with cisplatin[30]. In addition to DHFR inhibitition, pemetrexed also targets thymidylate synthase and GARFT, a ribonucleotide formyltransferase (Figure 3).

Like dihydrofolate, these classical antifolates possess a basic head group and a negatively charged glutamate extension that are critical for binding of the enzyme. Because of the structural similarities, these compounds mimic the binding motif of the substrate with a basic nitrogenous headgroup that forms strong contacts with an acidic residue in the active site and a glutamate tail that forms extensive ionic interactions with a basic amino acid[31-33]. As substrate mimics, classical antifolates often possess very high affinity for DHFR enzymes, with low nano-molar to pico-molar potency towards human and pathogenic enzymes including *E. coli* and *S. aureus*[34,35]. Like folate, classical antifolates are actively transported into eukaryotic cells though folate transporters. As bacteria synthesize folate through a *de novo* mechanism and do not possess folate transport capabilities, there is no mechanism by which these classical antifolates can penetrate bacterial cells and therefore show poor efficacy against these species regardless of the high enzyme affinity[29].

1.3 Antibiotic Resistance in *S. aureus*

Resistance to every class of antibiotics has been identified clinically. Drug resistance is responsible for increased morbidity, mortality and healthcare costs, estimates range from $20-35 billion in the US alone[6]. There are several major resistance mechanisms that affect antibiotics namely efflux of the drug from the cell, enzymatic modification of the drug, target mutations that reduce affinity of the drug, up-regulation of the target and permeability changes to the membrane. Methods in which a resistance-conferring enzyme is acquired by the cell, specifically an innately resistant target or a drug/ target

modifying enzyme, are often transferred between species on plasmid, mobile genetic elements, and incorporated into the chromosome via horizontal gene transfer. However, over-expression of the drug target or efflux pumps as well as changes in the drug target reducing drug affinity are a result of the accumulation of genetic mutations either in the gene's promoter region or within the gene itself[36].

1.3a Mutational Resistance

Point mutations in the target enzyme result in reduced affinity between the target and inhibitor by directly or allosterically hindering inhibitor binding. Fluoroquinolones, including ciprofloxacin and levofloxacin, target DNA gyrase (*gyrA*) and DNA topoisomerase IV (*grlA* and *grlB),* enzymes essential for DNA replication. The primary mechanism of resistance to fluroquinolones is a stepwise accumulation of mutations in these genes many of which are in the "quinolone resistance determining region" (QRDR) in the *gyrA* subunit[37]. Additionally, sulfamethoxazole resistance is conferred by the accumulation of up to 13 mutations in *folP,* the gene for DHPS, resulting in high level resistance[38]. Importantly, the formation of the mutations, as with other resistance mechanisms, must confer resistance without sacrificing the endogenous function of the enzyme, as enzymes or cells with reduced fitness are less likely to survive or be pathogenic.

Resistance conferred by reduced intercellular concentrations of antibiotics is achieved by efflux of the drug out of the cell and changes in cellular permeability reducing passive diffusion of the drug through the cytoplasmic membrane. In addition to mutational resistance, fluoroquinolones are also prone to resistance via efflux. *NorA*, an endogenous efflux system in *S. aureus*, can be over-expressed reducing the effective concentration within the cell to sub-lethal levels; inhibition of the efflux system can restore susceptibility

to these antibiotics. The overexpression of the efflux system is due to the accumulation of mutations in the gene's promoter sequence[39].

1.3b Plasmid Acquired Resistance Determinants

The ease with which bacteria transfer genetic elements from one species to another via plasmid genetic elements is responsible to the wide spread distribution of highly resistant genes. Once acquired by the cell, the genes encoded within genetic elements can be integrated into the chromosomal DNA through the process of horizontal gene transfer, although some plasmids contain mechanisms that allow gene expression without genomic incorporation. This mechanism of genetic material transfer is responsible for the introduction of innately resistant, drug modifying and enzyme modifying enzymes[31].

Resistance to methicillin and other beta-lactams in MRSA is conferred by the presence of a penicillin-resistant penicillin binding protein (PBP2a), encoded by the *mecA* gene. β-lactam antibiotics target the transpeptidase domain of endogenous penicillin binding proteins (PBPs) involved in bacterial cell wall synthesis. PBPs are essential to bacterial survival and the maintenance of cell wall integrity by acting as transpeptidases, cross-linking adjacent glycan strands in the cell membrane. PBP inhibition, via acylation by the β-lactam ring, halts cell wall synthesis while peptidoglycan autolysis continues and creates a compromised cell wall. The cells succumb to osmotic pressure, resulting in cell death[40]. PBP2a has low affinity for beta-lactam antibiotics allowing for uninterrupted transpeptidase activity in the presence of high beta-lactam concentrations. The *mecA* gene found on the SCC*mec* genetic element, is common in all MRSA strains and is required for its 'Methicillin resistant' designation[41]. The acquisition of innately resistant target enzymes is also responsible for antifolate resistance (*Chapter 1.3c*).

Additional beta-lactam resistance in *S. aureus* and other bacterial species is accomplished by the acquisition of β -lactamase enzymes. β-lactams bind β-lactamases and the nucleophilic active site acylates the β-lactam ring via a ring opening reaction. Once acylated, an active site water molecule hydrolyzes the acyl bond and the cleaved, deactivated β-lactam antibiotic is released from the active site

which deactivates the antibiotics by cleaving the lactam ring through an acylation mechanism, releasing an inactive form of the drug[42]. Similarly, plasmid-acquired enzymes can deactivate both macrolides and aminoglycosides. For example, bifunctional aminoglycoside deactivating enzymes, such as AAC(6')-APH(2"), have both acetyl transferase and phosphotransferase activity and have broad specificity towards the entire class of aminoglycosides[43]. These enzymes add acetyl and phosphate groups to specific alcohol substituents, reducing the affinity to its target, the 30S Ribosomal subunit. Similarly, *mph* isoforms phosphorylate a narrow spectrum of macrolid antibiotics such as erythromycin, which also targets the ribosome[44].

In addition to modification of macrolides by phosphorylation, *erm* enzymes, most commonly *ermA*, *ermB*, *ermC*, act as rRNA ribosomal methylases. These genes methylate the 23S ribosomal macrolide binding site, reducing the affinity between the inhibitor and binding site without sacrificing ribosomal function. The *erm* genes are inducible and affect a broader spectrum of macrolide antibiotics than the macrolide phosphorylase enzymes including erythromycin, azithromycin and clindamycin. These genes are also more common than the macrolide modifying enzymes in the clinic[45].

Resistance can also be conferred by biological changes to the target. For example, resistance to vancomycin, a first line antibiotic for complicated CA-MRSA and HA-MRSA, is conferred by changes in the cytoplasmic membrane. Vancomycin and other glycopepetides such as daptomycin bind the carboxy terminal of the D-Ala-D-Ala disaccharide penyapeptide cell wall precursor during peptidoglycan synthesis, blocking access for the transpeptidases required for cell wall generation. Resistance to vancomycin is conferred by the acquisition of a cluster of *van* genes that produce D-Ala-D-Lac disaccharides that are incorporated into the cell wall instead of D-Ala-D-Ala, drastically reducing the affinity of vancomycin[46]. While still rare, vancomycin-intermediate and vancomycin-resistant MRSA pose potentially devastating clinical consequences, as the treatment options for these strains are already very limited.

1.3c Antifolate Resistance

TMP/SMX resistance in *S. aureus* began to arise in the 1980s following its clinical introduction in 1968[47-49]. In the 1990s, two TMP^R mechanisms were identified as conferring clinical TMP resistance: point mutations in the endogenous DHFR gene, *dfrB*, and the acquisition of an innately resistant DHFR enzyme. A panel of point mutations, in both the allosteric and active sites of the enzyme, resulted in moderate to high-level resistance depending on the identity of the mutation. Noteworthy in this group was a Phe to Tyr mutation at the 98^{th} position that was isolated both alone and in combination with other minor, allosteric mutations. Alone, the F98Y mutation conferred up to 400-fold loss of affinity between TMP and the enzyme but the presence of H149R or H30N mutations contributed to even greater losses in activity. An interesting compensatory relationship between the two mutations suggested that the accumulation of the second mutation increased the fitness of the enzymes in addition to increasing its resistance[48].

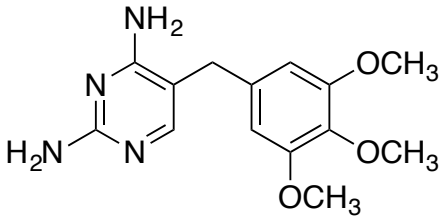

Trimethoprim

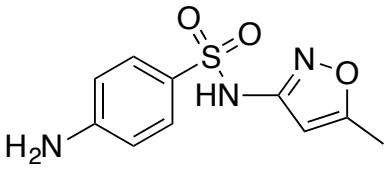

Sulfamethoxazole

Figure 4 The chemical structures of trimethoprim and sulfamethoxazole.

In addition to point mutations within the target, a horizontally transferred, plasmid-encoded resistant DHFR enzyme also appeared. The translated protein of the *dfrA* gene, often called S1 (but will be called DfrA here for clarity), was observed to confer high levels of TMP resistance at the enzyme level[47]. DfrA has three mutations in comparison to the TMP-sensitive *S. epidermidis* DHFR: V31I, G43A and F98Y; where F98Y is the major resistance determinant. The exact role of the F98Y mutation in TMP resistance is unknown, however studies suggest that it disrupts or destabilizes the binding of NADPH reducing its synergy with TMP, which is crucial for its potent activity[47]. More recently, two additional plasmid acquired TMP^R genes, *dfrG* and *dfrK*, have been identified. Both of these genes, which are genetically similar, confer high levels of TMP resistance and appear to be highly mobile as they have also been isolated in many *Staphylococci, Streptococci* and *Enterococci* species[50]. Not only has no recent survey of TMP^R MRSA isolates from US hospitals identified common molecular mechanisms of resistance, but the contribution of *dfrG* and *dfrK* was highly negated as clinically relevant despite reports[51]. Resistance for both pemetrexed and methotrexate has also been reported as a response to their use as anti-cancer agents. For pemetrexed, up-regulation of both

thymidylate synthase and dihydrofolate reductase have been reported[52,53]. Much more is known about methotrexate resistance, including decreases in active drug transport due to changes in the reduced folate carrier (RFC), efflux out of the cell, and up-regulation of DHFR[29].

1.4 Small Molecule Therapeutics to Overcome Drug Resistance

Exploiting new antimicrobial targets would temporarily reduce the clinical burden of drug resistant bacteria. However, no major classes of antibiotics have been discovered since the late 1980's, despite the introduction of linezolid and daptomycin in the early 2000's[54]. Efforts to overcome clinical antibiotic resistance are crucial for the continued, efficacious treatment of these infections. These efforts include the development of next generation inhibitors that are able to directly target the resistance mechanism and that are less susceptible to developing resistance. In order to accomplish this, a comprehensive understanding of the current and potential molecular mechanisms of resistance, through structural models and biochemical evaluations, is applied to the iterative process of development and evaluation.

Of the common mechanisms of resistance, only efflux, enzymatic modification and target mutations can be modeled using protein crystallography. Efforts to utilize crystal structures of efflux pump systems aim to elucidate the structural basis of substrate specificity, knowledge of this can lead to the design on inhibitors that are less susceptible efflux mediated resistance. Perhaps the two most successful examples of drug design to overcome resistances is the development of fluoroquinolones to overcome mutational resistance and β -lactam antibiotics that evade deactivation by β -lactamases.

1.4a Modification of the drug: β -lactamase enzymes

β-lactam antibiotics, including penicillins, cephalosporins and carbapenems (Figure 2a), have a broad spectrum of activity and are often used as a staple of therapy in clinically relevant infections caused by both Gram-positive and Gram-negative bacteria. Resistance to this class of antibiotics, primarily through drug modification via β-lactamases, has become a major barrier to effective treatment[40].

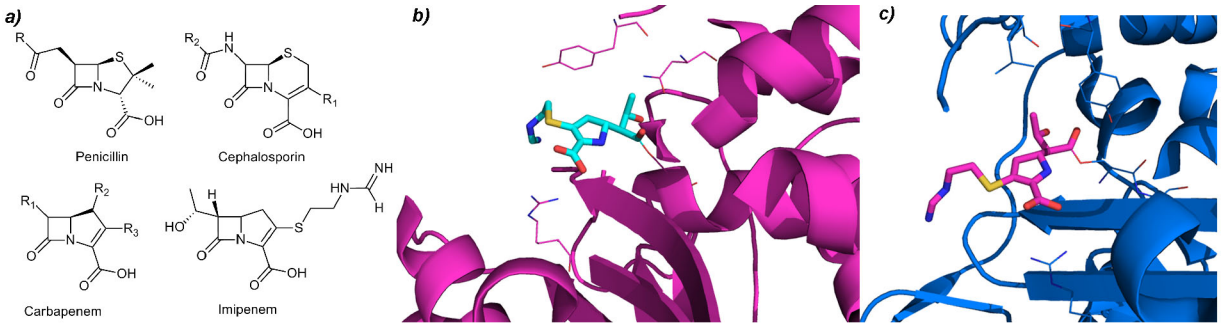

Figure 2: a. Beta-lactam antibiotic structures and imipenem, the first clinically available carbapenem antibiotic. Crystal structures of imipenem bound to b) TEM-1 (PDB: 1BT5, magenta) and c) AmpC (PDB: 1LL5, blue) beta-lactamases.

There are four different classes of β-lactamases based on structural homology. Classes A, C and D β-lactamases employ a nucleophilic serine to acylate the β-lactam bond while Class B uses a Zn^{2+} ion in the active site[55]. As β-lactamases have a high degree of structural homology to the PBPs, β-lactam antibiotics exhibit high affinity for these enzymes. Extended-spectrum β-lactamases (ESBLs), mainly from Class A, arose from early β-lactam use and are active in certain Gram-negative bacteria. ESBLs inactivate cephalosporin antibiotics that are typically resistant to acylation via β-lactamases.

Among the β-lactam antibiotics that are not susceptible to deactivation by serine β-lactamases is a class of antibiotics called carbapenems[55]. Structurally, carbapenems

have a similar 4-5 fused ring scaffold as penicillins differing by carbon substitution at the C_1 position and a double bond at the C_2-C_3 position of the pyrroline ring (Figure 2). Of the clinically relevant β-lactams, carbapenems have the greatest potency and broadest spectrum of activity towards Gram-negative and Gram-positive bacteria[56]. Carbapenems act as β-lactamase inhibitors and are thus inherently resistant to deactivation by β-lactamases. Imipenem, the first clinically available carbapenem, binds the β-lactamase active site with high affinity and like other β-lactam antibiotics becomes acylated. However, owing to a slow rate of hydrolysis, imipenem acts more as an inhibitor than a substrate. A crystal structure of imipenem bound to TEM-1, a Class A β-lactamase (PDB: 1BT5) and AmpC, a Class C β-lactamase (PDB:1LL5) captures the acyl intermediate that is key to its action as a β-lactamase inhibitor (Figure 2). The structures show the 6α-1*R*-hydroxyethyl substitutions on the β-lactam ring cause the ligand to adopt an unexpected, strained conformation once bound to the enzyme. This strained conformation displaces the hydrolytic water in the active site, protecting it from deacylation[55-57].

Discovery of newer generation carbapenems is critical in order to overcome emerging resistance by Class B β-lactamases and the metabolic instability of imipenem. Imipenem is susceptible to elimination via dehydropeptidase-1 (DHP-1) found in the renal tubules, requiring the co-administration of a DHP-1 inhibitor to improve stability. Doripenem, a later generation carbapenem, corrects for imipenem's metabolic instability, increases its Gram-negative bacterial activity and has reduced β-lactamase susceptibility[56]. In addition to overcoming metabolism by DHP-1, attempts have been made to overcome resistance to Class B, metallo-β-lactamases. This has proven to be difficult, although strides have been made using the carbapenem transition state as a basis for novel beta-lactamase inhibitors. Additionally, crystal structures of metallo-β-lactamases, such as the recently

published New Delhi metallo-β-lactamase, will aid the design of inhibitors. Other motivating factors for new carbapenem discovery include overcoming lowered PBP affinity due to point mutations, resistance due to efflux, and issues overcoming poor cellular penetration[57].

1.4b Modification of the Target: Binding Site Mutations

Mutations in the target protein that reduce the affinity between the drug and protein may arise by selection in the presence of drug pressure. The mutations may occur in the first shell of residues that contact the drug and eliminate key contacts or may arise in the outer shell and affect the conformation or dynamics of the drug-binding site. If mutations in the drug target is a mechanism by which resistance arises for a given drug, it is possible to determine the structures of both the wild type and mutated (resistant) proteins in order to understand the basis of resistance and allows for a modeling approach to predicting and overcoming the loss of interactions.

Bacterial topoisomerases, including DNA gyrase (topoisomerase II) and DNA topoisomerase IV, are the target of quinolone antibiotics and are essential for replication. The topoisomerases have formed a successful platform for drug discovery for the past several decades, beginning with the discovery of the Gram-negative antibacterial activity of nalidixic acid[37]. Over the years, there have been several generations of quinolone antibiotics, with notable examples including ciprofloxacin, levofloxacin and moxifloxacin[58]. Each generation of quinolones has expanded the spectrum of coverage of these compounds to include Gram-negative and -positive bacteria, *Pseudomonas* and *Mycobacterium tuberculosis*[58]. The primary mechanism of resistance to fluroquinolones in *S. aureus* is a stepwise accumulation of mutations in *grlA*, *grlB* and *gyrA*. High levels of

resistance are often achieved through mutations in the target combined with up regulation of efflux pump activity, for example *norA* in *S. aureus*. Crystal structures of *Acinetobacter baumanii* [59] or *Streptococcus pneumonia*[60] topoisomerase IV bound to DNA and moxifloxacin have revealed many of the details of the mechanisms of topoisomerases, the mode of inhibition of the quinolone antibiotics and the structural basis of quinolone resistance.

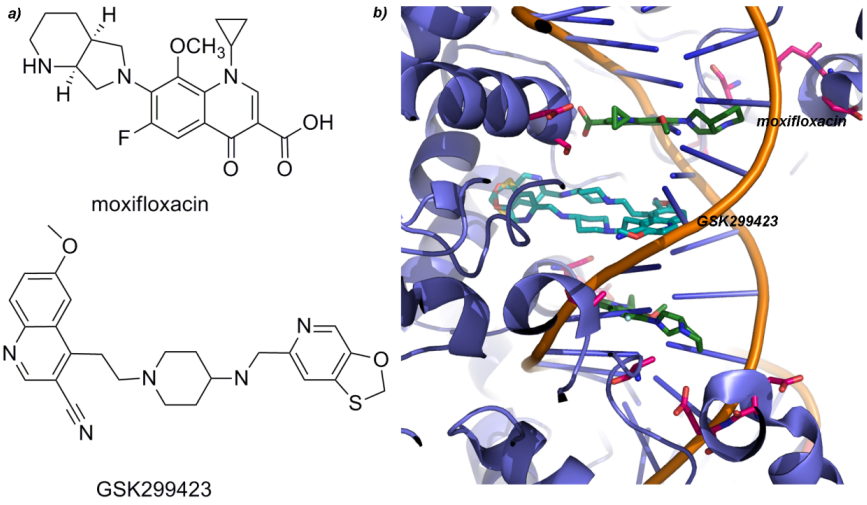

Figure 3. a) Chemical structures of moxifloxacin and GSK299423 b) The crystal structure of gyrase (purple) bound to DNA (backbone shown in orange) and two copies of GSK299423 (cyan) from PDB ID: 2XCS[61]. The figure shows a superposition of moxifloxacin (green) from PDB ID: 3FOF[60]. Typical resistance mutations are shown in magenta.

In response to the observed resistance to quinolones, several groups have worked to design more effective molecules that are active against the resistant strains. For example, scientists at Glaxo Smith Kline designed compound GSK299423 to act via a mechanism distinct from the quinolones based on stabilization of a pre-cleavage enzyme-DNA complex[61]. Structures of GSK299423 show that the compound occupies a novel non-catalytic binding pocket between the two GyrA subunits, which is adjacent to but not

overlapping with the ciprofloxacin site. As such, the affinity of the compound is not affected by the existing resistance mutations. In fact, GSK299423 shows potent activity against several bacterial strains, both wild-type and fluoroquinolone-resistant.

1.5 Conclusions

Staphylococcus aureus and its notorious ability to evolve and evade antibiotic pressure by the development of antibiotic resistance presents a major clinical burden. With the rise of community acquired MRSA strains and the continual decrease in therapies, MRSA has resulted in increased mortality, morbidity and costs associated with the onset of infections. Antifolates are crucial for the efficacious treatment of these infections, specifically the combination of TMP/SMX. However, its continued use is threatened by the development of diverse resistance mechanisms.

In this work, we present the development of a novel class of antifolates to overcome trimethoprim resistance; predicting, inducing and identifying the molecular mechanisms of resistance to the experimental and clinical antifolates. Understanding the interactions between the drug and target, through resistance, not only allows for the rational development of potent inhibitors against the resistance determinants but inhibitors that are also less susceptible to resistance. In doing this, we have identified two major lead scaffolds that show superior activity against TMP^{R} enzymes derived from the iterative process of structure based drug design.

1.6 References

1. Lowy, F. Antimicrobial Resistance: The Example of *Staphylococcus Aureus*. *J. Clin. Invest.* **2003**, *111* (9), 1265–1273.
2. Chambers, H. F.; Deleo, F. R. Waves of Resistance: Staphylococcus Aureus in the Antibiotic Era. *Nat. Rev. Microbiol.* **2010**, *7* (9), 629–641.
3. Jevons, M. P. 'Celbenin'-resistant *Staphylococci* Br. Med. J. **1961**, *1*, *124*–125.
4. Barrett, F.; McGehee, R.; and Finland, M. Methicillin-Resistant *Staphylococcus aureus* at Boston City Hospital-Bacteriological and Epidemiologic Observations. *New Engl. J. Med.* **1968**, *279*, 441–448.
5. O'Neill, J. Tackling Drug-Resistant Infections Globally: Final Report and Recommendations. *Review on Antimicrobial Resistance.* **2016**.
6. Centers for Disease Control, US Department of Health and Human Services, Antibiotic Resistance Threats in the United States, ***2013.***
7. Deese, B.; Holdren, J. Memorandum for the Heads of Executive Departments and Agencies. Science and Technology Priorities for the FY 2016 Budget. *United States Office of Science and Technology Policy.* **2014.**
8. Lodise Jr., T. P.; McKinnon, P. S. Burden of Methicillin-Resistant Staphylococcus Aureus: Focus on Clinical and Economic Outcomes. *Pharmacotherapy* **2007**, *27*, 1001–1012.
9. Styers, D.; Sheehan, D. J.; Hogan, P.; Sahm, D. F. Laboratory-Based Surveillance of Current Antimicrobial Resistance Patterns and Trends among Staphylococcus Aureus: 2005 Status in the United States. *Ann. Clin. Microbiol. Antimicrob.* **2006**, *5*, 1-9.
10. Kluytmans-Vandenbergh, M. F. Q.; Kluytmans, J. W. Community-Acquired Methicillin-Resistant *Staphylococcus Aureus*: Current Perspectives. *Clin microbiol nfect* **2006**, *12*, 9–15.
11. Lina, G.; Piémont, Y.; Godail-Gamot, F.; Bes, M.; Peter, M. O.; Gauduchon, V.; Vandenesch, F.; Etienne, J. Involvement of Panton-Valentine Leukocidin-Producing Staphylococcus Aureus in Primary Skin Infections and Pneumonia. *Clin. Infect. Dis.* **1999**, *29* (5), 1128–1132.
12. Watkins, R. R.; David, M. Z.; Salata, R. Current Concepts on the Virulence Mechanisms of Meticillin-Resistant Staphylococcus Aureus. *J. Med. Microbiol.* **2012**, *61*, 1179–1193.
13. Bush, K.; Leal, J.; Fathima, S.; Li, V.; Vickers, D.; Chui, L.; Louie, M.; Taylor, G.; Henderson, E. The Molecular Epidemiology of Incident Methicillin-Resistant *Staphylococcus Aureus* Cases among Hospitalized Patients in Alberta, Canada: A Retrospective Cohort Study. *Antimicrob. Resist. Infect. Control.* **2015**, *4*, 35.
14. Singh, R.; Ray, P.; Das, A.; Sharma, M. Penetration of Antibiotics through *Staphylococcus Aureus* and *Staphylococcus Epidermidis* Biofilms. *J. Antimicrob. Chemother.* **2010**, *65*, 1955–1958.
15. Damberger, D. M.; Boyd, S. E. Management of *Staphylococcus aureus* Infections. *Am. Fam. Physician*. **2005**, *72*, 2474-2481.

16. Zhou, W.; Scocchera, E. W.; Wright, D. L.; Anderson, A. C. Antifolates as Effective Antimicrobial Agents: New Generations of Trimethoprim Analogs. *Med. Chem . Comm.* **2013**, *4*, 908.
17. Human DHFR
18. Frey, K. M.; Lombardo, M. N.; Wright, D. L.; Anderson, A. C. Towards the Understanding of Resistance Mechanisms in Clinically Isolated Trimethoprim-Resistant, Methicillin-Resistant Staphylococcus Aureus Dihydrofolate Reductase. *J. Struct. Biol.* **2010**, *170* (1), 93–97.
19. Osborne, M. J.; Schnell, J.; Benkovic, S. J.; Dyson, H. J.; Wright, P. E. Backbone Dynamics in Dihydrofolate Reductase Complexes: Role of Loop Flexibility in the Catalytic Mechanism. *Biochemistry* **2001**, *40*, 9846–9859.
20. Frei, C. R.; Miller, M. L.; Lewis, J. S.; Lawson, K. a; Hunter, J. M.; Oramasionwu, C. U.; Talbert, R. L. Trimethoprim-Sulfamethoxazole or Clindamycin for Community-Associated MRSA (CA-MRSA) Skin Infections. *J. Am. Board Fam. Med.* **2010**, *23* (6), 714–719.
21. Gorwitz, R. J.; Jernigan, D. B.; Powers, J. H.; Jernigan, J. A. Participants in the CDC-convened experts' meeting on management of MRSA in the community: Summary of an experts meeting convened by the Centers for Disease Control and Prevention **2006**.
22. Nathwani, D.; Morgan, M.; Masterton, R. G.; Dryden, M.; Cookson, B. D.; French, G.; Lewis, D. Guidelines for UK Practice for the Diagnosis and Management of Methicillin-Resistant *Staphylococcus Aureus* (MRSA) Infections Presenting in the Community. *J. Antimicrob. Chemother.* **2008**, *61* (5), 976–994.
23. Liu, C.; Bayer, A.; Cosgrove, S. E.; Daum, R. S.; Fridkin, S. K.; Gorwitz, R. J.; Kaplan, S. L.; Karchmer, A. W.; Levine, D. P.; Murray, B. E.; et al. Clinical Practice Guidelines by the Infectious Diseases Society of America for the Treatment of Methicillin-Resistant Staphylococcus Aureus Infections in Adults and Children. *Clin. Infect. Dis.* **2011**, *52* (3), 18-55.
24. Center for Disease Control and Prevention. Centers for Disease Control and Prevention Outpatient antibiotic prescriptions — United States **2013**.
25. Hawser, S.; Lociuro, S.; Islam, K. Dihydrofolate Reductase Inhibitors as Antibacterial Agents. *Biochem. Pharmacol.* **2006**, *71*, 941–948.
26. Schneider, P.; Hawser, S.; Islam, K. Iclaprim, a Novel Diaminopyrimidine with Potent Activity on Trimethoprim Sensitive and Resistant Bacteria. *Bioorganic Med. Chem. Lett.* **2003**, *13*, 4217–4221.
27. Sincak, C.; Schmidt, J. Iclaprim, a novel diaminopyrimidine for the treatment of resistant gram-positive infections. *Ann Pharmacother.* **2009**, *43* ,1107–1114.
28. Viswanathan, K.; Frey, K. M.; Scocchera, E. W.; Martin, B. D.; Swain, P. W.; Alverson, J. B.; Priestley, N. D.; Anderson, A. C.; Wright, D. L. Toward New Therapeutics for Skin and Soft Tissue Infections: Propargyl-Linked Antifolates Are Potent Inhibitors of MRSA and Streptococcus Pyogenes. *PLoS One* **2012**, *7* (2), 1–9.

29. Walling, J. From methotrexate to pemetrexed and beyond. A review of the pharmacodynamics and clinical properties of antifolates. *Investigational New Drugs*. **2006**, *24*, 33-77.
30. Chattopadhyay, S.; Moran, R.; Goldman, I. Pemetrexed: biochemical and cellular pharmacology, mechanisms and clinical applications. *Mol. Cancer Ther.* **2007**, *6*, 404-17.
31. Bennett, B.; Wan, Q.; Ahmad, M.; Langan, P.; Dealwis, C. X-ray structure of the ternary MTX.NADPH complex of the anthrax dihydrofolate reductase: a pharmacophore for dual-site inhibitor design. *J. Struct. Biol*. **2009**, *166*, 162–171.
32. Sawaya, M.; Kraut, J. Loop and subdomain movements in the mechanism of Escherichia coli dihydrofolate reductase: crystallographic evidence. *Biochemistry* **1997**, *36*, 586–603.
33. Li, R.; Sirawaraporn, R.; Chitnumsub, P.; Sirawaraporn, W.; Wooden, J.; Athappilly, F.; Turley, S.; Hol, W. Three-dimensional structure of M. tuberculosis dihydrofolate reductase reveals opportunities for the design of novel tuberculosis drugs. *J. Mol. Biol.* **2000**, *295*, 307–323.
34. Burchall, J.; Hitchings, G. Inhibitor Binding Analysis of Dihydrofolate Reductases from Various Species. *Mol. Pharmacol*. **1965**, *1*, 126–136.
35. Kopytek, S.; Dyer, J.; Knapp, G.; Hu, J. Resistance to methotrexate due to AcrAB-dependent export from Escherichia coli. *Antimicrob. Agents Chemother*. **2000**, *44*, 3210–3212.
40. E, Aires J.; Nikaido, H. AcrB multidrug efflux pump of *Escherichia coli*: composite substrate-binding cavity of exceptional flexibility generates its extremely wide substrate specificity. *J. Bacteriol*. **2003**, *185*, 5657–5664.
42. Opperman, T.; Kwasny, S.; Kim, H. S. Characterization of a novel pyranopyridine inhibitor of the AcrAB efflux pump of *Escherichia coli. Antimicrob. Agents Chemother.* **2014**, *58* (2), 722–733.
43. Daigle, D. M.; Hughes, D. W.; Wright, G. D. Prodigious Substrate Specificity of AAC(6')-APH(2''), an Aminoglycoside Antibiotic Resistance Determinant in *Enterococci* and *Staphylococci*. *Chem. Biol.* **1999**, *6* (2), 99–110.
44. Leclercq, R. Mechanisms of Resistance to Macrolides and Lincosamides: Nature of the Resistance Elements and Their Clinical Implications. *Clin.Infect.Dis.* **2002**, *34* (1), 482–492.
45. Sutcliffe, J.; Grebe, T.; Tait-Kamradt, A.; Wondrack, L. Detection of Erythromycin Resistant Determinants by PCR. *Antimicrob Agents Chemother* **1996**, *40* (11), 2562–2566.
46. Weigel, L. M.; Clewell, D. B.; Gill, S. R.; Clark, N. C.; McDougal, L. K.; Flannagan, S. E.; Kolonay, J. F.; Shetty, J.; Killgore, G. E.; Tenover, F. C. Genetic Analysis of a High-Level Vancomycin-Resistant Isolate of Staphylococcus Aureus. *Science* **2003**, *302* (2003), 1569–1571.
47. Dale, G. E.; Broger, C.; Hartman, P. G.; Langen, H.; Page, M. G. P.; Then, R. L.; Stuber, D. Characterization of the Gene for the Chromosomal Dihydrofolate Reductase

(DHFR) of Staphylococcus Epidermidis ATCC 14990: The Origin of the Trimethoprim-Resistant S1 DHFR from Staphylococcus Aureus? *J. Bacteriol.* **1995**, *177*, 2965–2970.
48. Dale, G. E.; Broger, C.; D'Arcy, a; Hartman, P. G.; DeHoogt, R.; Jolidon, S.; Kompis, I.; Labhardt, a M.; Langen, H.; Locher, H.; et al. A Single Amino Acid Substitution in Staphylococcus Aureus Dihydrofolate Reductase Determines Trimethoprim Resistance. *J. Mol. Biol.* **1997**, *266*, 23–30.
49. Houvinen, P.; Sundstrom, L.; Swedberg, G.; Skold, O. Trimethoprim and Sulfamethoxazole Resistance. *Antimicrob. Agents Chemother*. **1995**, *39*, 279.
50. Bergmann, R.; Van Der Linden, M.; Chhatwal, G. S.; Nitsche-Schmitz, D. P. Factors That Cause Trimethoprim Resistance in Streptococcus Pyogenes. *Antimicrob. Agents Chemother.* **2014**, *58* (4), 2281–2288.
51. Nurjadi, D.; Olalekan, A. O.; Layer, F.; Shittu, A. O.; Alabi, A.; Ghebremedhin, B.; Schaumburg, F.; Hofmann-Eifler, J.; Van Genderen, P. J. J.; Caumes, E.; et al. Emergence of Trimethoprim Resistance Gene *dfrG* in *Staphylococcus Aureus* Causing Human Infection and Colonization in Sub-Saharan Africa and Its Import to Europe. *J. Antimicrob. Chemother.* **2014**, *69* (9), 2361–2368.
52. Zhao, R.; Goldman, I. D. Resistance to Antifolates. *Oncogene* **2003**, *22*, 7431–7457
53. Sigmond, J.; Backus, H.; Wouters D. *et. al.* Induction of resistance to the mutitargeted antifolate Pemetrexed (ALIMTA) in WiDr human colon cancer cells is associated with thymidylate synthase overexpression. **2003**, *66*, 431-438.
54. Silver, L. L. Challenges of Antibacterial Discovery. *Clin. Microbiol. Rev.* **2011**, *24* (1), 71–109.
55. Papp-Wallace, K.; Endimiani, A.; Taracila, M.; Bonomo, R. Carbapenems: past, present and future. *Antimicrob. Agents Chemother*. **2011,** *55*, 4943–4960.
56. Beadle B, Shoichet B. Structural basis for imipenem inhibition of class C β-lactamases. *Antimicrob. Agents Chemother.* **2002**, *46*, 3978–3980.
57. Maveyraud. L.; Mourey, L.; Korta, L.; et al. Structural basis for clinical longevity of carbapenem antibiotics in the face of challenge by the common class A β-lactamases from the antibiotic-resistant bacteria. *J. Amer. Chem. Soc.* **1988**,*120*, 9748–9752.
58. Pommier, Y.; Le, E.; Zhang, H.; Marchand, C. DNA topoisomerases and their poisoning by anticancer and antibacterial drugs. *Chem. Biol.* **2010**, *17*, 421–433.
59. Wohlkonig, A.; Chan, P.; Fosberry, A.; et al. Structural basis of quinolone inhibition of type IIA topoisomerases and target-mediated resistance. *Nat. Struc. Mol. Biol*. **2010** *17*, 1152–1153.
60. Laponogov, I.; Sohi, M.; Veselkov, D.; et al. Structural insight into the quinolone-DNA cleavage complex of type IIA topoisomerases. *Nat. Struc. Mol. Biol.* **2009**, *16*, 667–669.
61. Bax, B.; Chan, P.; Eggleston, D.; et al. Type IIA topoisomerase inhibition by a new class of antibacterial agents. *Nature* **2010,** 466, 935–940.

Chapter 2

Development of Propargyl-linked Antifolates as Potent Antimicrobial Agents

2.1 Evolution of Propargyl-linked Antifolates from Trimethoprim

Antifolates are important agents for continued anti-cancer and anti-microbial treatments. Trimethoprim is a well-tolerated, inexpensive antibiotic with a broad activity against gram-positive, gram-negative and parasitic diseases. However, the development of resistance and prevalence of innately resistant pathogens limits the use of this therapeutic. Efforts to develop a new class of antifolates against these clinically important and resistant disease states attempt to combat these problems. The development of this class of antifolates employed the iterative process of structure based drug design, in which high resolution X-ray structures of the protein:inhibitor complex are used to guide inhibitor design. Rational modifications to the inhibitor scaffold, based on the interpretation of the crystal structures, are tested *in-vitro* to validate or reject the design principle[1]. Ultimately, this method should result in the development of selective, potent inhibitors optimized against its target.

Crystal structures of trimethoprim in complex with *Cryptosporidium hominis* (*C. hominis*) dihydrofolate reductase (Ch DHFR) revealed that the inhibitor's poor fit into the active site is responsible for its innate resistance. Evaluation of the Ch DHFR active site revealed a narrow hydrophobic 'tunnel' leading to an unoccupied substrate-binding pocket. Therefore, a series of TMP-like antifolates were developed to expand the distance between the diaminopyrimide and trimethoxybenzyl rings and extend the inhibitor further into the active site to accumulate hydrophobic interactions[2].

Modifications to the TMP structure and extension of the single methyl linkage include an acetylene linker (Figure 1, Scaffold A) and ethylene linker including the cis- and trans-isomers as well as its saturated alkane counterparts (Scaffold B). However, the only TMP derivative that gained activity against these parasitic DHFR enzymes contained a rigid acetylene linker connected to the trimethoxybenzyl ring by a propargylic carbon (PLA Scaffold)[3]. This scaffold, named for its propargyl linker, was further modified with alkyl substitutions on the diaminopyrimidine ring and propargylic position resulting in a series compounds with nanomolar activity against the enzyme.

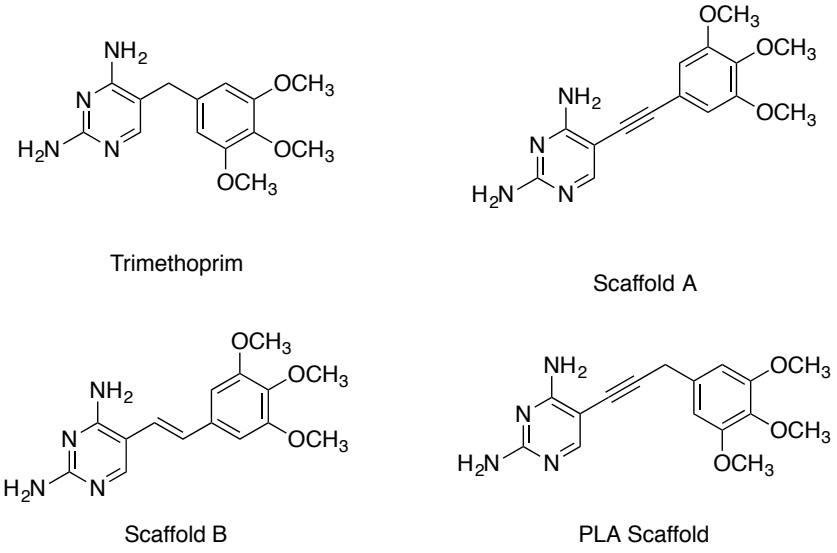

Figure 1 TMP Derivatives Optimizing Linker Identities

Cryptosporidium hominis (C. hominis) is an opportunistic parasite that was a major cause of morbidity in immunocompromised patients, specifically those with HIV. However, as HIV diagnostics and therapies improved, the clinical impact of *C. hominis* decreased[4] and the focus of the development of Ch DHFR inhibitors shifted to gram-negative and gram-positive bacteria as well as pathogenic fungal and mycobacterium species.

The first generation PLAs were assessed against *Bacillus anthracis*, an innately TMP^R gram-positive bacteria that was feared as a tool of bioterrorism[5]. Crystal structures of the PLAs in the *Bacillus anthracis* dihydrofolate reductase (Ba DHFR) active site shows the acetylene fitting through the narrow hydrophobic tunnel made of Phe 96 and placing the trimethoxybenzyl ring in the hydrophobic, substrate binding pocket, as designed. Additional analysis of the structures indicated that further alkyl substitutions at the C_6 position on the diaminopyrimidine ring, specifically an ethyl substituent; exploits interactions with an active site valine (Val 32) and leucine (Leu 29) residue. This work concluded that increased potency and selectivity over human DHFR can be achieved by adding bulky substitutions at the meta-position of the trimethoxybenzyl ring to increase contacts within the substrate binding site[6]. This revelation lead to the development of the second generation of propargyl-linked antifolates that feature an ethyl substituted diaminopyrimidine linked to the meta-substituted biaryl system by an acetylene linker (Figure B). The proximal B-ring and distal C-rings can be substituted with both heterocycles or aromatic rings as well as small alkyl or polar substituents, allowing for further optimization and establishment of a structure activity relationship.

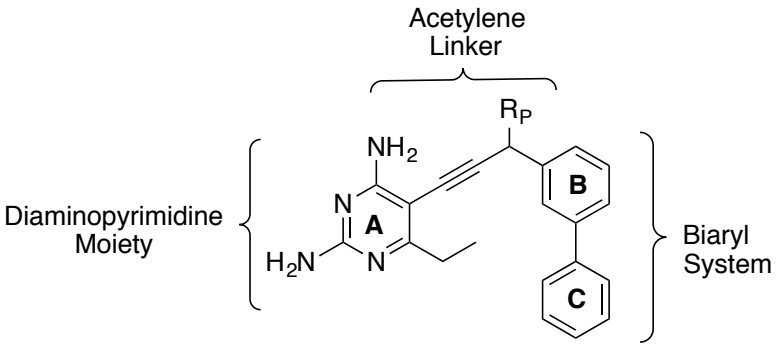

Figure 2 Second Generation PLA Scaffold

The second generation of propargyl-linked antifolates explored different C-ring substituents. Inhibitors with a distal benzyl or dimethyl benzyl were evaluated against wild-type *S. aureus* DHFR (DfrB) and a quality control *S. aureus* strain (ATCC 43300). The series of compounds with these hydrophobic C-rings exhibited very potent (3-80 nM) enzymatic potency and MICs below 100 ng/mL[7]. Crystal structures of this series validate the design principles of building these compounds into the substrate-binding pocket. The structure showed the standard polar interactions between the active site and diaminopyrimidine ring as well as hydrophobic interactions with Val 31 and stacking interactions between the acetylene linker and Phe 92 side chain. The biaryl system picked up extensive side chain Leu 20, Leu 28, Ile 50 and Leu 54 contributing to the formation of stable, inhibitory complex with the distal ring pointed toward the solvent exposed pocket of the enzyme. Unfortunately, this class of compounds displayed poor solubility and potent activity against human DHFR and resulted in minimal selectivity with over 70% of the inhibitors having a human/ *S. aureus* selectivity ratio of <10 [7].

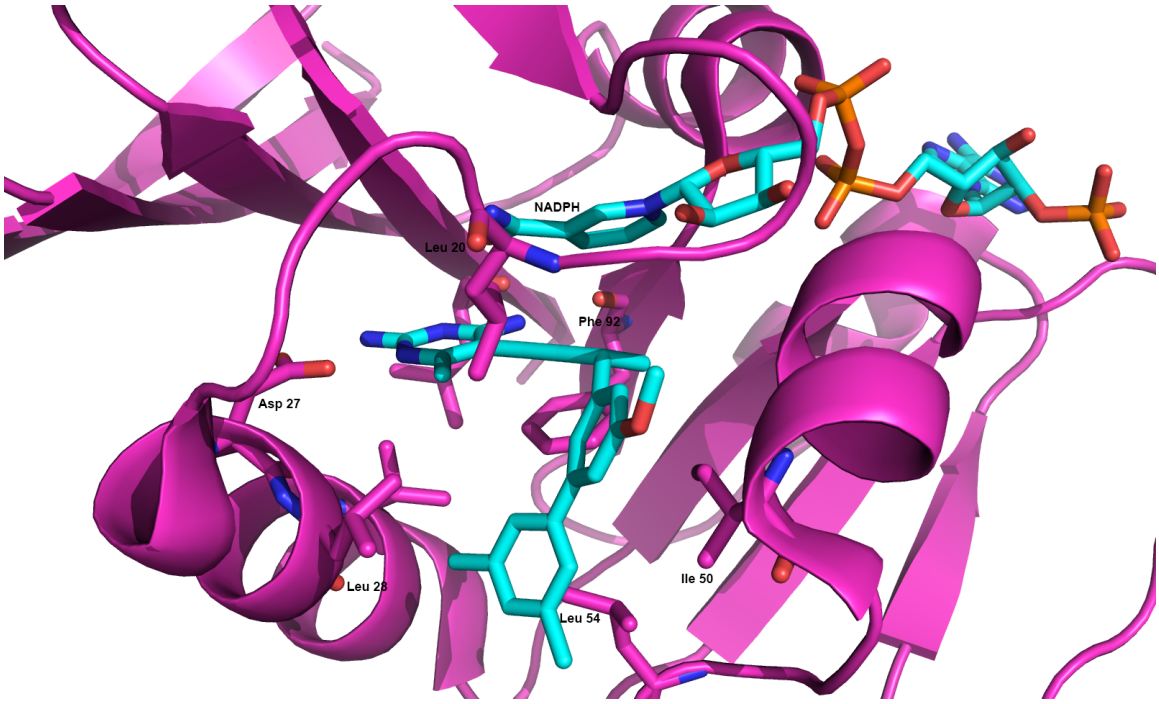

Figure 3 Crystal structure of a distal dimethylbenzyl substituted biaryl PLA bound to *S. aureus* DHFR (3F0S) highlighting the extensive network of hydrophobic interactions between the inhibitor and active site.

Replacement of the benzyl and substituted benzyl rings with heterocycles, namely 4-pyridine, increased the selectivity, potency and solubility of the class (Section 2.2). The biaryl compounds showed increased potency against a panel of gram-positive bacteria, including *Staphylococcus aureus* and *Streptococcus pyogenes*[7] as well as gram-negative bacteria[8] and fungal species *Candida albicans* and *Candida glabrada*[9,10]. This class of compounds was also used as probes to explore the importance of stereochemistry at the propargylic position (Section 2.3). A third, and current, generation of PLAs were further optimized by the addition of a *para*-carboxylate meant to form ionic interactions with polar amino acids in the distal region of the substrate-binding site, this class of compounds is described in Section 2.4.

2.2 Pyridine PLAs as a Promising Lead Scaffold

The *meta*-pyridine biaryl PLA scaffold was the first promising lead series within the class against *S. aureus* DHFR. The evolution of the propargyl linked antifolates from single aryl trimethoprim derivatives to hydrophobic, bulky meta-biphenyl compounds illustrates how this class of compounds can be optimized as potent DHFR inhibitors. The further incorporations of C-ring heteroatoms to the biaryl scaffold increased potency, solubility and selectivity. Identifying 4-pyridyl PLAs as a second-generation lead scaffold provides an opportunity for continued development and optimization by exploring various R_P and B-ring substitutions (Figure 4)[7]. The second-generation pyridine class of PLAs can be divided into three major scaffolds: mono-methoxy substituted, di-methoxy substituted and a rigid dioxolane, fused ring scaffold.

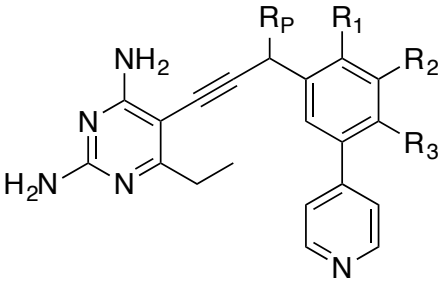

Figure 4 Pyridine PLA Scaffold

2.2a Methoxy-substituted PLAs

Compounds with single substitutions at the R_1 and R_2 positions were synthesized with and without alkyl substitutions at the propargyl position (R_P), evaluated for both cellular and enzymatic activity, establishing a structure activity relationship. The R_1 substituted compounds show a 32-fold difference in cellular activity when comparing the propargyl hydrogen (UCP1021) and the propargyl methyl (UCP1040) with MICs of 0.0195 μg/mL and 0.625 μg/mL but show very similar enzymatic activity with IC_{50} values of 21nM and 30nM, respectively (Figure 5). The addition of the propargylic methyl creates a single stereocenter in the inhibitor, which could account for the loss off activity seen with UCP1040, as single enantiomer inhibitors are known to display differential activity against

its enzymatic target[11]. The importance of the stereochemistry at this position was explored and discussed in Chapter 2.3.

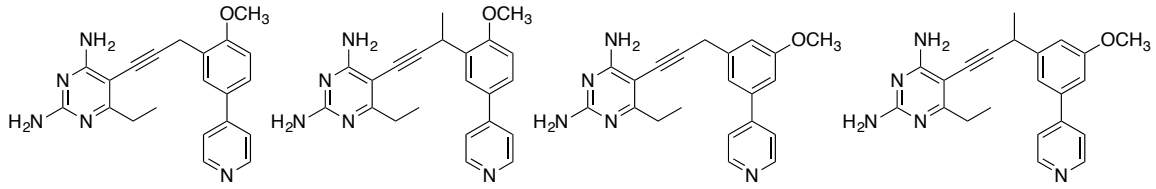

UCP1021
MIC: 0.0195 μg/mL
IC_{50}: 21 ±1 nM

UCP1040
MIC: 0.625 μg/mL
IC_{50}: 30 ±1 nM

UCP1015
MIC: 0.0781 μg/mL
IC_{50}: 12 ±2 nM

UCP1006
MIC: 0.0781 μg/mL
IC_{50}: 19 ±1 nM

Figure 5 Methoxy-substituted PLAs with Cellular and Enzymatic Activities

Moving the methoxy from the R_1 to the R_2 position only resulted in minimal losses in cellular activity, with MICs increasing from 0.0195 to 0.0781μg/mL with a R_P hydrogen substitution (UCP1015). However incorporation of a methyl at this position, in combination with the R_2-methoxy (UCP1006), results in no MIC shift when compared to UCP1015, however it gains 8–fold activity over its R_1-methoxy equivalent. Similarly, the IC_{50} values for these compounds are almost indistinguishable at 19nM and 12nM for UCP1006 and UCP1015 (Figure 5)[7].

Previously published crystal structures indicate an extensive network of hydrophobic interactions between the pyridine PLA and the DHFR active site, in addition to the hydrogen bonding interactions of the diaminopyrimidine moiety to an active site water, side chain of Asp 27 and backbone carbonyls of Leu 5 and Phe 92. The aromatic Phe 92 side chain makes additional stacking interactions with the acetylene linker and the side chains Leu 28 and Val 31 make additional hydrophobic interactions with the C_6-ethyl on the diaminopyrimidine. Ile 50 and Leu 54 side chains make extensive interactions with the

biaryl system whose pyridine ring is oriented towards the solvent exposed area of the active site. Finally, the propargyl methyl appears to make hydrophobic interactions with the nicotinamide ring of NADPH (Figure 6).

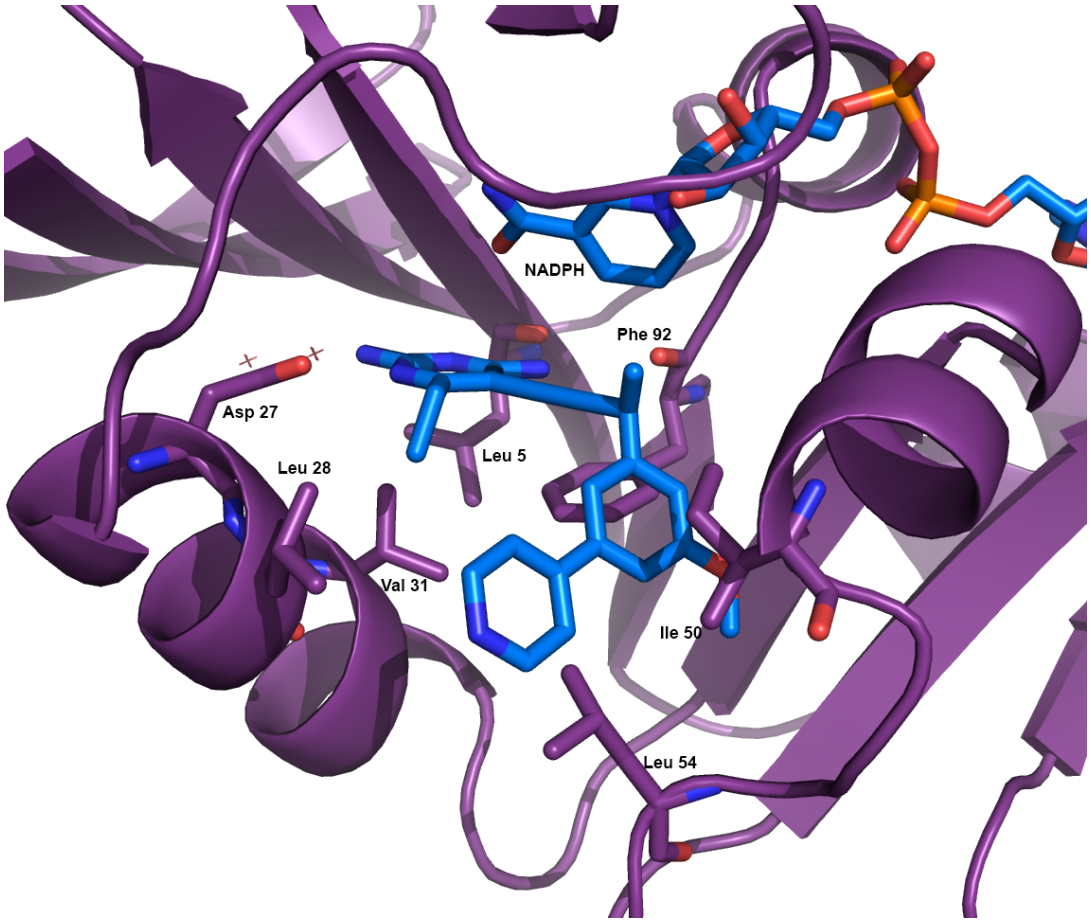

Figure 6 DfrB (purple) complexed with NADPH and UCP1006 (blue) highlighting the hydrogen bonding and hydrophobic interactions between the inhibitor and active site, PDB ID: 3SGY.

2.2b Dimethoxy and Dioxolane Substituted PLAs

Single methoxy B-ring substitutions on the pyridine scaffold afford potent activity against wild-type MRSA (ATCC 43300) and DHFR enzyme (DfrB). Trimethoprim contains three methoxy B-ring substituents proximal to the hydrophobic active site, accumulating weak

interactions that result in potent, broad-spectrum activity. Increasing and exploiting these hydrophobic interactions can further optimize the pyridine PLAs and increase potency against the DHFR targets. To probe this hypothesis, a series of pyridine PLAs with dimethoxy substituents (R_1/R_3 and R_2/R_3 substituted) pyridine PLAs were synthesized and evaluated. The series of compounds also features compounds with a benzodioxolane fused ring system at the R_1/R_2 and R_2/R_3 positions revealing a SAR between dioxolane positions as well as propargyl substitutions.

Pyridine PLAs with methoxy substituents at the R_1/R_3 and R_2/R_3 were synthesized and evaluated, the latter scaffold with and without substitutions at the R_P position. With R_P hydrogens, moving the second methoxy from the R_1 (UCP1033) to R_2 (UCP1039) positions resulted in a 16-fold increase in both cellular and enzymatic activity with MICs of 0.3125 μg/mL to 0.0195 μg/mL and IC_{50} values of 202 nM and 14 nM, respectively (Figure 7). The addition of the propargylic methyl to UPC1039 (UCP1082) resulted in an increase in MIC to 0.3125 ug/mL, mimicking the MIC of the R_1/R_3 substituted and potentially indicating that substitutions at the R_P and R_1 positions have similar effects in substrate binding (Figure 7).

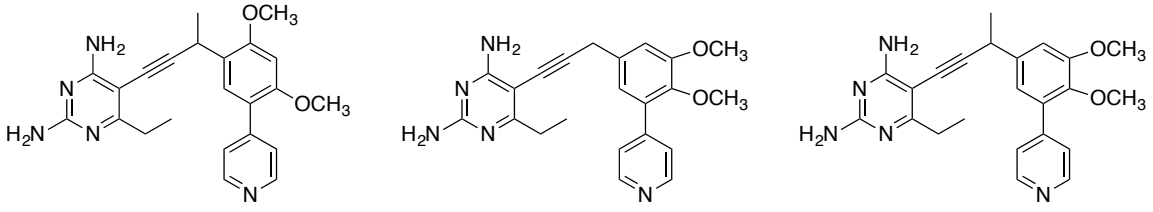

UCP1033
MIC: 0.3125 μg/mL
IC_{50}: 202 ±18 nM

UCP1039
MIC: 0.0195 μg/mL
IC_{50}: 14 ±1 nM

UCP1082
MIC: 0.3125 μg/mL
IC_{50}: 30 ±1 nM

Figure 7 Dimethoxy-substituted PLAs with Cellular and Enzymatic Activities

This series was pursued further by constraining the dimethoxy substitutions via a dioxolane ring resulting in a fused B-ring system that has reduced flexibility in the active site. Even though substitutions at the R_1 positions were not optimal for the dimethoxy series, a single R_1/R_2 benzodioxone compound with an R_P methyl was evaluated. This compound exhibited poor cellular and enzymatic activity with an MIC of 0.625 μg/mL and an IC_{50} of 4.2 μM. Shifting the dioxolane ring to the R_2/R_3 positions (UCP1038) reduced the MIC to 0.0781 μg/mL and IC_{50} value to 17nM. Furthermore, removal of the R_P-methyl raised the MIC to 0.3125 μg/mL but left the IC_{50} unaffected while the introduction of two R_P-methyl substituents further increased the MIC to 0.625 μg/mL (UCP1072, Figure 8).

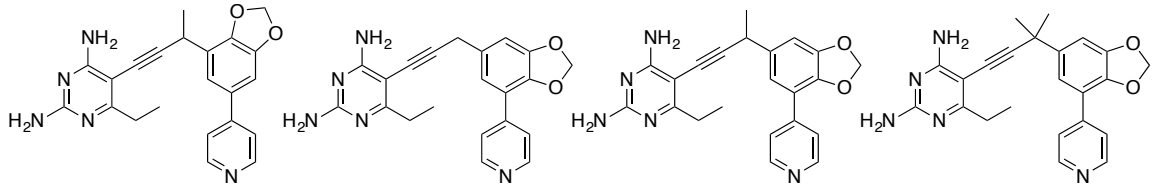

UCP1037
MIC: 0.625 μg/mL
IC_{50}: 4.2 ±1 μM

UCP1042
MIC: 0.3125 μg/mL
IC_{50}: 19 ±1 nM

UCP1038
MIC: 0.0781 μg/mL
IC_{50}: 17 ±1 nM

UCP1070
deuterated
MIC: 0.0781 μg/mL
IC_{50}: 35 ±3 nM

UCP1072
MIC: 0.625 μg/mL
IC_{50}: ND

Figure 8 Dioxolane-substituted PLAs with Cellular and Enzymatic Activities

Because dioxolane rings are a known metabolic liability, as the acetal can form covalent bonds to the heme of CYP enzymes a R_P methyl, R_2/R_3 dioxolane with deuterium at this position was synthesized (UCP1070)[12]. When trying to avoid metabolic or other pharmacokinetic liabilities, deuterium, which mimics hydrogen in size and chemical properties, can substitute hydrogen atoms and mitigate these reactivities[13]. The addition of the deuterium to the dioxolane ring resulted in no loss of activity when compared to its hydrogenated counterpart (UCP1038).

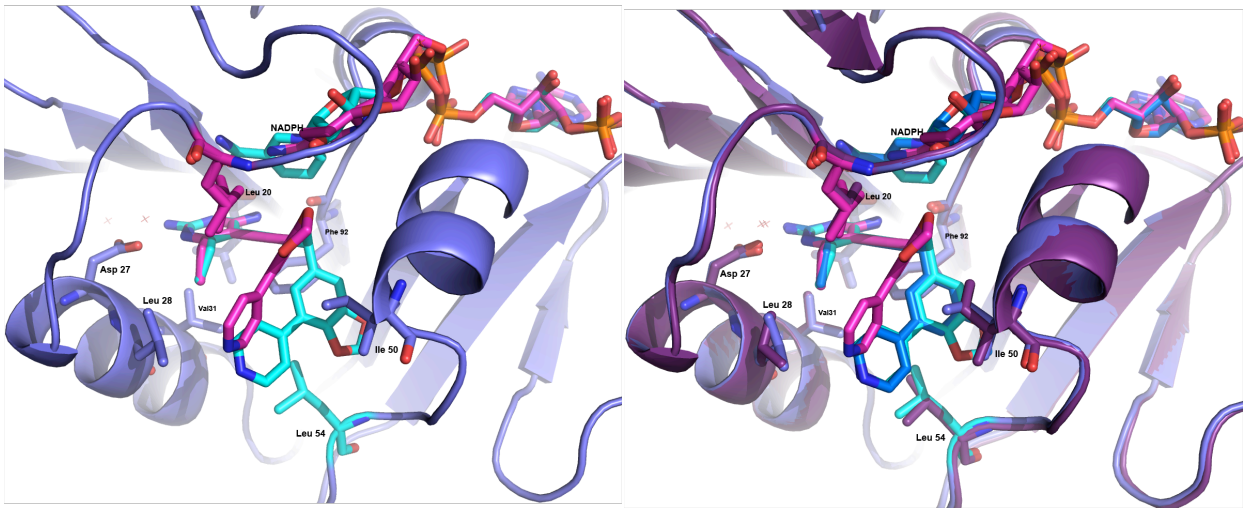

Figure 9 The crystal structure of a) DfrB:NADPH:UCP1070 (blue) and b) DfrB:NADPH:UCP1070 (blue) superimposed with DfrB:NADPH:UCP1006[7] (purple). The amino acids that form interactions with specific binding modes are the same color as the corresponding inhibitor.

A 1.47Å crystal structure of UCP1070 complexed with DfrB reveals two distinct conformations of NADPH and binding positions of the biaryl system. The two binding modes could be a result of the capture of the single enantiomers within the racemic mix, where as one inhibitors binds in the same orientation observed in Figure 6 and the other occupies a more solvent exposed binding pocket of the active site (Figure 10b). The structure reveals distinct hydrophobic interactions between the two binding modes where Ile 50 maintains contact with both but one inhibitor position forms interactions with Leu 54 (blue) and the other picks up interactions with Leu 20, located on a flexible loop region of the active site (pink, Figure 9). The additional interactions made between dioxolane ring and Leu 20 and Ile 50 side chains may contribute to the superior potency of the dioxolane and dimethoxy-substituted compounds, validating this attempt to further optimize the class of PLAs. The relevance and implications of the variable and novel NADPH configurations seen in Figure 9 are discussed in depth in Chapter 2.5.

2.3 Enantiopure Propargyl-linked Antifolates

Some of the most potent PLAs that have been evaluated against DHFRs of pathogenic bacteria feature a methyl substitution at the propargyl position resulting in a single stereogenic center[6-10]. Previous structural studies with a series of PLAs show that these branched substituents are proximal to the cofactor-binding site and may provide compensatory interactions with NADPH as well as providing conformational control of the biaryl ring system[14,15]. Therefore, investigating the role of the stereogencicity of the propargyl center in governing the inhibitors activity becomes priority. Probing the role of the configuration at the single stereocenter in these inhibitors required the preparation of a series of non-racemic, branched PLA inhibitors. These inhibitors possess potent enzyme inhibition (IC_{50} values <50nM), antibacterial effects (most MICS <1μg/mL) and form stable ternary complexes with the cofactor and enzyme. Individual crystal structures of a pair of enantiomers in *S. aurues* DHFR reveal that a single change in configuration of the stereo-center drove both the binding orientation of the biaryl systems as well as the selection of an alternative NADPH cofactor[16].

2.3a Biochemical and Microbiological Evaluation of Enantiomers

The series of enantiopure inhibitors indicates that the compounds maintain strong inhibition of wild-type *S. aureus* DHFR (DfrB) with the majority of inhibitors having IC_{50} values less than 50nM (Table 1). The compounds also display significant antibacterial activity against a quality control strain of MRSA (ATCC 43300) with the most active enantiomers showing an 8-fold increase in activity over trimethoprim. In contrast to TMP, the PLAs were designed to form alternative and additional contacts with residues in the active site by the biaryl domain and branched at the propargylic position to become less dependent on synergy with the cofactor. Interestingly, varying degrees of antibacterial

activity were observed within the pairs of enantiomers. For example, the MICs of the *R*- and *S*- R_1 methoxy substituted inhibitors (UCP1061 and UCP1062) differed 8-fold with values of 0.3125 μg/mL and 0.0391 μg/mL, respectively. Similarly, the *R*- and *S*-R_2 methoxy inhibitors (UCP1064 and UCP1063) have MIC values of 1.25 μg/mL and 0.078 μg/mL, a 16-fold difference in antibacterial activity. Conversely, the R_3 methoxy (UCP1096/UCP1097), dioxolane (UCP1098/UCP1099) and R_2 ,R_3-dimethoxy (UCP1079/ UCP1080) substituted compounds only had a 2- or 4-fold discrepancy in MIC values (Figure 10, Table 1).

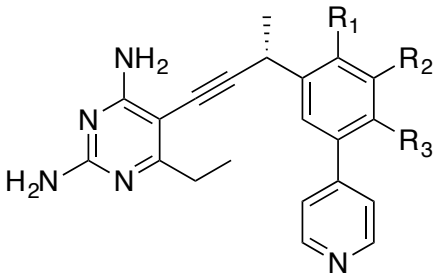

UCP1061: R_1=H, R_2=OCH_3, R_3=H
UCP1063: R_1=OCH_3, R_2=H, R_3=H
UCP1079: R_1=H, R_2=OCH_3, R_3=OCH_3
UCP1096: R_1=H, R_2=H, R_3=OCH_3
UCP1098: R_1=H, R_2, R_3=Dioxolane

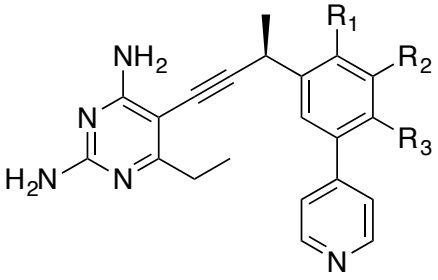

UCP1062: R_1=H, R_2=OCH_3, R_3=H
UCP1064: R_1=OCH_3, R_2=H, R_3=H
UCP1080: R_1=H, R_2=OCH_3, R_3=OCH_3
UCP1097: R_1=H, R_2=H, R_3=OCH_3
UCP1099: R_1=H, R_2, R_3=Dioxolane

Figure 10 Structures of Enantiopure PLA compounds

Table 1 Biological activity of Enantiopure PLA compounds

Inhibitor	Sa MIC (μg/mL)	DfrB IC_{50} [a] (nM)	DfrB IC_{50} [b] (nM)	NADPH Rate (μM/min)	Thy^+ Sa MIC (μg/mL)
UCP1061 *(R)*	0.3125	15.0 ± 0.7	69 ± 5	-0.919	5
UCP1062 *(S)*	0.0391	18± 2	155 ± 5	-0.965	5
UCP1063 *(S)*	0.0781	11 ± 0.7	37 ± 5	-0.454	5
UCP1064 *(R)*	1.25	19 ± 1	464 ± 27	-4.571	10
UCP1079 *(R)*	1.25	46 ± 4	26 ± 3	-0.850	10
UCP1080 *(S)*	2.5	74 ± 6	98 ± 8	-2.712	>20
UCP1096 *(R)*	1.25	202 ± 20	458 ± 37	-19.944	10
UCP1097 (*S)*	0.3125	35 ± 6	211 ± 12	-0.428	10
UCP1098 *(R)*	0.3125	46 ± 6	78 ± 4	-1.241	5
UCP1099 *(S)*	0.0781	35 ± 2	45 ± 6	-0.359	10
TMP	0.3125	23 ± 3	77±4	-0.505	>20

[a] Measured with 5 minutes pre-incubation of enzyme and inhibitor
[b]Measured with no pre-incubation of enzyme and inhibitor

As antibacterial activity is highly dependent on the degree and persistence of the blockade of the essential targeted pathway, we investigated the target inhibition profile of the enantiomers with DHFR. By comparing enzyme inhibition values using the standard incubation of enzyme and inhibitor (5 min)[7] with those that did not have the pre-incubation step, we attempted to detect differences in the capacity for the enantiomers to quickly for a stabled, inhibited complex. The results show an increase in the observed IC_{50} values with the magnitude of increase depending on the specific pairs. For example, the dioxolane derivatives (UCP1098/ UCP1099) display on marginal increases in IC_{50} value while the R_2-methoxy derivative (UCP1063) shows a more substantial increase in observed IC_{50} (24.4-fold) as well as a more significant difference between the two

enantiomers (3.4 vs. 24.4-fold). Overall these experiments suggest that some inhibitors require the pre-incubation step in order to form a high affinity complex.

Rates of dissociation of the complexes were also determined for five pairs of enantiomers. Dissociation, in which the inhibitors and the enzyme were incubated with the enzyme for 18-24 hours prior to activation with the substrate, was determined to further understand the stability of the tertiary complex[17]. The enzymatic reaction, measured by the rate of oxidation of NADPH, was monitored over an hour period and the differential rate of dissolution of the complex was determined for each enantiomer pair. Overall, the target inhibition profile experiments show that inhibitors, UCP1063, UCP1079, UCP1080, UCP1098 and UCP1099 appear to form an inhibited complex quickly. Furthermore, several inhibitors including UCP1061, UCP1062, UCP1063, UCP1079, UCP1097 and UCP1099 have a relatively show rate of dissociation of this complex (Table 1 and Figure 11). As effective antibacterial agents must quickly form a long-lasting and effective inhibitory complex with the target, these results are promising, especially for UCP1063 and UCP1099, as these compounds possess both of these characteristics.

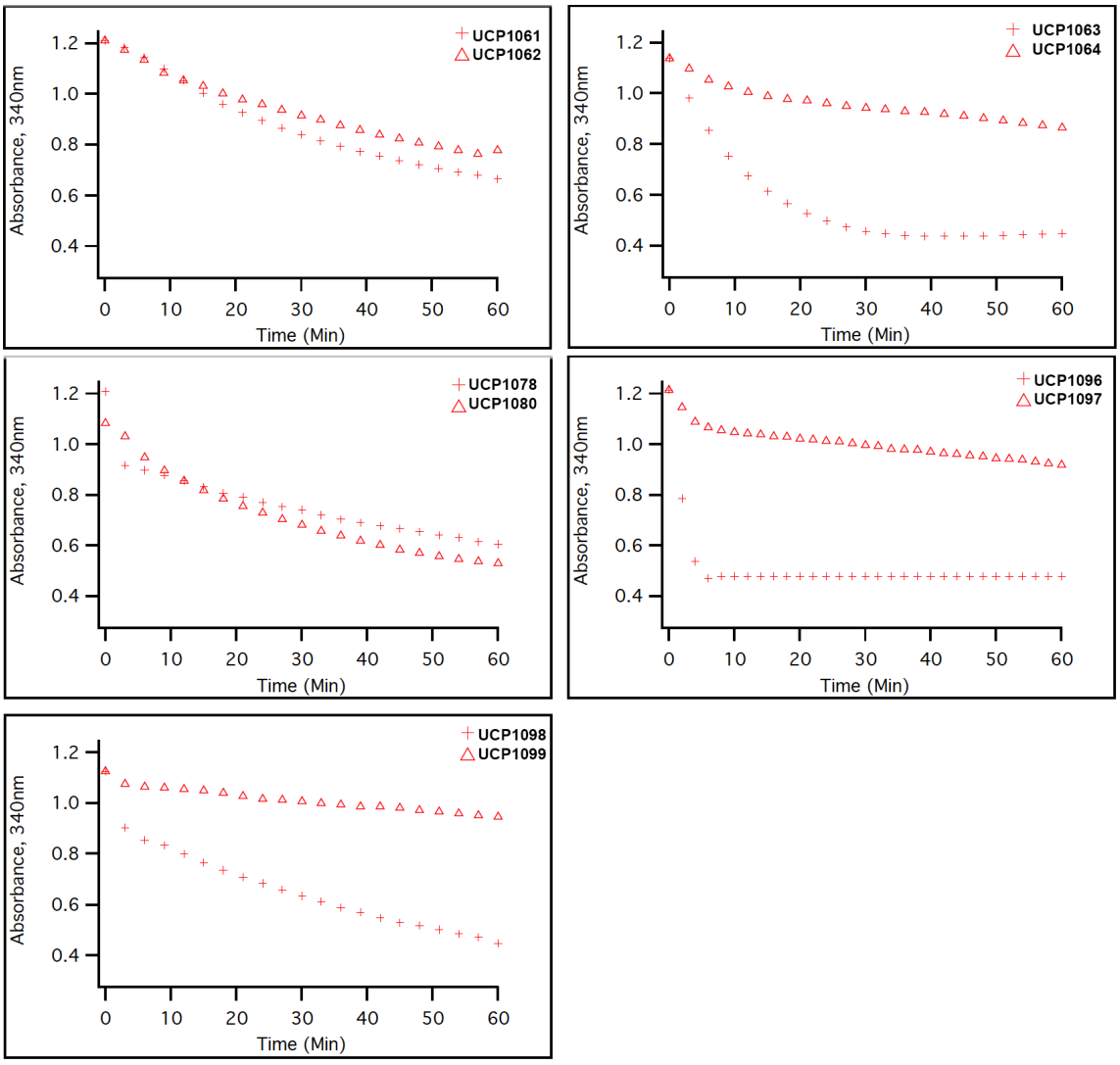

Figure 11 Dissociation of the inhibitory complex (DfrB:NADPH:PLA) over a 60 minutes reaction period following 18 hours of incubation. Differences of dissociation rates indicate the differences in stability of the complex attributing to antimicrobial effects.

The potential of the enantiomers to possess differential affinity to an unknown second target, resulting to increased antibacterial activity, was probed by end-product rescue experiments. As the PLAs are inhibitors of the folic acid biosynthetic pathway, which is primarily responsible for the production of deoxythymidine monophosphate, rescue experiments were conducted to measure MIC values in the presence of excess thymidine (Thy^+)[18]. With 10 µg/mL thymidine, MIC values rose to 5-10 µg/mL indicating on-target

activity (Table 1). Thy^+ MICs that increase less than 8-fold indicates inhibitory activity against a target outside of the folic acid cycle. It is not believed that differences in enantiomer activity are due to preferential permeability or efflux, as the physiochemical properties of the enantiomers are identical[16].

2.3b Structural Studies of an Enantio-pure Pair of Inhibitors

Crystal structures of DfrB complexed with UCP1061 and UCP1062 reveal unexpected and significant differences in the binding mode of the two enantiomers with the enzyme. After collection of diffraction data (2.69Å and 2.16Å, respectively) the structures were determined by molecular replacement with probe molecule PDB ID 3F0Q[10]. The structure of DfrB:NADPH:UCP1062 is identical to the previously reported structure of *S. aureus* DHFR crystallized with its racemic counter part, UCP1006 (Figure 6)[7], suggesting that the ternary complex with UCP1062 is more thermodynamically stable complex relative to that formed with UCP1061. In the structure of DfrB:NADPH:UCP1062, the enzyme binds the extended, β-form of NADPH with a number of key van der Waals contacts between the inhibitor and the nicotinamide ring of the cofactor involving each of the four carbons of the propargyl linker. In addition to the expected interactions between the diaminopyrimidine and residues Asp 27, Val 31 and Leu 28 there are contacted between Leu 28, Ile 50, met 42 and Leu 54 and the hydrophobic pyridine C-ring favors a coplanar arrangement with its joined B-ring (Figure12).

The structure of DfrB:NADPH:UCP1061 reveals a major change in both biphenyl binding mode and NADPH cofactor binding where the nicotinamide and ribose rings are displaced approximately 3.2Å relative to the standard β-NADPH anomer, a result of the puckering of the internal phosphates. In this alternative NADPH structure, as seen in the

DfrB:NADPH:UCP1070 structure (Figure 9), the caboxamide forms three water-mediated hydrogen bonds to the protein rather than the direct hydrogen bonding interactions with Ala 7 (Figure 12b). Despite this displacement, the pyrophosphate tail and adenine nucleotide are ultimately placed in the identical binding positions[14,15]. The significance and impact this alternative NADPH is discussed in-depth in Section 2.5.

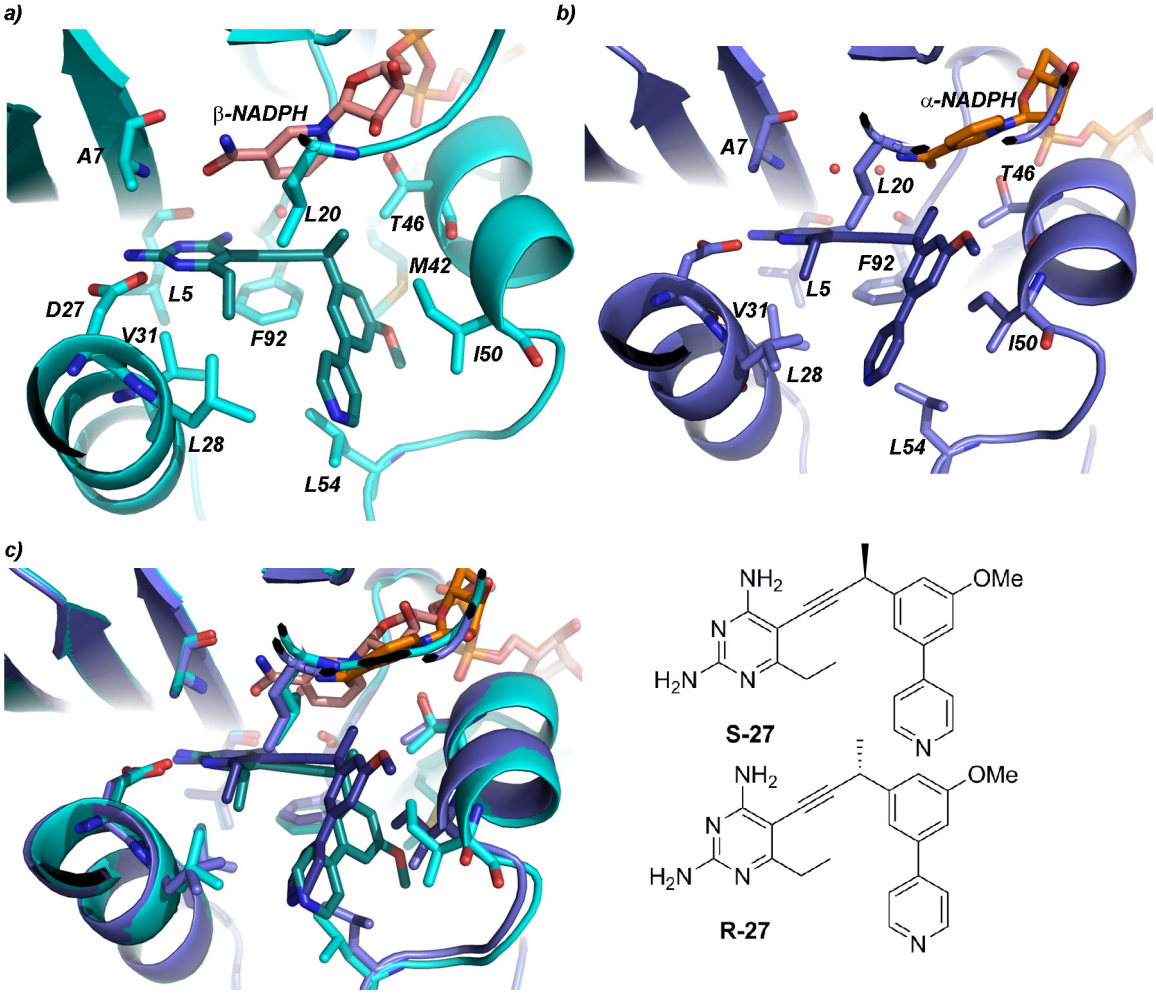

Figure 12 Crystal structures of wild-type *S. aureus* DHFR (DfrB) bound to cofactor and inhibitors: a) compound UCP1062 (teal) and β-NADPH (salmon) or b) compounds 1061 (purple) and α-NADPH NADPH (orange). Panel C shows a superposition of the two structures.

Aside from NADPH, Ile 50 undergoes a second significant conformation change in order to accommodate the differing enatiomeric preference. Both a 1.5Å displacement of the protein backbone and a change of the side chain rotamer of Ile 50 are necessary to accommodate the R-configuration of UCP1061. Therefore, when a racemic mixture of the ligand is present, the protein would need to undergo a significant conformation change to binding the opposite enantiomer.

Evaluation of 5 pairs of enantiopure PLAs in the effort to further optimize the scaffold towards efficacious inhibition of *S. aureus* emphasizes the importance of substitutions, specifically the stereochemistry of substitutions at this propargylic position. Biochemical, microbiological and structural analysis indicates differences in binding orientations, cofactor recruitment, and the stability of the inhibitory complex; each contributing to differing antibacterial activities between enantiomer pairs. This work highlights the importance of pursuing enantiomerically pure inhibitors as we continue to modify and optimize the series.

2.4 Charged Propargyl-linked Antifolates

Classical antifolates, such as methotrexate and pemetrexed, mimic substrate structure and exhibit sub-nanomolar affinity for eukaryotic and prokaryotic DHFR enzymes. However, these compounds lack bacterial efficacy due to insufficient permeability into the cell, a result of its highly charged nature[20-22]. These classical antifolates, marketed as potent chemotherapeutic, are actively transported into eukaryotic cells through folic acid transporters, but because bacterial cells produce folic acid de novo, they do not possess the mechanisms required for uptake. Methotrexate's high affinity for the enzyme is credited to the ionic interactions formed between the enzyme and the glutamate tail of the

compounds[23] (Figure 13). Similarly, the superior activity of the pyridine PLAs over TMP is attributed the increase of interactions between the inhibitor and enzyme. However, building onto the PLA scaffold by the addition of a C-ring carboxylate to mimic that of methotrexate and folic acid to pick up ionic interactions with an active site argenine residue and further optimize the inhibitors.

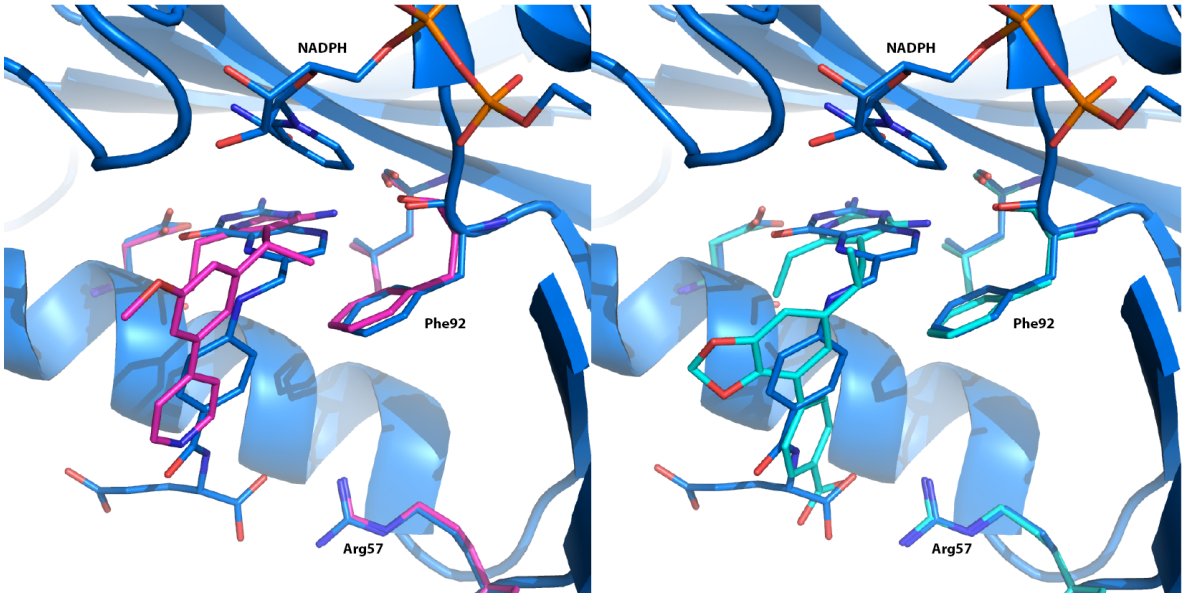

Figure 13 SaDHFR complexed with β-NADPH and a) folate (blue, PDB:3FRD) and UCP1061 (magenta) a pyridine substituted and b) UCP1191(light blue) a carboxylate substituted PLA. The ionic interaction acquired through the addition of the C-ring carboxylate is highlighted in panel B.

In addition to the acquisition of a hydrogen bonding interaction between the inhibitor and the protein, the introduction of charged character to the PLAs is expected to increase permeability of the compounds into gram-negative bacteria, namely *Escherichia coli* and *Klebsiella pneumonia.* The absence of PLA activity against these pathogenic strains is attributed to the lack of passive diffusion through the thick peptidoglycan outer membrane of these pathogenic species[8]. Fluoroquinolones, specifically ciprofloxacin, and tetracyclines have potent activity against these gram-negative bacteria, their ability to

penetrate the membranes and accumulate in the cell is attributed to the zwitterion character of a single carboxylic acid[23.] In order to explore these hypotheses, we developed a series of compounds that features a phenyl C-ring with carboxylic acid substitution and varying B-ring and propargylic substitutions (Figure 14). While the addition of zwitterionic character did not increase activity in gram-negative species, with the most potent compounds having a MIC of 10 μg/mL[24], ventures to improve the protein-inhibitor interactions were successful.

2.4a Biological Evaluation of COOH-PLAs against S. aureus

UCP1106, a *para*- carboxylate substituted PLA with an R_1-methoxy, was the first compound of the series to be evaluated revealing very promising cellular and enzymatic activity in wild-type *S. aureus*. The role of the carboxylate placement was explored and optimized within the series, by synthesizing and evaluating the *ortho*- (UCP1133) and *meta*- (UCP1124) substituted analogs (Figure 14, Table 2). Migration of the carboxylate from the *para*- position to both the *meta*- and *ortho*- positions resulted in significant, 5- and 12- fold decrease in cellular activity, with a rise in MIC from 0.0195 μg/mL to 0.625 μg/mL and >20 μg/mL, respectively.

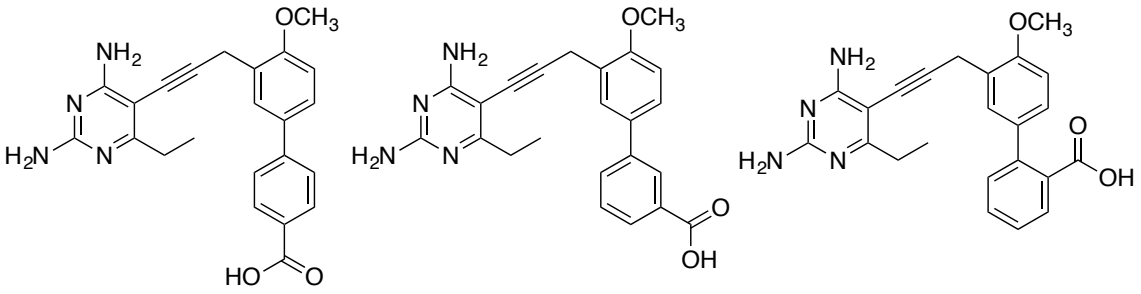

UCP1106 UCP1124 UCP1133

Figure 14 Structures of PLAs to determine COOH placement SAR

The series of *p*-carboxylate compounds was further expanded with various B-ring and propargylic substitutions. Moving the methoxy from the R_1 (UCP1106) to the R_2 (UCP1175) position resulted in a three-fold increase in enzymatic activity against SaDHFR, from 32 to 11 nM, respectively. This modification also resulted in a 2-fold decrease in MIC from 0.0195 to 0.0098 μg/mL. Meanwhile, the placement of the methoxy group had little effect on activity against HuDHFR (Table 2)[24, 25].

Evaluation of enatiopure PLAs is crucial for the continued optimization of the series of COOH-PLAs, as the methyl configuration is important not only for its noncovalent interactions but also for directing the binding position of the biaryl system[16]. The S-enantiomer of UCP1106 (UCP1164) exhibits no significant change in IC_{50}, unlike the R-enantiomer (UCP1163) that has a 7-fold loss in enzymatic activity and 16-fold loss in cellular activity with MICs of 0.625 μg/mL. The R_2- methoxy enantiomers, inhibitors UCP1172 (*R*) and UCP1173 (*S*), maintain similar activity as their hydrogen-substituted counterpart (UCP1175), with MICs of 0.0098 μg/mL and IC_{50} values of 8.9 nM, 14 nM and 11 nM, respectively. Similarly, UCP1205 and UCP1206 and the racemate UCP1191 with a constrained dioxolane ring at the R_2 and R_3 positions are nearly distinguishable by activites with MICs of 0.0098 μg/mL and IC_{50} values of 18nM,17nM and 10nM, respectively (Figure 15, Table 2).

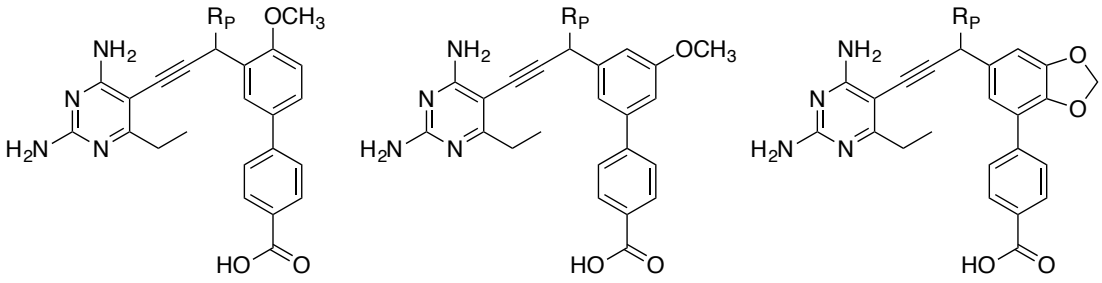

UCP1163: R_P= **S**-CH_3
UCP1164: R_P= **R**-CH_3

UCP1172: R_P= **R**-CH_3
UCP1173: R_P= **S**-CH_3

UCP1191: R_P= CH_3
UCP1205: R_P=**R**-CH_3
UCP1206: R_P=**S**-CH_3

Figure 15 Structures of the Evaluated PLA Compounds

Table 2 Cellular and Ezymatic Evaluation of COOH-PLAs

Inhibitor	S. aureus MIC (μg/mL)	SaDHFR IC_{50} (nM)	Hu DHFR IC_{50} (μM)
UCP1106	0.0195	32 $\pm$ 0.001	870 $\pm$ 30
UCP1124	>20	359 $\pm$ 0.03	10,800 $\pm$ 200
UCP1133	0.625	157 $\pm$ 0.008	1,580 $\pm$ 60
UCP1163	0.625	37 $\pm$ 2	1,630 $\pm$ 90
UCP1164	0.0391	216 $\pm$ 20	1,960 $\pm$ 0.05
UCP1172	0.0098	9 $\pm$ 0.7	1,020 $\pm$ 0.06
UCP1173	0.0098	14 $\pm$ 1	1,700 $\pm$ 100
UCP1175	0.0098	11.0 $\pm$ 0.6	690 $\pm$ 40
UCP1191	0.0098	10.0 $\pm$ 0.2	ND
UCP1205	0.0098	18 $\pm$ 3	ND
UCP1206	0.0098	17 $\pm$ 2	ND
TMP	0.3125	23 $\pm$ 3	198.2 $\pm$ 0.1
MTX	>40	ND	ND

p-COOH PLAs exhibits potent cellular and enzymatic activity against *S. aureus* MICs values ranging from 0.0098-0.625 μg/mL (Table 2). Furthermore, inhibitors UCP1175, UCP1172 and UCP1173 were shown to be bactericidal with minimum bactericidal

concentrations (MBC) less than four times the MIC[24,26]. While this class of compounds does not overcome barriers in gram-negative activity, as they were designed to, the compounds are promising candidates for development against gram-positive species.

2.4b Structural Analysis of Charged PLAs in S. aureus DHFR

In order to understand the mechanisms of action and validate design principles, the X-ray crystal structures of *S. aureus* DHFR bound to a panel of COOH-PLAs were determined. Crystals of SaDHFR complexed with NADPH and inhibitors UCP1106, UCP1175 and UCP1191 produced diffraction amplitudes to 2.24 Å, 1.81 Å and 1.88Å, respectively. All structures were solved using molecular replacement using: PDB 3F0Q[19] as a model. All structures feature the COOH-PLA bound with full or partial occupancy of β-NADPH and its alternative α-anomer in its cyclized, ring-closed tautomer. In all structures, the diaminopyrimidine of the antifolate forms conserved hydrogen bonds with Asp 27 and backbone carbonyl oxygen atoms from Leu 5 and Phe 92 (Figure 16). The propargyl linker and benzodioxalane B-ring form hydrophobic interactions with Phe 92, Thr 46, Leu 28, Val 31 and Ile 50. The phenyl C-ring is positioned well to form hydrophobic interactions with Leu 54, Val 31 and Leu 28.

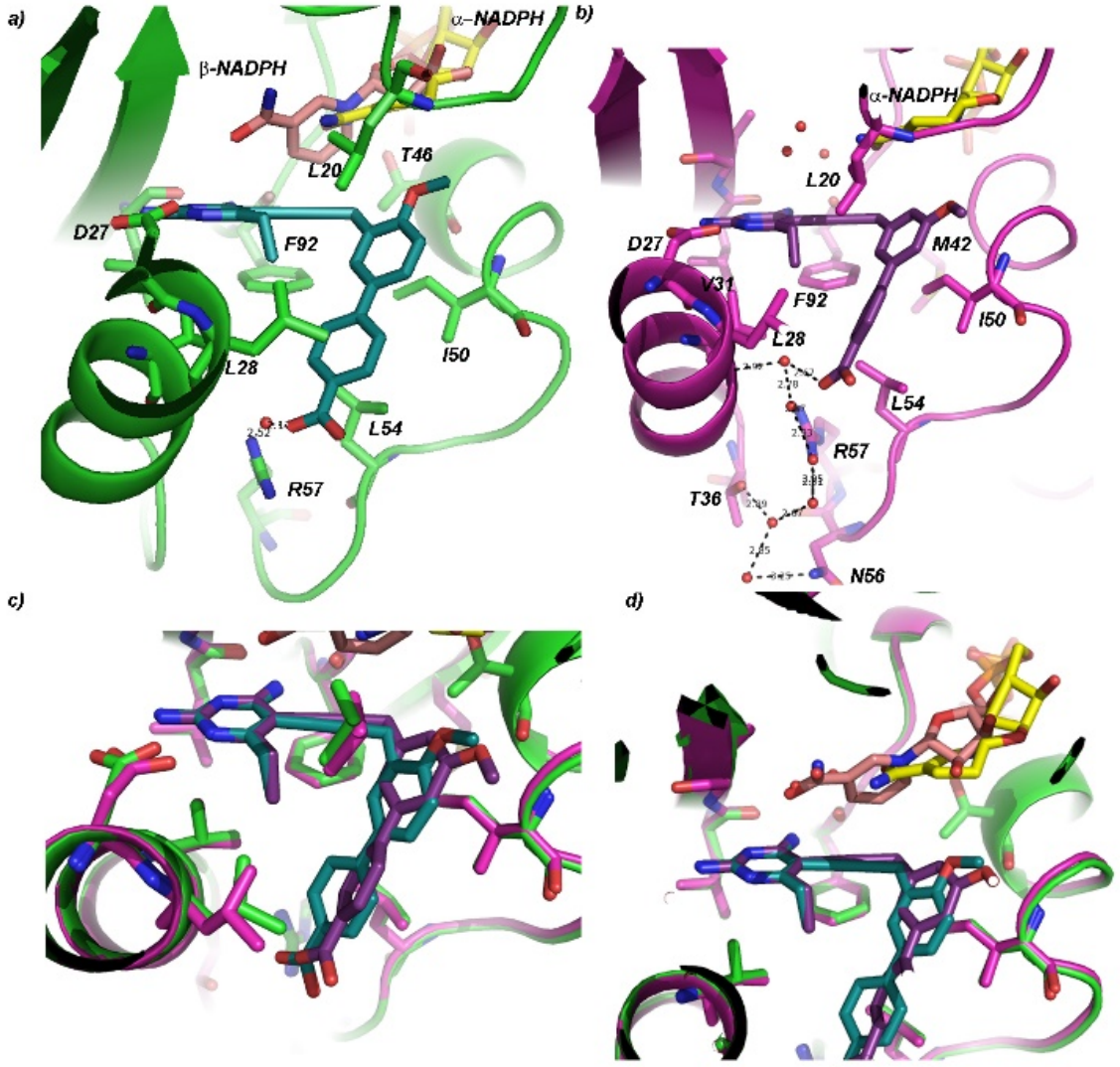

Figure 16 Active site views of a) UCP1106 and b) UCP1175 highlighting water network formed between the inhibitor and enzyme and comparisons of c) the binding position of the hydrogen substituted PLAs and d) the contrasting NADPH conformations

The UCP1106 complex shows the coordination of a water molecule between the carboxylic acid (2.1Å) and the side chain of Arg 57 (2.8Å) (Figure 16a). Conversely, the structure with compound UCP1175 exhibits an extensive water network involving at least four water molecules, coordinated between the carboxylic acid and both amino groups on Arg 57 as well as the carbonyl oxygen of Leu 28. The water network expands to include additional hydrogen bonding interactions with the side chains of Asn 56 and Thr 36

(Figure 16b). The binding modes of the inhibitor represent significant differences in the crystal structures with inhibitors UCP1106, UCP1175 and UCP1191. The methoxy substitution in the R_1 position of compound UCP1106 shifts the biaryl system 1.2 Å toward the solvent exposed surface, which is likely responsible for differences in the observed water networks between compounds UCP1106 and UCP1175 (Figure 16c).

Crystal structures of UCP1191, reveals a potential basis for the increased cellular and enzymatic potency of propargylic substituted PLA-COOH compounds. Importantly, the carboxylate moiety forms one direct ionic bond to Arg 57 and one water-mediated hydrogen bond to Arg 57 and Lys 32 (Figure 17), as opposed to the water network formed with between the carboxylate and Arg 57 in both UCP1106 and UCP1175 structures. This direct interaction is believed to occur in all of the propargyl substituted PLA-COOHs, explaining the increased activities of UCP1172, UCP1173, UCP1205 and UCP1206. Conversely, the R_1-methoxy substitution of UCP1163 and UCP1164 is believed to dictate its binding location, where substitutions of the propargylic position are not likely push the biphenyl system closer to Arg 57.

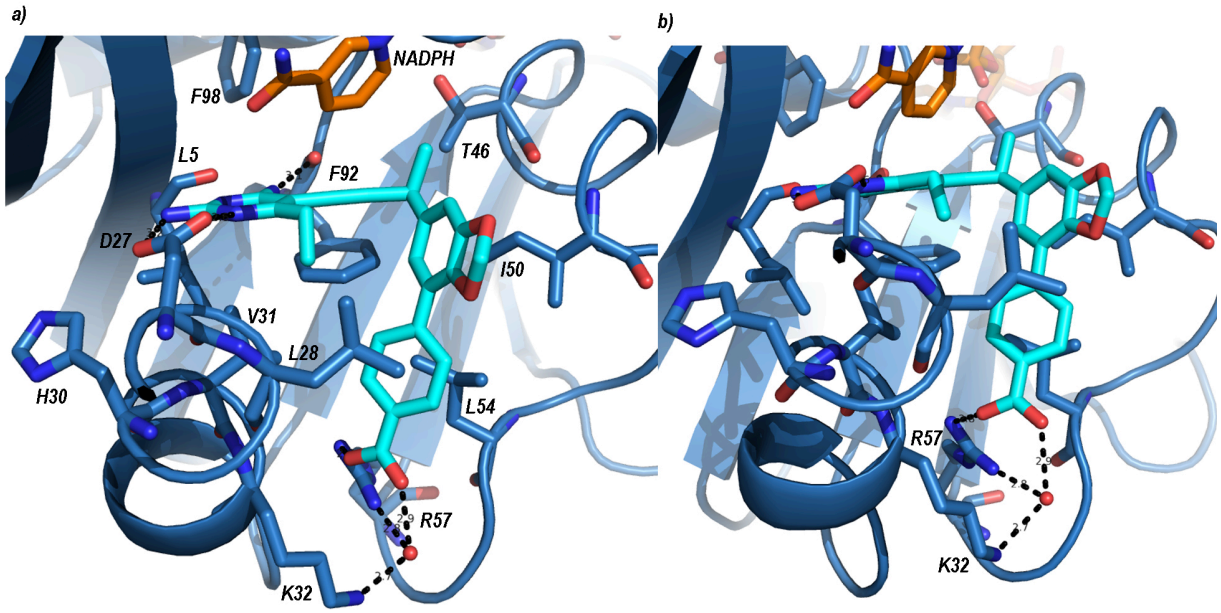

Figure 17 Binding of UCP1191 in the active site highlighting the a) water mediated interaction with Arg 57 and b) direct hydrogen bonding interactions.

Both UCP1106 and UCP1175 structures feature the cyclized α-anomer of NADPH in the cofactor-binding site. The structure with DfrB:NADPH:UCP1106 shows 40% occupancy and that with DfrB:NADPH:UCP1175 shows 100% occupancy of the tricyclic α-NADPH anomer. DfrB:NADPH:UCP1191 contains 100% occupation of the extended β-NADPH cofactor. This switch in NADPH identity, discussed in Section 2.5, is believed to be a result of the binding position of the acetylene linker, dictated the various propargylic and B-/ C-ring substitutions.

Allowing the incorporation of negatively charged functionality to the PLA scaffold and the addition of key contacts with the enzyme afforded some of the most potent and selective activity seen within the class of antifolates. Structural studies reveal how the incorporation of a carboxylate moiety can mimic one of the key interactions common to classical antifolates. Specifically, it was demonstrated that modifications to B-ring and propargylic

substitutions allow for the optimization of inhibitor binding. Optimization within this series of compounds resulted in the displacement of a water network and the formation a strong, direct ionic interaction with the side chain of Arg 57. As Arg 57 is conserved in pathogenic DHFR enzymes, specifically TMP^S and TMP^R *S. aureus* associated enzymes; it is likely that the interactions between these PLAs with this residue will also be conserved; this point is an important distinction that will be highlighted in Chapters 4 and 5.

2.5 Role of NADPH in PLA Binding and Activity

Crystallographic studies of propargyl-linked antifolates with *S. aureus* DHFR revealed an unexpected, novel NADPH configuration. This phenomenon was first observed in a series of wild-type and mutant crystal structures with a panel of first generation PLAs[14,15]. Initially, this alternative NADPH was believed to be β-NADPH bound in a novel conformation, however further analysis has revealed that the change is actually a consequence of a switch in configuration at the anomeric carbon of the nicotinamide ribose to produce the α-form. NADPH is known to exist in equilibrium between the two anomers, with a distribution of approximately 1.5 % α- and 98.5% β-form[27]. The β- to α-anomerization requires a reversible ring opening, ring-closing mechanism (Figure 18).

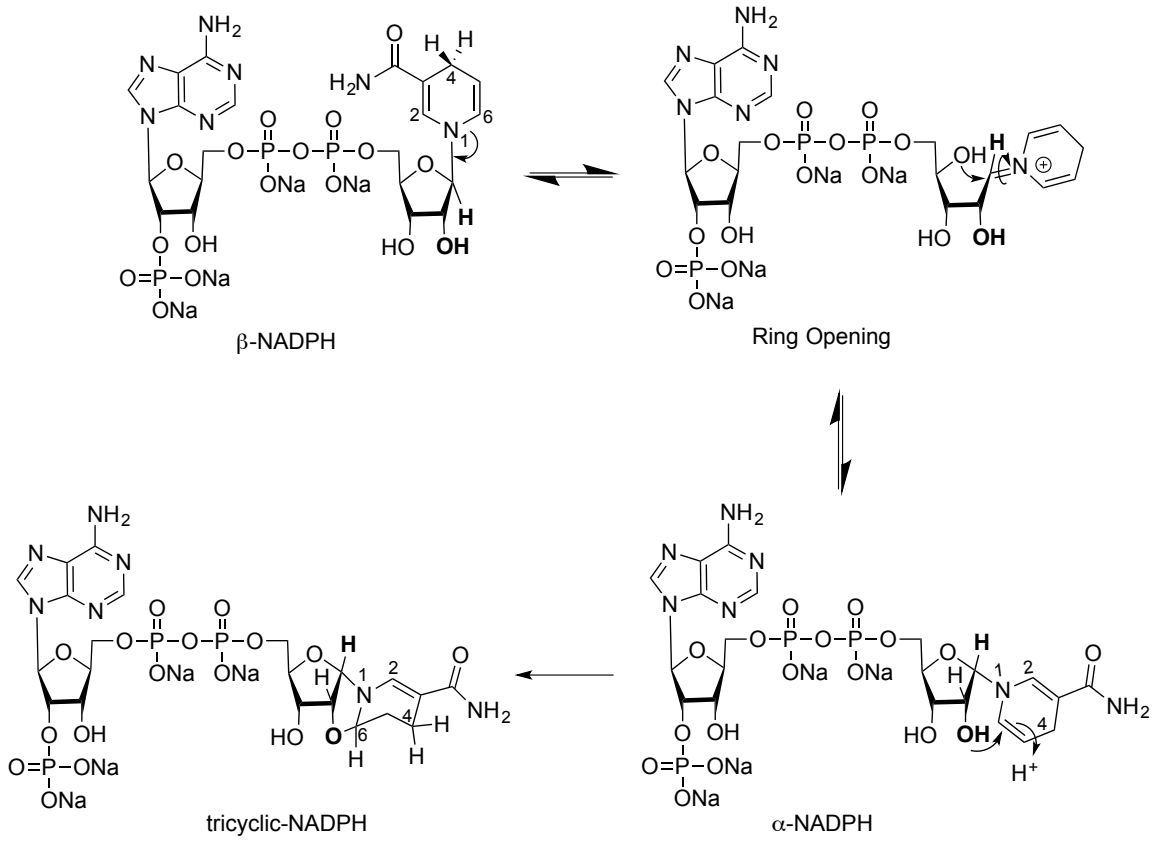

Figure 18 The mechanism of the reversible, acid catalyzed β- to α-NADPH anomerization followed by the irreversible tautamerization.

Upon additional scrutiny of the crystal structures and their electron density maps, it was discovered that the α-NAPDH anomer actually exists in its cyclized, closed tautomer state (Figure 18, 19). This additional step results in the formation of a covalent bond (Figure 18) that requires the precursory β- to α- anomerization to occur in order for the nicotinamide and ribose alcohol to be on the same plane for reaction[28,29]. However, biochemical evaluations show that tNADPH is neither an active cofactor nor an inhibitor of DHFR, as enzymatic assays with the purified tricyclic NADPH have an IC_{50} of 111 $\pm$6 uM. While the source of the tricyclic NADPH is unknown, it is believed that the protein facilitates and stabilizes the condensed α-NADPH configuration, which is believed to be a transition state for the transformation of tricyclic-NADPH[29].

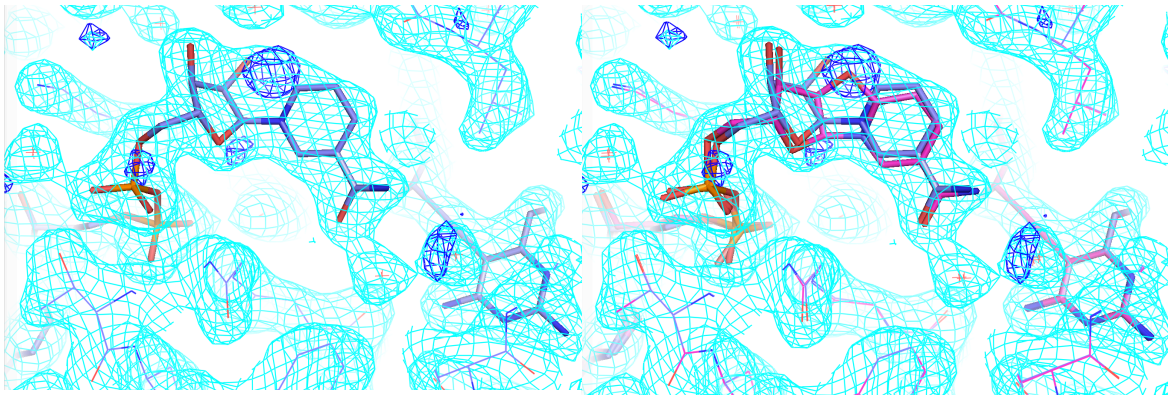

Figure 19 Difference density (dark blue) in the structure of DfrB:NADPH:UCP1061 indicates that alpha NADPH anomer (purple) exists in the closed ring tautomer state (magenta). Moving the ribose alcohol to fit the difference density resulted in the ring closure, capturing the rigid NADPH tautomer.

In the structures featuring the tNADPH, the nicotinamide ring is displaced 2.5Å for amine and 4.5Å for the carboxyl atom compared to its β-NADPH counterpart. The displaced nicotinamide ring coordinates three water molecules between the amide and the backbone of Phe 92, Ile 14 and Ala 7, whereas the nicotinamide amide of β-NADPH forms direct hydrogen bonding interactions with Ala 7 (Figure 20). Additionally, the alternative anomer displaces a water molecule coordinated between the nicotinamide phosphate of β-NADPH and the sidechain of Asn 18, which becomes occupied by the ribose moiety of α-NADPH stabilizing the condensed NADPH conformation. Cyclization results in the slight displacement of a water coordinated between the ribose and side chains of Asn 18 and Asp 120, however the displaced ribose gains a direct interaction with Asn 18 (Figure 21).

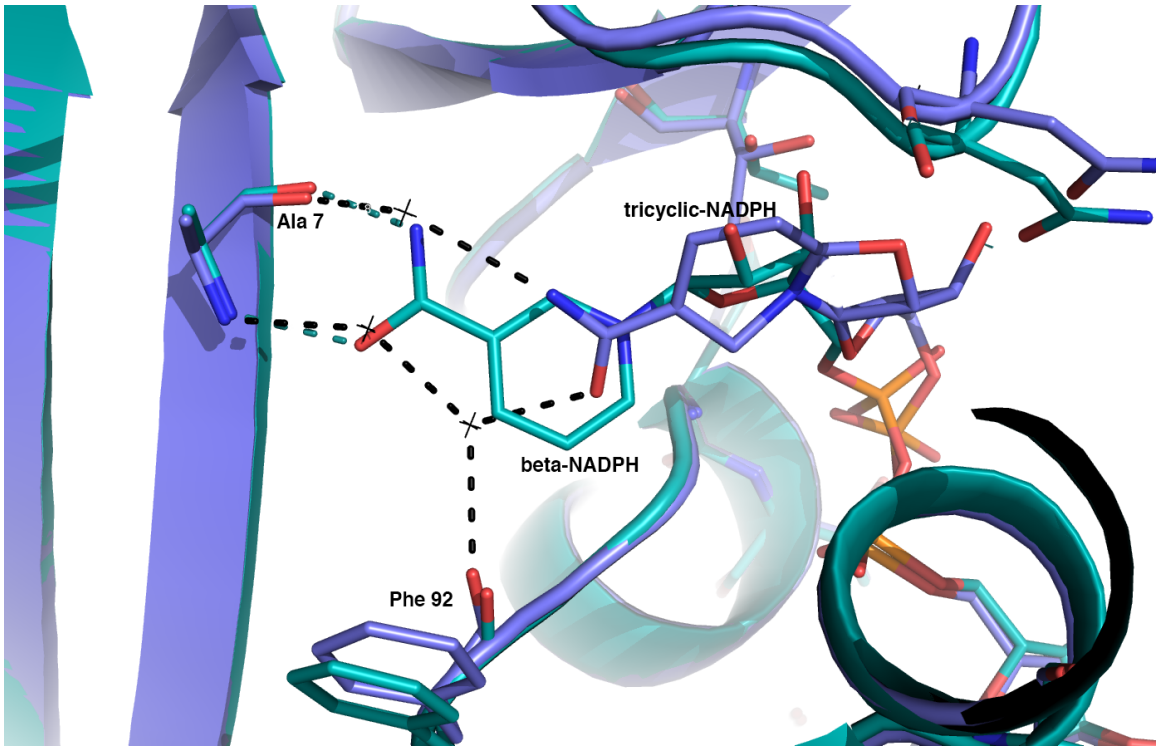

Figure 20 The interactions of the nicotinamide rings of both beta- and tricyclic-NADPH with DfrB active site. The beta-NADPH (blue) forms two direct hydrogen bonding interactions with Ala 7 and the tricyclic-NADPH (purple) coordinates three water molecules between Ala 7, Phe 92 and Ile 14 (not shown).

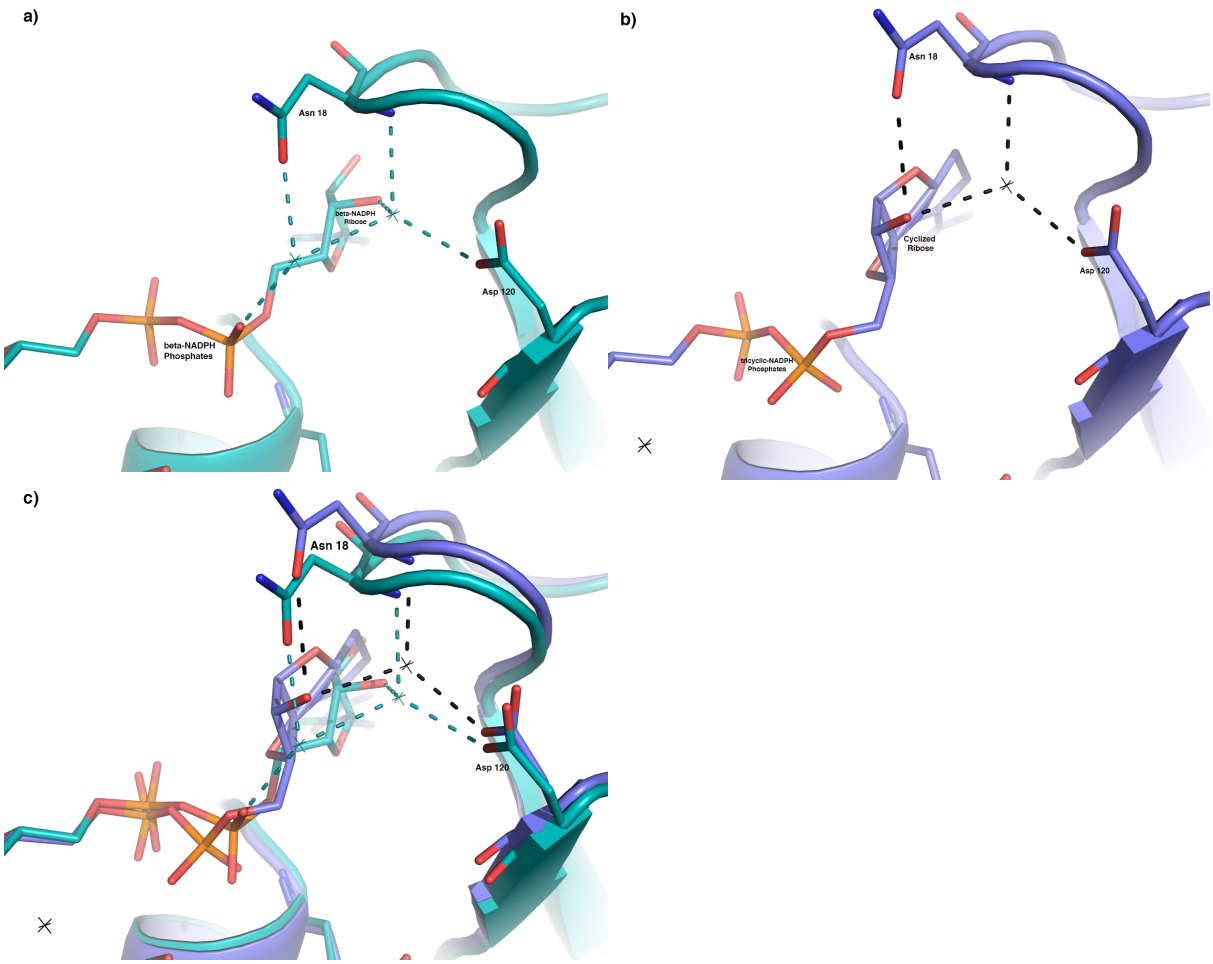

Figure 21 The interactions between a) beta-NADPH (green) and b) tricyclic-NADPH (purple) ribose and ribose phosphate and DfrB. The waters and hydrogen bonding interactions associated with the extended B-NADPH are shown in green and those associated with tricyclic NADPH are shown in black. Panel C shows the superposition of the two structures, highlighting the significant structural changes that the protein must undergo to accommodate the two NADPH anomers.

The transformation from the extended β-NADPH to the condensed alpha and tNADPH conformation is possible by the flexibility and plasticity of the internal NADPH phosphates. These phosphates reorient to form a hydrogen-bonding interaction with Gln 95 backbone instead of a 2.6Å hydrogen bond with a water networked between the sidechain of Asn 18 and an Asp 120 coordinated water of β-NADPH. This reorientation maintains a 2.6Å

hydrogen bonding interaction with Thr 46 and Thr 96, although the latter interacts with the phosphate through a different plane (Figure 22).

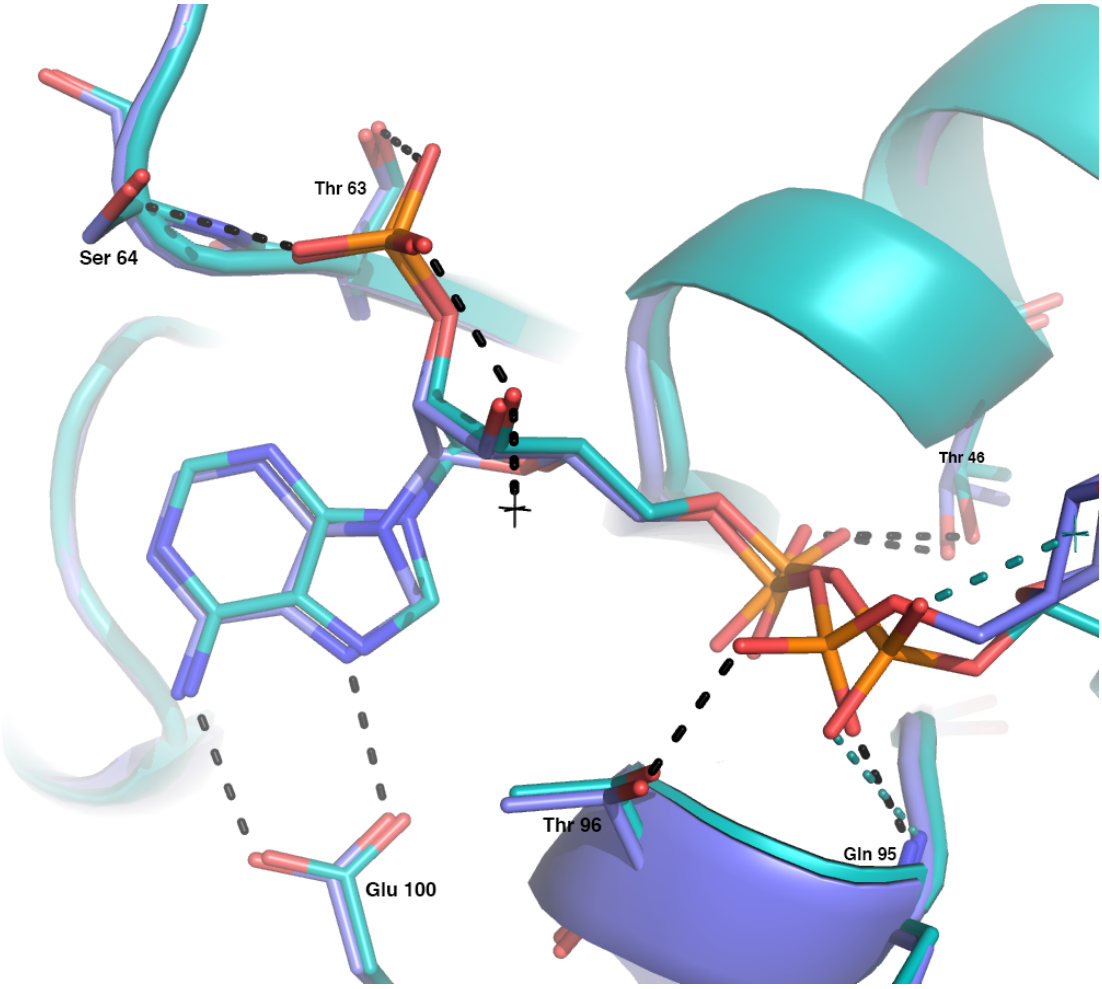

Figure 22 The interaction of the internal phosphates of beta- (green) and tricyclic- (purple) NADPH, the bonding interactions are shown in green and black, respectively. The binding interaction between the pterin ring and the protein are conserved in both beta- and tricyclic NADPH

Biochemical (Section 2.3, Figure 11) and structural analysis indicate that both tricyclic and beta-NADPH can form stable ternary structures with the DfrB and inhibitors, specifically UCP1061 and UCP1062. Interestingly, a crystal structure of UCP1006, the racemic mix of UCP1061 and UCP1062, exclusively selects beta-NADPH and its

corresponding enantiomer, potentially indicating preference for the beta-anomer complex. While the exact mechanism by which the alternate cofactor is recruited to the protein:inhibitor complex is still unknown, the binding of the inhibitor, influenced by both mutations in DfrB and the structure of the inhibitor of itself, appear to influence this selection. For example, UCP1061 and UCP1062 differ by a single stereogenic center and recruit 100% occupancy of the tricyclic-NADPH and beta-NADPH, respectively. In the structure with UCP1061, where α-NADPH is primarily stabilized by van der Waals interactions by the projection of the methyl group inhibitor into a pocket formed by Phe 92 and Thr 46. However, one of the water molecules coordinated between the NADPH and protein forms a hydrogen bond with the Phe 92 backbone, which forms extensive hydrophobic interactions with the acetylene linker (Figure 23).

In addition to the stereogenic steering of the biaryl system, a 1.5Å displacement of the acetylene linker is observed, resulting from the position of the R_P methyl (Figure 23) with the inhibitor whose linker binds nearer to the NADPH biding site UCP1061), correlates to the tricyclic NADPH. This shift in the acetylene linker was also observed with the panel of COOH-PLA's whose binding position was attributed to the coordination of waters, or direct hydrogen bonding interaction with Arg 57 (Section 2.4). While it is possible that the binding position of the acetylene linker is an artifact of the identity of the NADPH present, the potent activity and assumed potent binding of the PLAs is assumed to be preferential to that of NADPH.

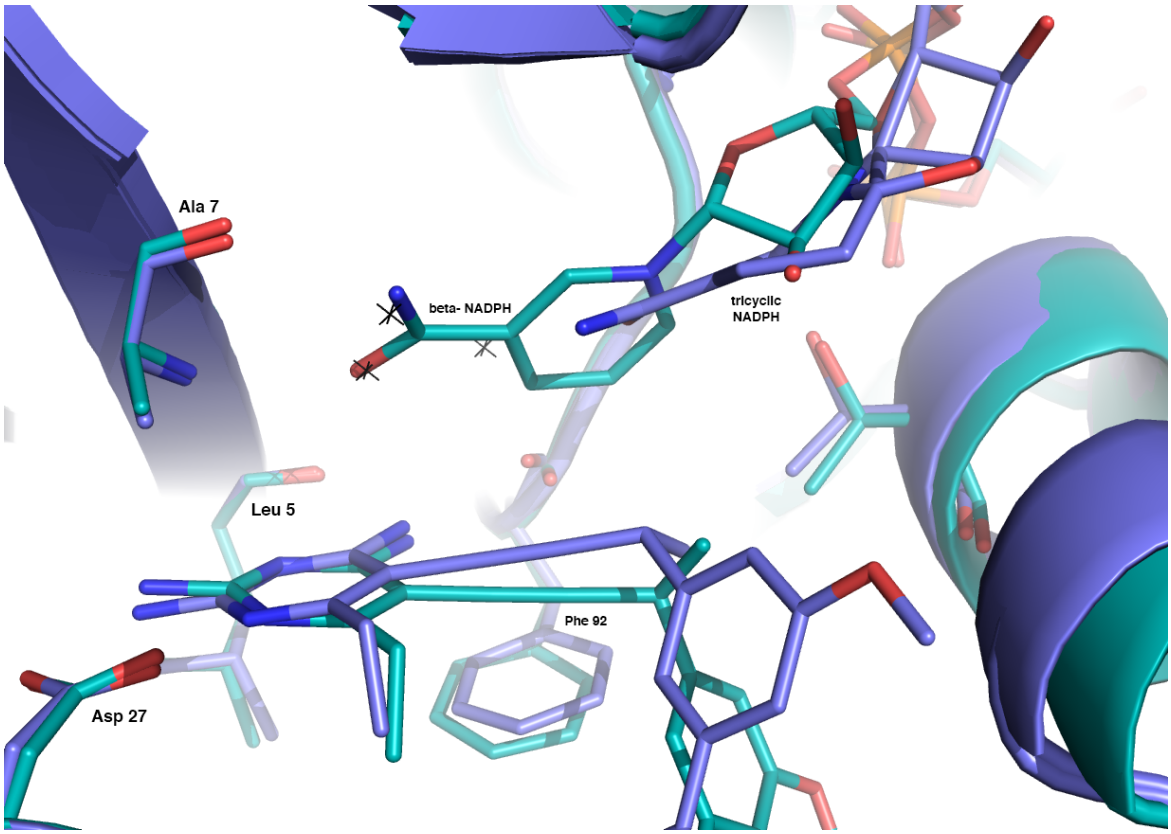

Figure 23 The binding of the PLAs, directed by a single stereogenic center, appears to influence the recruitment of the NADPH anomers. The distance between the proparyglic carbon atoms of UCP1061 (purple) and UCP1062 (green) is 1.5Å.

2.6 Conclusions

The development of a novel class of antifolates, guided by the acquisition of high-resolution crystal structures, has resulted in a class of compounds with potent enzymatic and cellular activity against *S. aureus* DHFR. These inhibitors, evolving from trimethoprim, retain the 2,4-diaminopyrimidine and linked various benzyl and biaryl system through a propargylic acetylene linker. By evaluating the aryl identities of the distal and proximal rings on the biaryl system as well as substituents on these rings and the propargylic methyl, we can elucidate a structure-activity relationship for scaffold optimization.

The first identified classes of lead PLA compounds against *S. aureus* featuring a distal-pyridine ring were optimized from a series of TMP derivatives and hydrophobic biaryl compounds. Not only did the pyridine compounds show an increase in cellular and enzymatic activity, the increased solubility gained by the polar character of the pyridine was crucial for continued lead development. B-rings and R_P substitutions further optimized the class and highlighted the important role that the propargylic methyl, the sole chiral center of the inhibitor, plays in the activity of the PLAs, therefore a panel of enatiomerically pure PLAs were developed and analyzed.

Biological and structural studies of these enantio-pure compounds show that the configuration of this chiral center provides essential conformational control of the biaryl moiety as well as increases functionality proximal to the cofactor. A noteworthy observation is that two enantiomers, containing only a single stereogenic center, drove a unique change in the adjacent NADPH binding site, leading to the binding of a modified, minor component of the natural cofactor. Continued modifications to the scaffold to try and gain ionic interaction with an active site arginine and mimic the binding of the natural substrate resulted in the generation of inhibitors further optimized against their target. By understanding the functionality of the stereogenic center and the importance of the carboxylate substitution on the distal benzyl ring, compounds that contain both of these attributes display a 32-fold increase in cellular potency over TMP as well as show good drug-like properties such as solubility and selectivity.

Finally, crystal structures of DfrB bound to cofactor and inhibitor revealed a novel configuration of NADPH. While the potential relationship between inhibitors and NADPH remains convoluted, the plasticity of the active site to accommodate this novel binding

conformation reveals a previously unknown plasticity. Additionally, the ability of the enzyme, inhibitor and tricyclic-NADPH to form a stable inhibitory complex with diminished interactions between the nicotinamide ring and acetylene linker

2.7 Acknowledgments

I would like to acknowledge Eric Scocchera (COOH-PLAs), Dr. Naren G-Dayanadan (dioxolanes and pyridines) and Dr. Santosh Keshipeddy (enantiomers) for the synthesis of the PLA compounds presented here as well as Dr. Kathleen Frey for the early pyridine compound data and Dr. Janet Paulsen and Behnoush Haijan for the expression and purification of the human DHFR. I would like to thank Dr. Bruce Donald, Dr. Eric May and their students Dr. Pablo Gainza and Jason Pattis for their discussions of NADPH. Finally, I would like to acknowledge the beamline staff at Stanford Synchrotron Radiation Lightsource (SSRL) and Brookhaven National Lab (BNL) for their assistance with crystallography data collection.

2.8 References

1. Bolstad, D. B.; Bolstad, E. S. D.; Frey, K. M.; Wright, D. L.; Anderson, A. C. Structure-Based Approach to the Development of Potent and Selective Inhibitors of Dihydrofolate Reductase from Cryptosporidium Structure-Based Approach to the Development of Potent and Selective Inhibitors of Dihydrofolate Reductase from Cryptosporidium. *J. Med. Chem.* **2008**, 6839–685.
2. Anderson, A. C. Two Crystal Structures of Dihydrofolate Reductase-Thymidylate Synthase from Cryptosporidium Hominis Reveal Protein-Ligand Interactions Including a Structural Basis for Observed Antifolate Resistance. *Acta Crystallogr. Sect. F Struct. Biol. Cryst. Commun.* **2005**, *61* (3), 258–262.
3. Pelphrey, P. M.; Popov, V. M.; Joska, T. M.; Beierlein, J. M.; Bolstad, E. S. D.; Fillingham, Y. a.; Wright, D. L.; Anderson, A. C. Highly Efficient Ligands for Dihydrofolate Reductase from Cryptosporidium Hominis and Toxoplasma Gondii Inspired by Structural Analysis. *J. Med. Chem.* **2007**, *50*, 940–950.
4. Checkley, W.; White, A. C.; Jaganath, D.; Arrowood, M. J.; Chalmers, R. M.; Chen, X. M.; Fayer, R.; Griffiths, J. K.; Guerrant, R. L.; Hedstrom, L.; et al. A Review of the Global Burden, Novel Diagnostics, Therapeutics, and Vaccine Targets for Cryptosporidium. *Lancet Infect. Dis.* **2015**, *15* (1), 85–94.
5. Toole, T. O.; Henderson, D. a; Bartlett, J. G.; Ascher, M. S.; Eitzen, E.; Friedlander, A. M.; Gerberding, J.; Hauer, J.; Hughes, J.; Mcdade, J.; et al. Updated Recommendations for Management. *JAMA, J. Am. Med. Assoc.* **2002**, *287* (17), 2236–2253.
6. Beierlein, J. M.; Frey, K. M.; Bolstad, D. B.; Pelphrey, P. M.; Joska, T. M.; Smith, A. E.; Priestley, N. D.; Wright, D. L.; Anderson, A. C. Synthetic and Crystallographic Studies of a New Inhibitor Series Targeting Bacillus Anthracis Dihydrofolate Reductase. *J. Med. Chem.* **2008**, *51* (23), 7532–7540.
7. Viswanathan, K.; Frey, K. M.; Scocchera, E. W.; Martin, B. D.; Swain, P. W.; Alverson, J. B.; Priestley, N. D.; Anderson, A. C.; Wright, D. L. Toward New Therapeutics for Skin and Soft Tissue Infections: Propargyl-Linked Antifolates Are Potent Inhibitors of MRSA and Streptococcus Pyogenes. *PLoS One* **2012**, *7* (2), 1–9.
8. Lamb, K. M.; Lombardo, M. N.; Alverson, J.; Priestley, N. D.; Wright, D. L.; Anderson, A. C. Crystal Structures of Klebsiella Pneumoniae Dihydrofolate Reductase Bound to Propargyl-Linked Antifolates Reveal Features for Potency and Selectivity. *Antimicrob. Agents Chemother.* **2014**, *58* (12), 7484–7491.
9. Paulsen, J. L.; Liu, J.; Bolstad, D. B.; Smith, A. E.; Priestley, N. D.; Wright, D. L.; Anderson, A. C. In Vitro Biological Activity and Structural Analysis of 2,4-Diamino-5-(2-Arylpropargyl)pyrimidine Inhibitors of Candida Albicans. *Bioorganic Med. Chem.* **2009**, *17* (14), 4866–4872.
10. G-Dayanandan, N.; Paulsen, J. L.; Viswanathan, K.; Keshipeddy, S.; Lombardo, M. N.; Zhou, W.; Lamb, K. M.; Sochia, a E.; Alverson, J. B.; Priestley, N. D.; et al. Propargyl-Linked Antifolates Are Dual Inhibitors of Candida Albicans and Candida Glabrata. *J. Med. Chem.* **2014**, *57* (6), 2643–2656.

11. Chen, F.; Larsen, M. B.; Sánchez, C.; Wiborg, O. The S-Enantiomer of R,S-Citalopram, Increases Inhibitor Binding to the Human Serotonin Transporter by an Allosteric Mechanism. Comparison with Other Serotonin Transporter Inhibitors. *Eur. Neuropsychopharmacol.* **2005**, *15*, 193–198.
12. Orr, S. T. M.; Ripp, S. L.; Ballard, T. E.; Henderson, J. L.; Scott, D. O.; Obach, R. S.; Sun, H.; Kalgutkar, A. S. Mechanism-Based Inactivation (MBI) of Cytochrome P450 Enzymes: Structure-Activity Relationships and Discovery Strategies to Mitigate Drug-Drug Interaction Risks. *J. Med. Chem.* **2012**, *55* (11), 4896–4933.
13. Gant, T. G. Using Deuterium in Drug Discovery: Leaving the Label in the Drug. *J. Med. Chem.* **2014**, *57* (9), 3595–3611.
14. Frey, K. M.; Liu, J.; Lombardo, M. N.; Bolstad, D. B.; Wright, D. L.; Anderson, A. C. Crystal Structures of Wild-Type and Mutant Methicillin-Resistant Staphylococcus Aureus Dihydrofolate Reductase Reveal an Alternate Conformation of NADPH That May Be Linked to Trimethoprim Resistance. *J. Mol. Biol.* **2009**, *387* (5), 1298–1308.
15. Frey, K. M.; Lombardo, M. N.; Wright, D. L.; Anderson, A. C. Towards the Understanding of Resistance Mechanisms in Clinically Isolated Trimethoprim-Resistant, Methicillin-Resistant Staphylococcus Aureus Dihydrofolate Reductase. *J. Struct. Biol.* **2010**, *170* (1), 93–97.
16. Keshipeddy, S.; Reeve, S. M.; Anderson, A. C.; Wright, D. L. Non-Racemic Antifolates Stereo-Selectively Recruit Alternate Cofactors and Overcome Resistance in S. Aureus. *J. Am. Chem. Soc.* **2015**.
17. Copeland, R. A.; Pompliano, D. L.; Meek, T. D. Drug – Target Residence Time and Its Implications for Lead Optimization. *Nature Drug Disc* **2006***, 5,* 730-740.
18. Koch, A. E.; Burchall, J. J. Reversal of the Antimicrobial Activity of Trimethoprim by Thymidine in Commercially Prepared Media. *Appl. Environ. Microbiol.* **1971**, *22* (5), 812–817.
19. Frey, K. M.; Georgiev, I.; Donald, B. R.; Anderson, A. C. Predicting Resistance Mutations Using Protein Design Algorithms. *Proc. Natl. Acad. Sci. U. S. A.* **2010**, *107* (31), 13707–13712.
20. Burchall, J.; Hitchings, G. Inhibitor Binding Analysis of Dihydrofolate Reductases from Various Species. Mol. Pharmacol. **1965**, *1*, 126–136.
21. Kopytek, S.; Dyer, J.; Knapp, G.; Hu, J. Resistance to methotrexate due to AcrAB-dependent export from Escherichia coli. *Antimicrob. Agents Chemother*. **2000**, *44*, 3210–3212.
22. Kruszewska, H.; Zareba, T.; Tyski, S. Antimicrobial activity of selected non-antibiotics - activity of methotrexate against *Staphylococcus aureus* strains. *Acta Polym. Pharm*. **2000**, *57S*, 117–119.
23. O'Shea, R.; Moser, H. Physicochemical properties of antibacterial compounds: implications for drug discovery*. J. Med. Chem.* **2008**, *51*, 2871–2878.
24. Scocchera, E.; Reeve, S. M.; Keshipeddy, S.; Lombardo, M. N.; Hajian, B.; Sochia, A. E.; Alverson, J. B.; Priestley, N. D.; Anderson, A. C.; Wright, D. L. Charged

Nonclassical Antifolates with Activity Against Gram-Positive and Gram-Negative Pathogens. *ACS Med. Chem. Lett.* **2016**, *7*, 692-696.
25. Lamb, K.; G-Dayanandan, N.; Wright, D.; Anderson, A. Elucidating Features That Drive the Design of Selective Antifolates Using Crystal Structures of Human Dihydrofolate Reductase. *Biochemistry* **2013**, *52*, 7318–7326.
26. Pankey, G.; Sabath, L. Clinical Relevance of Bacteriostatic versus Bactericidal Mechanisms of Action its the Treatment of Gram-Positive Bacterial Infections. *Clin. Infect. Dis.* **2004**, *38*, 864–870.
27. Oppenheimer, N. J.; Arnold, L. J.; Kaplan, N. O. A Structure of Pyridine Nucleotides in Solution. *Proc. Nat. Acad. Sci. USA* **1971**, *68*, 3200-3205
28. Oppenheimer, N. J.; Kaplan, N. O. Structure of the Primary Acid Rearrangement Product of Reduced Nicotinamide Adenine Dinucleotide (NADH). *Biochemistry* **1974**, *13* (23), 4675–4685.

Chapter 3

Protein Design Algorithms Predict Viable Resistance to a Lead PLA

3.1 Computer Algorithms to Predict Drug Resistance

Mutational resistance is a common mechanism conferring resistance observed in nearly every class of antibiotics as well as chemotherapeutics and antivirals. Being able to predict mutations *in-silico* and understand the specific mechanisms in which a target can mutate and confer resistance would allow for the development of more successful and robust therapeutics. Advancements in computational biology have fostered the development of algorithms capable of producing these outcomes. Minimally, a successful algorithm would predict resistance mutations that maintain enzyme function while reducing inhibitor affinity. However, a more powerful algorithm would also predict mutations that maintain the fitness of the pathogen and are therefore likely to be selected *in vitro* or *in vivo*. Predicting "fit" mutations is a significant challenge because the variables that contribute to fitness in an organism are complex and often unknown. Additionally, a successful algorithm would predict novel mutations that are responsive to novel compounds. A prospective strategy such as this would be especially effective in the discovery of therapeutics for which it is difficult to generate resistant cells *in vitro*.

Previous attempts to predict mutational drug resistance have been reported. One study optimized molecular dynamics and thermodynamic integration calculations to reproduce experimentally derived data and therefore computationally predict the effects of mutations at two well characterized amino acids on the binding of a small molecule inhibitor to the P38α MAP kinase[1]. Others, focused heavily on HIV proteases, validate combinations of various computational methods by correlating their results to obtained *in-vitro* mutant or

clinical data for approved therapeutics. As these studies are retrospective analyses, often of known mutations that arise under pressure from known drugs, they do not address the problem of prospectively predicting a fit mutation[2-4].

3.2 Prediction of resistance mutations by K* in OSPREY

In this chapter, we report the application of the structure-based protein design algorithm, K* in OSPREY, to identify prospective single nucleotide polymorphisms (SNP) that confer resistance to UCP1006, Figure 1, a lead PLA. In previous work[5], the structure-based K* algorithm in the OSPREY protein design suite[6,7] was used to predict double mutations in *S. aureus* DHFR that confer resistance to the older generation PLA. Of the top 10 predicted mutations, all of them contained mutations at Phe 92 and the top 7 contained mutations at Val 31, with Val31Tyr prevailing; the remaining three mutations occurred at Ile 50. A detailed biochemical and structural analysis of the top three mutations (V31Y/F92I, V31Y/F92V and V31Y/F92S) validated K*'s ability to accurately the effect of mutations on enzyme fitness and inhibition**.**

Bacterial DHFR, specifically *S. aureus*, is an ideal model system for these predictions as the development of a single amino acid mutation results in trimethoprim resistance; higher levels of resistance are conferred by the accumulation of a second mutation[8]. As we continue to develop PLAs that overcome the molecular mechanisms of resistance to TMP[9], it would be useful to predict mutations that may arise for this new class of antifolates. Using ratios of positive design scores that predict binding of the substrate, dihydrofolate, and negative design scores that predict binding of the inhibitor, OSPREY/K* identified catalytically competent resistance mutations[6,7].

The protein design algorithm, K* in OSPREY[6], was used to identify mutations characterized by single nucleotide polymorphisms (SNPs) that maintain binding to the substrate, dihydrofolate, while conferring resistance to the UCP1006 (Figure 1). Nine active site residues (Leu 5, Val 6, Leu 20, Leu 28, Val 31, Thr 46, Ile 50, Leu 54 and Phe 92) were allowed to either maintain their wild type identity or to mutate to a restricted group of residues that involve only a single nucleotide polymorphism (Table 1).

K* searches were performed on both the substrate (DHFR:NADPH:dihydrofolate) and inhibitor (DHFR:NADPH:UCP1006) ternary complexes. K* scores approximate the binding affinity (K_a) and are computed as a ratio of Boltzmann-weighted partition functions for rotamer-based conformational ensembles of the bound protein:inhibitor complex, free protein and free ligand. Since higher K* scores predict greater affinity, the ideal mutation would have a high score for DHF and a low or zero score for UCP1006. The wild-type sequence was ranked 18th with a design ratio of 1.95 x 10^6 (Table 1). Mutants that had both (I) higher ranking than the wild-type and (II) a good predicted binding affinity to DHF (i.e., positive design score) were considered as resistant mutants. Four mutations (V31L, V31I, L5I, L5V) exhibiting high ratios for the scores representing positive (binding to DHF) and negative design (binding to inhibitor) are shown in Table 2.

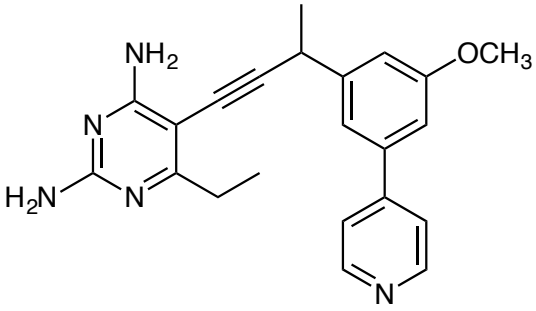

Figure 1 Structure of UCP1006

Table 1 K* Rankings by Positive/Negative Design Ratio

K* Rank	Single Nucleotide Mutation	Substrate Positive design K* Score	Negative design K* Score	Ratio: positive / negative design
1	V31L	2.16E+41	3.04E+19	7.11E+21
2	V31I	4.87E+36	8.18E+14	5.95E+21
3	L5I	6.06E+39	3.54E+24	1.71E+15
4	L5V	4.01E+44	3.44E+30	1.16E+14
5	L54R	6.31E+43	1.60E+30	3.94E+13
6	L20F	6.06E+20	1.75E+07	3.46E+13
7	V31D	1.54E+41	5.65E+32	2.72E+08
8	L5Q	2.84E+44	1.20E+36	2.36E+08
9	V31A	7.32E+40	7.86E+33	9.31E+06
10	V6G	3.92E+42	4.27E+35	9.18E+06
11	I50L	5.18E+38	5.69E+31	9.10E+06
12	F92S	2.09E+43	2.52E+36	8.32E+06
13	L54Q	2.62E+42	3.21E+35	8.14E+06
14	V31G	2.64E+40	3.38E+33	7.80E+06
15	T46A	2.88E+42	5.27E+35	5.46E+06
16	V61	1.10E+43	4.01E+36	2.75E+06
17	L28M	3.27E+42	1.58E+36	2.07E+06
18	**WT**	**7.16E+42**	**3.66E+36**	**1.96E+06**
19	T46S	4.93E+42	3.46E+36	1.42E+06
20	L28F	2.25E+42	1.73E+36	1.30E+06
21	L28W	1.29E+43	1.01E+37	1.28E+06
22	L20S	3.57E+41	2.95E+35	1.21E+06
23	L20I	3.04E+42	2.94E+35	1.03E+06
24	L20V	7.43E+41	7.40E+35	1.01E+06
25	V6A	4.71E+42	6.07E+36	7.76E+05
26	L54V	1.46E+41	2.68E+35	5.44E+05
27	L28S	1.34E+41	3.74E+35	3.59E+05

28	V6D	1.18E+43	6.05E+37	1.95E+05
29	V6L	7.26E+42	6.47E+37	1.12E+05
30	F92V	8.18E+40	2.80E+36	2.29E+04
31	I50V	2.49E+42	1.74E+38	1.43E+04
32	L28V	3.19E+39	2.37E+35	1.35E+04
33	F92I	8.91E+40	8.48E+36	1.05E+04
34	F92C	1.02E+40	5.37E+36	1.90E+03
35	I50S	3.07E+41	2.37E+38	1.30E+03
36	I50T	1.11E+42	9.85E+38	1.13E+03
37	I50N	6.81E+41	1.53E+39	4.46E+02
38	I50M	1.00E+40	7.50E+37	1.33E+02
39	F92L	4.02E+37	4.20E+36	9.59E+00
40	L5R	4.21E+34	4.27E+35	9.88E-02
41	T46I	5.05E+36	2.25E+42	2.25E-06
42	V6F	0.00E+00	2.94E+36	0.00E+00
43	V31F	0.00E+00	8.69E-11	0.00E+00
44	T46R	0.00E+00	0.00E+00	0.00E+00
45	T56K	0.00E+00	1.14E+14	0.00E+00
46	F92Y	0.00E+00	3.10E+32	0.00E+00
47	I50F	0.00E+00	3.37E+35	0.00E+00

3.3 Biochemical and Structural Evaluation of K* Predicted Mutants

To validate the positive and negative design results from K*, site-directed mutagenesis was used to create the top four ranked mutant DHFR enzymes: Sa(V31L), Sa(V31I), Sa(L5I), and Sa(L5V). Michaelis-Menten kinetics (Table 2) reveal that the enzymes maintain their catalytically competency with only minor losses in k_{cat}/K_M. The activity of the mutant enzymes validates the success of the positive design component of the computational search, meanwhile drastically decreased activity of the inhibitor against the mutant enzyme validates the negative design component. Resistance, measured by

loss in K_i, ranged from 2-fold to 58-fold, with the top-ranked mutants (V31L and V31I) conferring the greatest level of resistance. In fact, K* accurately ranked the mutations as their experimental ratio of inhibition constants correlates with their K* design ratio.

Table 2 Characterization of wild-type and mutant enzymes

Enzyme	K* Ratio Rank	K* design ratio	k_{cat}/K_M	Fold Loss[b] (K_i^{mut}/K_i^{wt}) UCP1006
Sa (wt)	18	1.96 E+06	6.1 ± 0.3	n/a
Sa (V31L)	1	7.11 E+21	1.60 ± 0.06	58
Sa (V31I)	2	5.95 E+21	1.74 ± 0.07	36
Sa (L5I)	3	1.71 E+15	2.24 ± 0.1	4.4
Sa (L5V)	4	1.16 E+14	1.8 ± 0.1	1.9

The lowest energy conformations of the top-ranked mutations, SaV31L and SaV31I, were compared to the crystal structure of wild-type SaDHFR:NADPH:UCP1006 to understand the basis of the resistance prediction[9]. Carbons Cδ1 and Cδ2 in Leu 31 are predicted to displace Phe 92, most likely to avoid steric hindrance with the phenyl side chain (Figures 2 and 3). In addition, these carbons are observed to sterically interfere with the pyrimidine ring, displacing it from its corresponding position in the wild-type structure. Both of these steric interactions are expected to significantly weaken inhibitor binding.

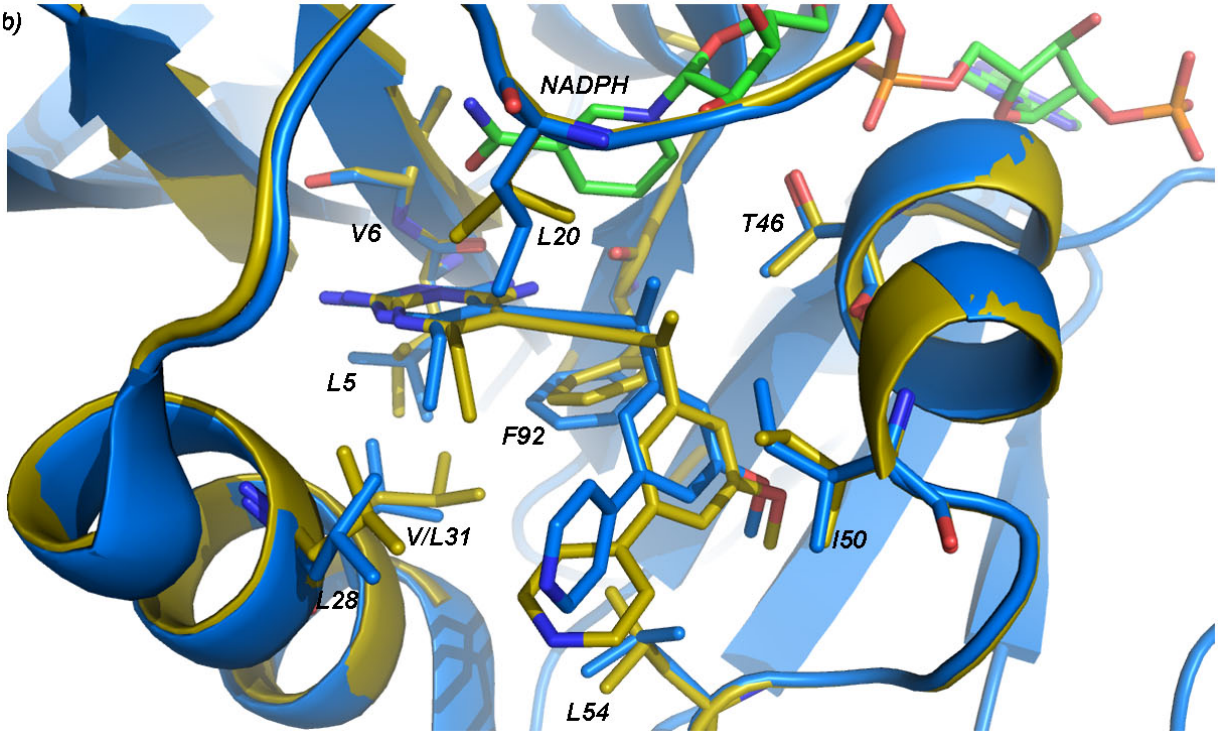

Figure 2 Comparison of the structures of wild-type SaDHFR bound to NADPH and UCP1006 (PDB ID: 3SGY, blue) with the K*-predicted lowest-energy structure of SaDHFR (V31L) (yellow). All residues allowed to be flexible and to mutate during the K* prediction are shown in yellow stick form. The cofactor, NADPH, is shown in green.

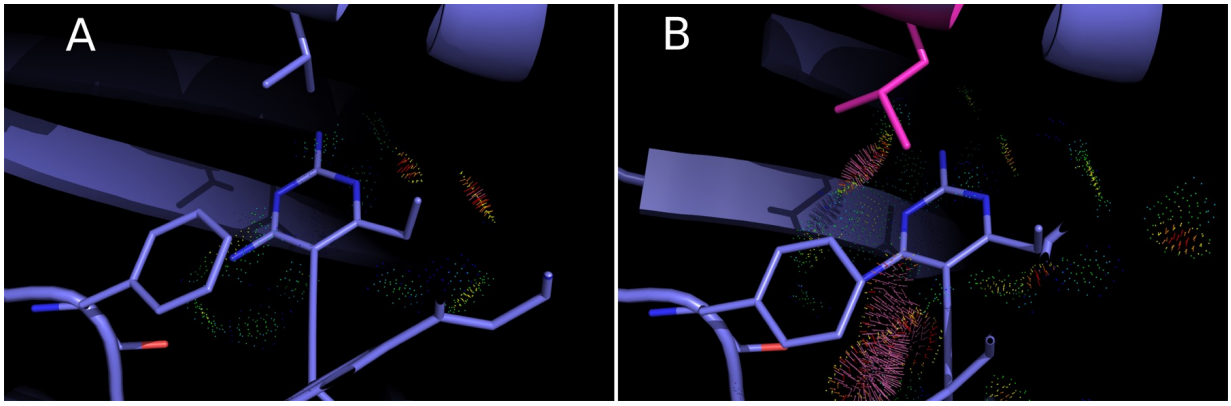

Figure 3 Computationally-predicted effect of the V31L mutation on inhibitor binding. A) the wild-type *S. aureus* DHFR:inhibitor complex (shown in blue) and B) the computationally predicted model of the mutant V31L in complex with the inhibitor (in which the mutant is shown in magenta and the complex is shown in blue). In addition to V31 and the inhibitor, F92 is also shown in a stick model, while the remainder of the protein is shown in ribbon form.

3.4 Selection of UCP1006^{R} Mutants

3.4a Microbiological Evaluation of Generated Mutants

In order to show the application of these predictions to a living pathogen, UCP1006^{R} MRSA strains were generated and selected by the bacteria under pressure from UCP1006 and probed for mutations in the endogenous DHFR (*dfrB*). A first round of selection revealed a single F98Y mutation. F98Y (a TTT to TAT transversion mutation), a mutation that has been clinically identified as a mechanism that *S. aureus* DHFR confers resistance to TMP, has a resistance frequency of 1.21×10^{-12}. The F98Y strain was then exposed to a second round of mutant selection experiments. Five of the generated nine colonies of surviving bacteria yielded the computationally predicted V31L mutation (a GTT to CTT transversion mutation). An overall frequency of 7.56×10^{-24} reflects the step-wise mechanisms in which the mutations developed. One of the nine colonies yielded V31G (14th in the ranked list, with a 10-fold increase in the K* ratio over the wildtype) and the remaining three colonies possessed only F98Y. Both the single F98Y and double V31L/F98Y mutant strains were characterized to evaluate antimicrobial susceptibility and relative fitness. Trimethoprim, whose resistance profile includes the F98Y mutation, was included as a reference (Table 3). A comprehensive evaluation of all mutant strains generated in these and additional selection experiments are characterized in Chapter 4.

Table 3 Characterization of Strain Susceptibility and Fitness

Strain	MIC UCP1006 (μg/mL)(fold loss)	MIC TMP (μg/mL) (fold loss)	Relative Fitness	Doubling Time (min)
Wild-type	0.0781	0.3123	1	22.5
F98Y	2.5 (32)	10 (32)	0.98	23.2
V31L, F98Y	20 (256)	40 (128)	0.86	25.4

UCP1006 and TMP have MIC values of 2.5 μg/mL and 10 μg/mL for the F98Y strain, respectively, representing a 32-fold loss when compared with the wild-type ATCC 43300 strain. The addition of the V31L mutation confers an additional 8-fold loss for UCP1006 and 4-fold loss for TMP, resulting in total 256- and 128-fold losses, respectively. As observed previously, the Sa(F98Y) DHFR mutation does not reduce the fitness of the strain[10,11]. The presence of the V31L/F98Y mutation reported here results in minimal (14 %) loss of fitness, as measured by a pair-wise fitness assay. Log-phase cell growth was minimally affected by the presence of the single F98Y or double V31L/F98Y mutation with doubling times at 22.5 minutes for the wild-type strain and 23.2 and 25.4 minutes for the mutants, respectively.

3.4b Biochemical Evaluation of Generated Mutants

In order to understand why the V31L mutation arises only in the background of the F98Y mutation, we examined detailed inhibition and kinetic data for the enzymes. Here, we also included the F98Y mutation and data for trimethoprim as a comparator. The Sa(F98Y) mutation has more pronounced effects on trimethoprim, resulting in 38- and 5-fold losses in K_i against trimethoprim and UCP1006, respectively. However, the Sa(V31L) mutation affects UCP1006 more significantly, resulting in 15- and 60-fold losses in K_i against trimethoprim and UCP1006 (Table 4). The Sa(V31L,F98Y) double mutant clearly confers much greater resistance with a 148-fold loss in K_i for trimethoprim and an 189-fold loss in K_i for UCP1006.

Michaelis-Menten constants, determined for each of the enzymes (Table 4), reveals a compensatory relationship between the mutations. The K_M value for DHF is reduced from the wild-type value (17.5 μM) by 2-fold for Sa(F98Y)DHFR to 8.4 μM while the same

value for Sa(V31L) DHFR is increased by 2.4-fold to 42.9 μM. In combination, the Sa(V31L/F98Y) DHFR restores the K_M for DHF to 4.1 μM. Interestingly, the K_M value for NADPH for Sa(F98Y) increases to 56.8 μM from the wild-type value of 32.6 μM and the K_M value for NADPH in Sa(V31L) decreases to 15.6 μM. The double mutant maintains the decreased K_M of Sa(V31L) and has an overall lower K_M relative to wild-type at 22.3 μM. Taken together, the data show that while F98Y and V31L negatively affect NADPH and DHF, respectively, the two mutations in combination restore the K_M values to wild-type levels. Additionally, the k_{cat}/K_M value for the double mutant is increased to 10.9 μM^{-1}.

Table 4: Characterization of MRSA Generated Mutant Enzymes

DHFR	TMP K_i, nM	UCP1006 K_i, nM	DHF K_M, μM	NADPH K_M, μM	k_{cat}	k_{cat}/K_M
WT	3.5 ± 0.5	2.8 ± 0.2	17.5 ± 2	32.6 ± 4	106.9 ± 2	6.1 ± 0.3
F98Y	131 ± 4	13 ± 1	8.4 ± 0.7	56.8 ± 5	44.7 ± 0.4	5.33 ± 0.08
V31L	54 ± 2	170 ± 20	42.9 ± 3	15.6 ± 3	68.8 ± 2	1.60 ± 0.06
V31L, F98Y	520 ± 30	530 ± 30	4.1 ± 0.8	22.3 ± 2	44.8 ± 2	10.9 ± 0.8

3.5 Structural Analysis of Sa (V31L, F98Y) DHFR

The data in Tables 2 and 4 indicate that the mutations have a direct influence on substrate and cofactor binding as well as inhibitor potency. In order to understand the structural effects of the mutations, we determined a crystal structure of the double mutant enzyme. Crystals of Sa (V31L, F98Y) DHFR produced diffraction amplitudes to 2.1 Å when co-crystallized with NADPH and a propargyl-linked antifolate that is structurally similar to UCP1006. The structure was solved using Fourier methods based on the model of the single mutant Sa(F98Y) bound to NADPH and a propargyl-linked antifolate (PDB

ID:3F0U)[12]. The Sa(V31L, F98Y) structure features the standard extended form of NADPH but lacks the PLA present during co-crystallization.

Comparisons of the Sa (V31L, F98Y) structure with the structure of wild-type enzyme bound to UCP1006 reveal a structural basis of resistance indicated by significant conformational changes induced by the presence of the two mutations. The most significant amino acid reorientations are observed between Phe 92, Val 31 and the binding site of the diaminopyrimidine moiety of UCP1006**.** The major change centers on Leu 31 that projects 2.0 Å further into the active site than the wild-type Val 31 residue, resulting in a corresponding 2.3 Å shift in Phe 92 into the active site and 1.4 Å shift of the backbone carbonyl (Figure 2a). This new Phe 92 orientation restricts the side chain from adopting the position needed for ligand binding and disrupts stabilizing hydrophobic interactions with the acetylene linker. The shift of the Phe 92 carbonyl also results in the loss of a hydrogen bond to the 4-amino group of the pyrimidine. Additionally, Leu 31 is 2.2 Å from the 6-ethyl substituent of the diaminopyrimidine, indicating potential repulsive steric interactions.

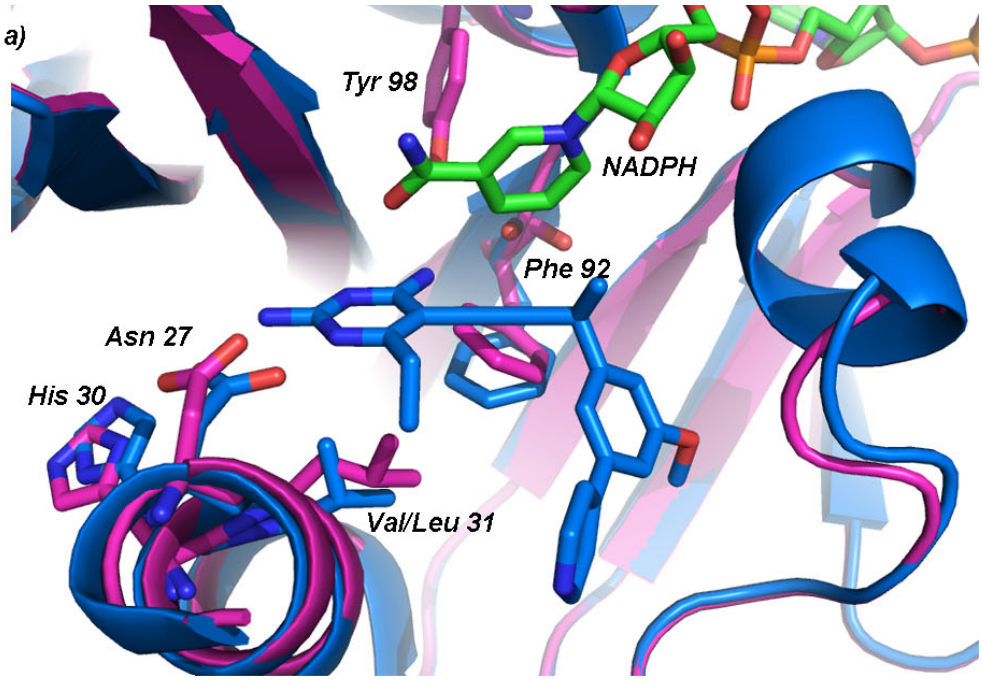

Figure 4 Crystal structures of the wild-type and mutant enzymes show conformational changes at Phe 92 and His 30. **a)** Superposition of the structures of Sa(wt):NADPH:UCP1006 from PDB ID: 3SGY (blue) with Sa(V31L,F98Y):NADPH (magenta)

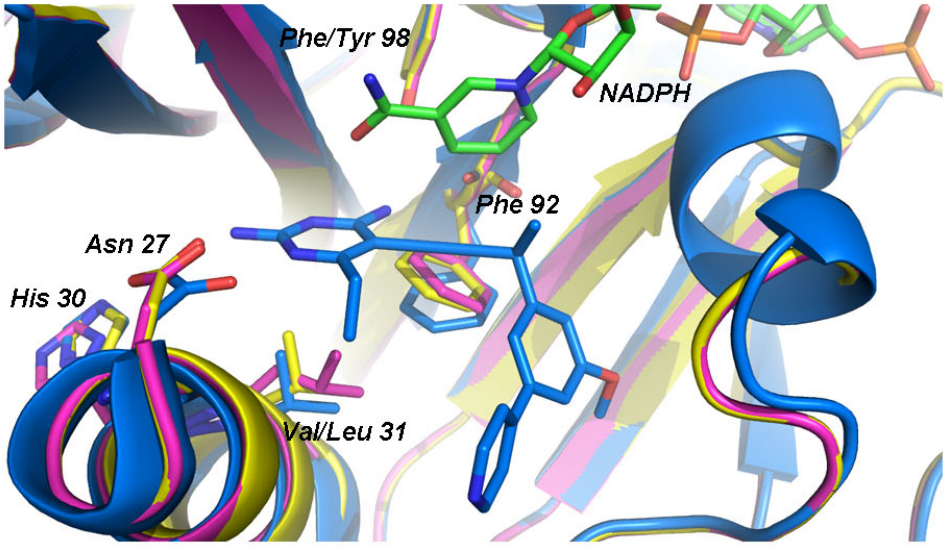

Figure 4 Crystal structures of the wild-type and mutant enzymes show conformational changes at Phe 92 and His 30. **b)** Superposition of the structures of Sa(wt):NADPH:UCP1006 from PDB ID 3SGY (blue) with Sa(F98Y):NADPH (yellow) and Sa(V31L/F98Y):NADPH (magenta).

Furthermore, the B-helix, adjacent to the active site and possessing critical amino acids for ligand binding, shifts 0.4 Å away from the active site. Distances between the ligand and amino acids Asn 25, Asp 27, His 30 and Leu 34 are increased by 0.4 Å, concomitantly reducing hydrogen bonding and van der Waals interactions essential for stability and ligand binding. Moreover, the shift in the B-helix results in a 1.1 Å shift in the imidazole ring of His 30. The shifted His 30 side chain extends the binding site, allowing for a glycerol molecule to displace a water molecule that typically provides stabilizing hydrogen bonds between the pyrimidine amino group of UCP1006 and the His 30 imidazole (Figure 5). A similar disruption of the water network has been previously shown in a crystal structure of the clinically observed resistance mutant Sa (H30N, F98Y) with NADPH and a propargyl-linked antifolate13. In combination, the observations for Phe 92, Leu 31 and the B-helix explain the lower affinity of UCP1006 for the mutant enzyme.

The Sa(V31L, F98Y) enzyme maintains catalytic competency. Comparisons of the Sa(V31L/F98Y) structure with wild-type Sa/NADPH/DHF (PDB ID: 3FRD)[14] indicates that a shift in the Phe 92 peptide carbonyl would have little or no effect on DHF binding or turnover since there are no direct interactions between the two groups. Any minor steric interactions between Phe 92 and the pterin ring of DHF may be compensated by the additional interactions in the glutamate tail that remain undisturbed.

In order to verify which structural effects result from the presence of the mutations and which result from enzyme lacking a bound ligand, we determined the structure of Sa(F98Y)DHFR bound only to NADPH. Comparisons of the structures of binary Sa(F98Y):NADPH, Sa(F98Y/V31L):NADPH and ternary Sa:NADPH:UCP1006 indicate that the reorientations of Phe 92 and His 30 are due to the presence of the mutations.

Like the Sa(F98Y/V31L):NADPH structure, the Sa(F98Y):NADPH structure features the same 0.4 Å shift of the B-helix away from the active site. However, the conformation of Phe 92 in the Sa(F98Y/V31L) structure appears to be influenced by the V31L mutation as the conformation of this residue in the Sa(F98Y) structure is approximately 0.5 Å closer to that observed in the ternary structure. Similarly, the V31L mutation influences the conformation of His 30 as a comparison of the Sa(F98Y):NADPH and ternary (Sa:NADPH:UCP1006) structures shows that the His 30 conformation is the same (Figure 2b).

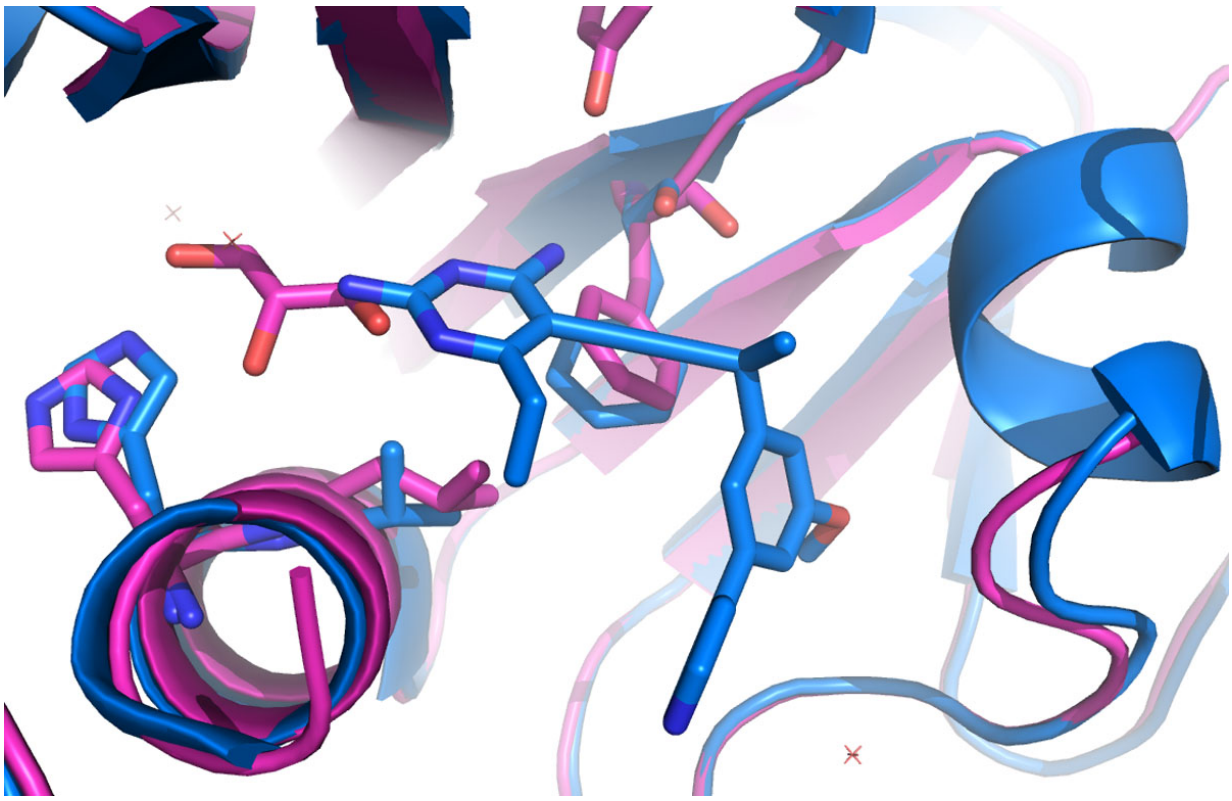

Figure 5 A molecule of glycerol is observed to bind in the active site of the structure of Sa(F98Y/V31L):NADPH. The Sa(F98Y/V31L) structure is shown in magenta, the 3SGY structure (Sa(wt):NADPH:**1**) structure is shown in blue for reference. The molecule of glycerol replaces the 2-amino group and a water molecule found in the wild-type structure.

Comparisons of the crystal structure of Sa(F98Y/V31L):NADPH with the lowest energy predicted structure of the K*-predicted single V31L mutant (Figure 1) shows a conservation of the effect of the V31L mutation on Phe 92. The predicted structure also indicates a steric interaction between Leu 31 and the C_6-ethyl substituent of the pyrimidine ring of UCP1006, which compliments the crystallographic results. Incidentally, when K* was previously used to predict resistance mutations with another propargyl-linked antifolate that maintains the same atoms as UCP1006 other than possessing a methyl instead of an ethyl group at the C_6 position of the pyrimidine ring, the Val 31 mutants ranked lower than the Leu 5 mutations. These results further validate that the steric interaction between Leu 31 and the ethyl group specifically contribute to resistance.

3.6 Conclusions

In summary, the K* algorithm in OSPREY was successfully used to predict unique single amino acid mutations in the active site of *S. aureus* DHFR that confer resistance to UCP1006. Four of the predicted mutant enzymes were created and shown to be catalytically competent and resistant to UCP1006, with the top-ranked mutant having a 58-fold reduction in inhibitor potency. Excitingly, the computational predictions were shown to not only be biochemically validated, but also selected in the bacteria under antibiotic pressure as the top-ranked mutation, V31L, was selected in the background of an F98Y mutation, which has been clinically observed. Exploration of the enzymatic fitness of this novel double mutant revealed a compensatory relationship between the single F98Y and V31L mutations that results in a doubly mutated enzyme with fitness comparable to the wild-type enzyme. Consideration of the cellular fitness revealed that the double mutant strain only suffered a slight loss in fitness over both the progenitor

strain and the previously characterized F98Y strain. Crystal structures of the double mutant enzyme revealed the structural basis of compound resistance.

The mutation V31L emerged as the top-ranked SNP that maintained dihydrofolate binding while conferring inhibitor resistance by perturbing Phe 92 and sterically interfering with the C_6-ethyl group of the pyrimidine ring. Interestingly, there is a strong correlation between the current results and those obtained in the first application of K* to identify double mutants of SaDHFR that confer resistance. In the previous study[5], the seven top-ranked mutations were variants of Val 31 and Phe 92; a crystal structure of the V31Y/F92I mutant enzyme shows that the F92I mutation reduces van der Waals interactions and the V31Y mutation introduces destabilizing steric bulk. Overall, it is striking that the same structural effect is selected with both applications of K* whether it is applied to identify double or SNP mutations.

Having validated the mutational prediction capabilities of K*/OSPREY via bacterial selection of the predicted mutants, the algorithm could potentially be applied to many different research areas. Specifically, the computational prediction of drug-resistance mutations could be valuable in cases where it is more difficult to raise mutant strains or cell lines in vitro, such as with viruses or cancer cell lines. Overall, the extension of the computational prediction of drug resistance to observations of biologically relevant mutants provides new opportunities in drug discovery, especially for those targets that are most affected by mutational resistance.

3.7 Acknowledgements

The K* algorithm in the OSPREY Protein Design Suite was developed by Dr. Bruce Donald and experiments were run by his students Pablo Gainza and Dr. Ivelin Georgiev. The initial single mutant enzyme construction, characterization and F98Y, V31L:NADPH:UCP1006 crystal growth was done by Dr. Kathleen Frey. I would also like to acknowledge the staff at beamline X4A of the National Synchrotron Light Source at Brookhaven National Laboratory for their assistance with X-ray data collection.

3.8 References

1. Zhu, S.; Travis, S.; Elcock, A. Accurate Calculation of Mutational Effects on the Thermodyamics of Inhibitor Binding to p38α MAP Kinase: A combined computational and experimental study. *J. Chem. Theory Comput.* **2009,** *9*, 3151-3164.
2. Ishikita, H.; Warshel, A. Predicting Drug-Resistant Mutations of HIV Protease. *Angew. Chem. Int. Ed.* **2008,** *47*, 697-700.
3. Hao, G.-F.; Yang, G.-F.; Zhan, C.-G. Computational mutation scanning and drug resistance mechanisms of HIV-1 protease inhibitors. *J. Phys. Chem. B* **2010,***114*, 9663-9676.
4. Safi, M.; Lilien, R. Efficient a Priori Identification of Drug Resistant Mutations Using Dead-End Elimination and MM-PBSA. *J. Chem. Inf. Model.* **2012,** *52*, 1529-1541.
5. Frey, K.; Georgiev, I.; Donald, B.; Anderson, A. Predicting resistance mutations using protein design algorithms. *Proc. Natl. Acad. Sci.* **2010***, 107*, 13707-13712.
6. Gainza, P. et al. OSPREY: Protein Design with Ensembles, Flexibility, and Provable Algorithms. *Meth. Enz.* **2013**, *523*, 87-107.
7. Chen, C.; Georgiev, I.; Anderson, A; Donald, B. Computational Structure-Based Redesign of Enzyme Activity. *Proc. Natl. Acad. Sci.* **2009**,*106*, 3764-3769.
8. Dale, G. et al. A single amino acid substitution in *Staphylococcus aureus* dihydrofolate reductase determines trimethoprim resistance. *J. Mol. Biol.* **1997**, *266*, 23-30.
9. Viswanathan, K. et al. Toward new Therapeutics for Skin and Soft Tissue Infections: Propargyl-linked Antifolates Are Potent Inhibitors of MRSA and *Streptococcus pyogenes*. *PLoS ONE* **2012***, 7*, e29434.
10. Frey, K.; Viswanathan, K.; Wright, D.; Anderson, A. Prospectively screening novel antibacterial inhibitors of dihydrofolate reductase for mutational resistance. *Antimicrob. Agents and Chemother.* **2012**, *56*, 3556-3562.

11. Vickers, A.; Potter, N; Fishwick, C.; Chopra, I; O'Neill. A. Analysis of mutational resistance to trimethoprim in *Staphylococcus aureus* by genetic and structural modelling techniques. *J. Antimicrob. Chemother.* **2009***, 63*, 1112-1117.
12. Frey, K. et al. Crystal Structures of Wild-type and Mutant Methicillin-resistant *Staphylococcus aureus* Dihydrofolate Reductase Reveal an Alternative Conformation of NADPH that may be linked to Trimethoprim Resistance. *J. Mol. Biol.* **2009**, *387*, 1298-1308.
13. Frey, K.; Lombardo, M.; Wright, D.; Anderson, A. Towards the Understanding of Resistance Mechanisms in Clinically Isolated Trimethoprim-resistant, Methicillin-resistant *Staphylococcus aureus* Dihydrofolate Reductase. *J. Struc. Biol.* **2010**, *170*, 93-97.
14. Oefner, C. et al. Increased hydrophobic interactions of iclaprim with *Staphylococcus aureus* dihydrofolate reductase are responsible for the increase in affinity and antibacterial activity. *J. Antimicrob. Chemother.* **2009**, *63*, 687-698.

Chapter 4

Understanding and Overcoming Mutational Resistance to Trimethoprim with Charged Antifolates

4.1 Understanding Mutational Resistance in *S. aureus*

The accumulation of amino acid mutations in the active site of the drug target is a common mechanism of antibiotic resistance implicated in the loss of clinical efficacy to antifolates, including TMP[1] and SMX[2], as well as fluoroquinolones[3]. Sulfamethoxazole resistance is conferred by the accumulation of up to thirteen mutations in the dihydropteroate synthase (DHPS) whereas a variety of mutations across the DNA gyrase A (*gyrA)* and topoisomerase A and B (*grlA* and *grlB*) results in resistance to fluoroquinolones[2,3]. The first description of mutations in the endogenous DHFR (*dfrB*) reported four sets of mutations that determined clinical TMP resistance across Europe, the UK and South America[4]. The group of mutations includes F98Y, the combinations of F98Y with H30N or H149R and a L20V, N59I and F98Y triple mutant. The single F98Y mutation resulted in a 64-fold loss in cellular potency whereas the double and triple mutants resulted in a 254-fold loss of activity. Structural studies indicate that the presence of the Tyr 98 disrupts the Phe 92 binding resulting in the loss of a hydrogen bonding interaction between the Phe 92 backbone carbonyl and the 4-amino group of the diaminopyrimidine. The formation of an interior hydrogen bond between the Tyr 98 phenol and the Leu5 backbone carbonyl, further reducing the hydrogen bonding interactions between TMP and the active site, was observed[4].

Additional studies indicate that the presence of the F98Y mutation disrupts cofactor binding and diminishes the crucial synergy between TMP and NADPH, which in turn

confers resistance[5]. More in-depth crystallographic studies looking to overcome F98Y mutation with early generation of PLAs indicates that an alternative NADPH conformation correlates with decreased activity against this enzyme[6]. While the exact mechanism by which Tyr 98 confers resistance remains convoluted, its impact on clinical antifolate resistance remains of the utmost importance. Furthermore, comprehensive biochemical and structural analysis of the clinically isolated TMP^R double mutant, Sa (H30N, F98Y) DHFR indicates that the double mutant doesn't only confer high levels of TMP resistance, but that the accumulation of mutations does not compromise enzymatic efficiency. Crystal structures of this enzyme bound to a first generation PLA showed that the loss of a water mediated hydrogen bond between His30 and Thr111 is responsible for the loss of TMP efficacy[7]. Compounding this observation with previously understood effects of the Phe98 mutation on NADPH and inhibitor binding allows for a complete understanding of mutational resistance and allows for the development of more robust inhibitors.

In vitro generation of resistance is achieved by extended exposure of large concentrations (10^{11} to 10^{12} CFU/mL) of bacterial culture to high concentrations (6x MIC) of inhibitor. Upon exposure to inhibitor, the resistant bacteria are revealed and can grow unharmed under the antibiotic pressure. It is unclear whether these revealed mutant strains are generated directly in response to antibiotic pressure from a stress response or if these resistant bacteria pre-exist in small quantities and are revealed upon the death of the susceptible population. The first report of the prospective analysis of mutational resistance to early generation PLAs in *S. aureus* yielded the selection of F98Y, F98I and H30N single mutants at a very low (10^{-10}) mutational frequency. It was also observed that the series of PLAs exhibited superior potency over TMP against these enzymes and showed lower mutation prevention concentrations (MPCs). This indicates that the class of

antifolates can compensate for the resistance effect of the mutations, are potentially less susceptible to mutational resistance and are promising candidates to overcome clinical resistances.

4.2 Generation and characterization of UCP1006^{R} MRSA strains

To further characterize the resistance profile of the propargyl-linked antifolates, strains containing point mutations in the *dfrB*, generated by extended UCP1006 exposure, were selected and analyzed by microbiological, biochemical and structural mechanisms. For single-step mutant selection, the ATCC quality control strain 43300 was subjected to UCP1006 at 6x MIC yielded three clinically observed mutations: F98Y, H30N and H149R as well as three novel mutations: F151S, F151C and D142Y. A second round of resistance selection using UCP1006 and progenitor strains possessing F98Y or H149R yielded a series of both novel and clinically relevant double mutants (Table 1). As strains containing H30N/F98Y and F98Y/H149R mutants have been isolated clinically after exposure to TMP[1], we chose to fully characterize the fitness of these mutant enzymes and bacteria, including their single mutant (F98Y, H30N, H149R) counterparts (Table 1) at a biochemical, structural and cellular level.

Table 1 Mutant Strain Selection using UCP1006

Mutant	Progenitor Strain	Single Nucleotide Polymorphism	Seq. Frequency (%)	Overall Freq	Doubling time (min)
F98Y	WT	TTT to TAT	2/19 (10.5)	$3.11x10^{-11}$	34.53
H149R	WT	CAT to CGT	7/19 (36)	$1.07x10^{-10}$	38.34
H30N	WT	CAT to AAT	3/19 (15.8)	$4.68x10^{-11}$	36.62
F151S	WT	TTT to TCT	3/19 (15.8)	$4.68x10^{-11}$	ND
F151C	WT	TTT to TGT	2/19 (10.5)	$3.11x10^{-11}$	ND
D142Y	WT	CAT to TAT	1/19 (5.3)	$1.57x10^{-11}$	ND
H30N/V70L	WT	GTA to TTA	1/19 (5.3)	$1.57x10^{-11}$	ND
F98Y, H149R	H149R	TAT to TTT	1/1 (100)	$1.23x10^{-11}$	30.89
H30N, F98Y	F98Y	CAT to CGT	2/16 (12.5)	$8.20x10^{-12}$	35.06
F98Y, F151S	F98Y	TTT to TCT	1/16 (6.25)	$4.10x10^{-12}$	ND
F98Y, F151C	F98Y	TTT to TGT	1/16 (6.25)	$4.10x10^{-12}$	ND
V31G, F98Y	F98Y	GTT to GGT	6/16 (37.5)	$2.46x10^{-11}$	ND
V31L, F98Y	F98Y	GTT to CTT	5/16 (31.3)	$2.05x10^{-11}$	25.4
V31G, F98Y, V112D	F98Y	(V31G) GTT to GGT (V112D) GTT to GAT	1/16 (6.25)	$4.10x10^{-12}$	ND

Overall mutation frequencies for each strain exposed to UCP1006 were calculated based on the inoculum and average number of colonies appearing on the 6x MIC experimental plates. Resistance to UCP1006 with *S. aureus* is generated at a very low frequency of 2.96×10^{-10}. Overall mutation frequencies are even lower to progenitor strains possessing F98Y and H149R, with rates of 6.56×10^{-11} and 3.75×10^{-11}, respectively. Specific mutational frequencies were then calculated based on the number of sequenced colonies with a particular mutation. If the generation of double mutants occurs in a step-wise fashion, the combined frequency of resistance could be as low as 10^{-21}. Evaluation of

bacterial fitness, measured by doubling time, shows that the majority of the mutant strains exhibit only minor losses in growth time (1.08-1.2 x doubling time of wild-type), with the exception of Sa(F98Y/H149R), which preserved or slightly improved doubling time (Table 1). Overall, these studies show that the accumulation of the mutations retains cellular fitness of the strains.

4.3 Generation and Evaluation of UCP1006^R Enzymes

The recombinant mutant DHFR enzymes were created by site-directed mutagenesis of the wild-type enzyme and purified using affinity chromatography. Michaelis-Menten kinetics were measured for each enzyme using 12.5-100 μM NADPH and 12.5-100 μM DHF (Table 2)[9]. Overall, the enzymes, with the exception of Sa(H149R), have k_{cat}/K_M values within approximately 2-fold of the wild-type value. Sa(H149R) has a significantly reduced k_{cat}/K_M value (6-fold reduction), which is a consequence of higher K_M values for both DHF and NADPH. Interestingly, the double mutant Sa(F98Y/H149R) compensates for the low efficiency of the single Sa(H149R) mutant as the Sa(F98Y/H149R) enzyme restores the K_M value for DHF and NADPH to nearly wild-type values. Similarly, the single H30N mutation suffers a significant decrease in NADPH K_M (31.21 to 79.89 μM); this K_M value is restored to a value near wild-type in the double Sa(H30N/F98Y) mutant. This compensatory relationship was observed in the analysis of F98Y, V31L enzymes generated after the K* prediction, however here, the single mutants are also fit[9].

Table 2 Mutant Enzyme Characterization

	K_M (DHF) (μM)	V_{max} (DHF)	K_M (NADPH) (μM)	k_{cat} DHF (s^{-1})	k_{cat}/K_M DHF
WT	17.5	62.93	31.21	41.13	2.4
F98Y	8.38	68.38	57.08	44.76	5.3
H30N	24.49	45.76	79.89	29.91	1.2
H30N, F98Y	11.24	39.98	51.17	26.1	2.3
H149R	63.54	42.44	303.4	27.74	0.4
F98Y, H149R	5.24	44.98	45.08	29.40	5.6

4.4 Propargyl-linked Antifolates Overcome Mutational Resistance

Understanding mutational resistance to UCP1006 is critical for guiding the development of a newer generation of robust PLAs that overcome the effects of the point mutations. By examining previously identified structure-activity relationships[6, 8, 10] and testing several compounds likely to inhibit the single mutant enzymes, we initially identified a series of pyridine lead compounds, UCP1006, UCP1038, UCP1039 and UCP1040, with potent MICs against the single mutant strains and enzymes. The incorporation of the knowledge that enantio-specific methyl substitutions at the propargyl position can steer the biaryl system and result in a further optimized interaction with the enzyme led to the evaluation of UCP1062, UCP1063 and UCP1099[12]. These enatio-pure PLAs further increased the activity against single mutant strains and enzymes and showed the first hints of activity against the double mutant strains. Finally, incorporation of the carboxylate C-ring substitution on ring to the initial set of promising compounds lead to a series of compounds potent enzymatic and cellular activity across all single and double mutant species[11] (Figure 1, Tables 3 and 4).

All of the compounds exhibit good potency (K_i values less than 16 nM, against the single mutant enzymes Sa (F98Y) and Sa(H30N) with only minor losses relative to wild-type (Table 4). UCP1038 lost the greatest affinity for the Sa(H30N) enzyme with a 12.6-fold loss. Activity against the single mutant Sa(H149R) was more compromised, where TMP loses activity against the Sa(H149R) mutant by 69-fold. The PLAs possess a range of affinity for this enzyme, ranging from UCP1173 with a K_i value of 153 nM to UCP1038 with a K_i value of 1362 nM. UCP1039 with unconstrained 3' and 4' methoxy groups maintained reasonable affinity with a K_i of119 nM when compared to compound UCP1038, showing that flexibility, in addition to the propargylic subsitutions, may be critical for affinity to the mutant enzymes. In general, the dioxalane compounds (UCP1038 and UCP1099) as well as compounds UCP1040, 1062 and 1063 lose significant affinity for the Sa (F98Y, H30N) double mutant enzyme (180 to 300-fold loss), TMP losses 130-fold loss of activity against this enzyme. Inhibition of Sa (F98Y, H149R) remains a struggle for the pyridine substituted PLA series.

The PLA-COOH class of compounds was designed to form ionic interactions with a conserved arginine to provide compensatory interactions in these mutant enzymes. These COOH substituted compounds, with the exception of UCP1106, show much greater affinity for the double mutant Sa (F98Y, H30N) enzyme with K_i values ranging from 19-45 nM. With K_i values of 107-2059 nM against the double mutant Sa (F98Y, H149R) enzyme pyridine compounds as well as UCP1106 and TMP maintain challenge. However, UCP1172 and UCP1173 show significant inhibition for this enzyme, with K_i values of 69 and 55 nM, respectively. Again, it appears that the presence of the ionized carboxylates may provide critical additional interactions to compensate for reduced contacts elsewhere in the complex.

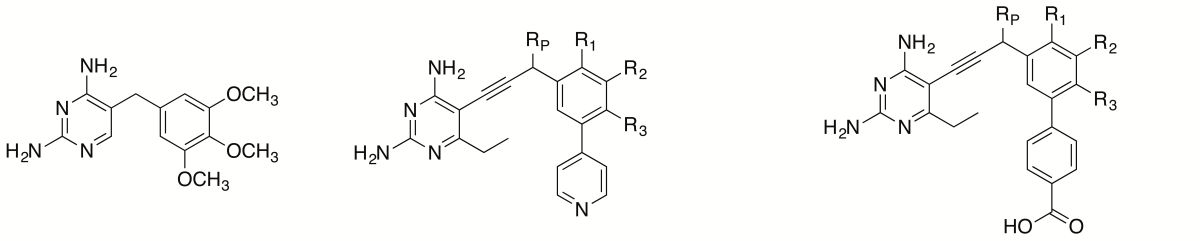

Trimethoprim

Pyridine Scaffold

UCP1006: R_P=CH_3, R_1=H, R_2=OCH_3, R_3=H
UCP1038: R_P=CH_3, R_1=H, R_2, R_3=dioxolane
UCP1039: R_P=H, R_1=H, R_2=OCH_3, R_3=OCH_3
UCP1040: R_P=CH_3, R_1=OCH_3, R_2=H, R_3=H
UCP1062: R_P=R-CH_3, R_1=H, R_2=OCH_3, R_3=H
UCP1063: R_P=R-CH_3, R_1=OCH_3, R_2=H, R_3=H
UCP1099: R_P=R-CH_3, R_1=H, R_2, R_3=dioxolane

PLA COOH Scaffold

UCP1106: R_P=H, R_1=OCH_3, R_2=H, R_3=H
UCP1164: R_P=S-CH_3, R_1=OCH_3, R_2=H, R_3=H
UCP1175: R_P=H, R_1=H, R_2=OCH_3, R_3=H
UCP1172: R_P=R-CH_3, R_1=H, R_2=OCH_3, R_3=H
UCP1173: R_P=S-CH_3, R_1=H, R_2=OCH_3, R_3=H

Figure 1. Structure of Trimethoprim and PLAs

Table 3 K_i (nM) of PLAs against WT and mutant enzymes

Compound	Sa(WT)	Sa(F98Y)	Sa(H30N)	Sa(H149R)	Sa(H30N, F98Y)	Sa(F98Y, H149R)
TMP	3.4±0.3	14.68±0.08	6.9±0.2	240±10	595±5	1729±40
UCP1006	2.8±0.3	13.1±0.7	12.9±1	681±27	191±10	2059±200
UCP1038	2.5±0.1	3.0±0.4	33.2±1	1363±38	485±40	779±25
UCP1039	2.1±0.1	12.1±0.6	4.5±0.4	119±7	449±40	107±9
UCP1040	4.51±0.09	19.7±1	5.9±0.9	1563±34	820±80	878±30
UCP1062	2.6±0.3	8.6±0.4	16.7±0.6	1154±19	801±51	894±84
UCP1063	1.6±0.1	16.7±1	16.5±1	269±20	417±30	422±14
UCP1099	5.2±0.3	13.6±0.8	8.9±0.6	174±4	345±10	289±20
UCP1106	4.8±0.1	11.7±0.5	3.9±0.4	130±3	158±4	142±2
UCP1164	5.5±0.1	11.8±0.7	3.8±0.6	862±39	36±3	295±9
UCP1175	1.64±0.09	11.3±0.7	3.36±0.06	323±23	45±3	184±5
UCP1172	1.3±0.1	7.9±0.2	3.5±0.6	111±7	19±1	69±2
UCP1173	2.1±0.1	5.57±0.08	3.3±0.2	153±11	16.6±0.3	55±1

The compounds were also tested for inhibition of the growth of wild-type and mutant (Sa(F98Y), Sa(H30N), Sa(H149R), Sa(H30N, F98Y) and Sa(F98Y/H149R)) strains of *S. aureus* (Table 3). The antibacterial activity of TMP was clearly crippled by even the single mutations and reached a 50-100 μg/mL MIC value against the double mutant strains. The pyridine PLAs as well as UCP1106 and UCP1164 were more potent against the wild-type strain than TMP and many were more potent against the single mutants (MIC values between 0.078 and 5 μg/mL). However, these compounds also suffered significant losses against the strains with double mutations in DHFR. PLAs UCP1172, 1173 and 1175 have superior activity against the wild-type strain as well as strains with both single and double mutants. Notably, the MIC value for UCP1173 against either of the double mutant strains is only 4-fold higher than the MIC value of TMP for wild-type *S. aureus*. On-target activity of the PLAs was verified end-product rescue MICs, in which the folic acid cycle is bypassed by the increased concentration thymidine concentration in the growth media (Thy^+)[11,12]. All compounds, with the exception of UCP1038, UCP1062 UCP1063 and UCP1099 have Thy^+ MICs of >40 μg/mL, where UCP1038, UCP1062 and UCP1063 have Thy^+ MICs of 5 μg/mL and UCP1099 had an MIC of 10 μg/mL. These MIC values rise by 64x – 4081x, validating that the compounds inhibit DHFR.

Table 4 Minimum Inhibitory Concentrations (μg/mL)

Compound	ATCC 43300	Sa(F98Y)	Sa(H30N)	Sa(H149R)	Sa(H30N, F98Y)	Sa(F98Y, H149R)
TMP	0.3125	10	2.5	2.5	50	100
UCP1006	0.0781	2.5	2.5	2.5	20	80
UCP1038	0.0781	1.25	5	5	40	40
UCP1039	0.0195	0.625	0.625	0.625	20	40
UCP1040	0.625	2.5	2.5	2.5	20	40
UCP1062	0.0391	0.625	0.625	0.625	40	20
UCP1063	0.0195	1.25	0.625	1.25	10	20
UCP1099	0.0195	1.25	2.5	2.5	20	20
UCP1106	0.0195	0.1563	0.1563	0.1564	6.25	>50
UCP1164	0.0391	0.1563	0.1563	0.0781	>40	>40
UCP1175	0.0195	0.1563	0.1563	0. 1563	5	10
UCP1172	0.0098	0.0781	0.0781	0.0391	1.25	2.5
UCP1173	0.0098	0.0781	0.0781	0.0781	1.25	1.25

4.5 Structural Analysis of Mutant Enzymes and UCP1106

A series of crystal structures with the wild-type and mutant enzymes elucidates the structural changes caused by the selected mutations. Mutants Sa (F98Y), Sa (H30N) and Sa (H30N, F98Y) DHFR were co-crystallized with NADPH and UCP1106; the structure of the wild type Sa DHFR complex with NADPH and UCP1106 has been previously described (PDB: 5HF0; Figure 1)[11]. The structures of the wild-type and Sa (H30N) enzymes feature mixed occupancy of tricyclic- and β-NADPH in the cofactor binding site (Figure 2), similar to previous observations[6, 10].

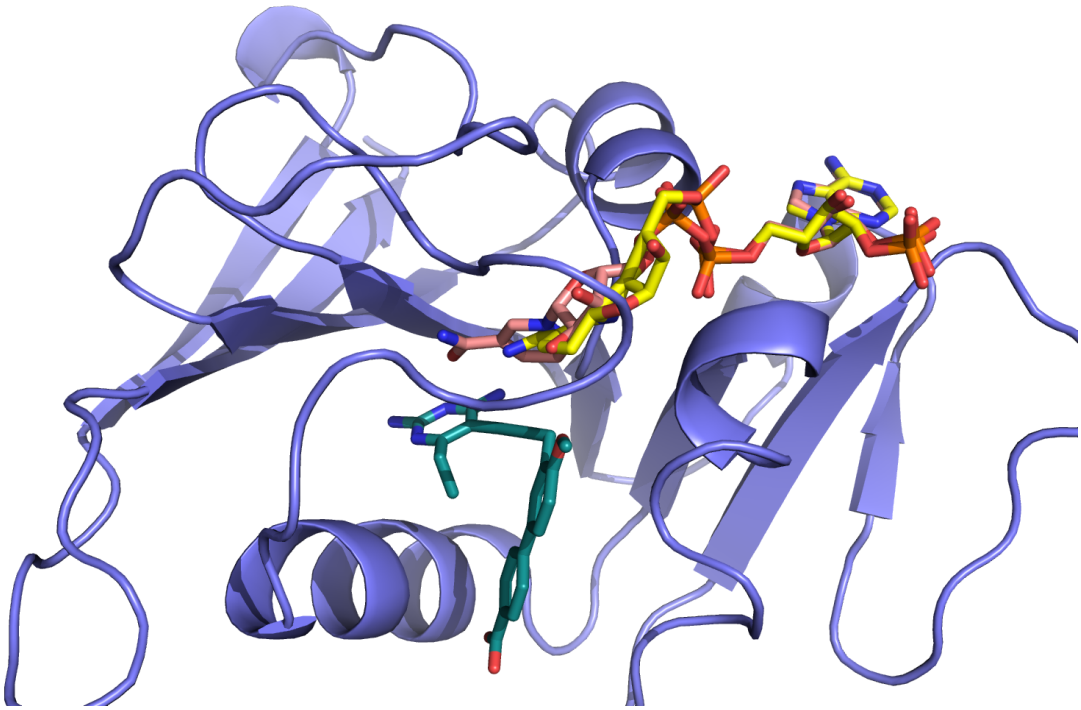

Figure 2 View of wild-type SaDHFR (purple) bound to β-NADPH (salmon), α-NADPH (yellow) and UCP1106 (green).

The structural basis of antifolate resistance in these F98Y mutant enzymes appears to involve the loss of a critical hydrogen bond between the carbonyl backbone of Phe 92 and the conserved 4-amino group of the inhibitor. Comparisons between structures of wild-type SaDHFR and those with the F98Y mutant enzymes show that the F98Y mutation induces a rotation of the Phe 92 backbone carbonyl by 1.1 Å, which disrupts the hydrogen bond between the carbonyl oxygen and the N_4-amino group of the diaminopyrimidine ring (Figure 3). The hydrogen bond between the Phe 92 carbonyl and the 4-amino group in the wild-type enzyme is 2.9 Å; in the mutated structure it is 3.9 Å. There is a new hydrogen bond between Tyr 98 and the 4-amino group, but with reduced strength (3.4 Å). Loss of this conserved hydrogen bond to Phe 92 would represent a significant loss in affinity.

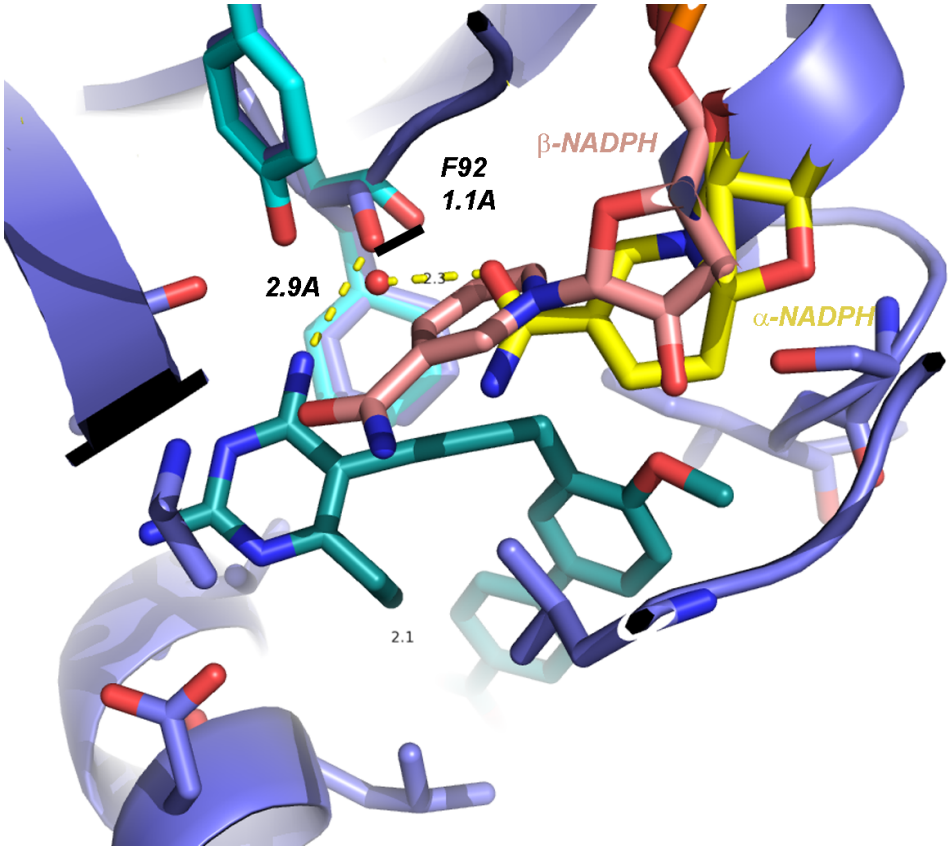

Figure 3 The shift in the position of the carbonyl of Phe 92 in the F98Y mutant (cyan) eliminates a hydrogen bond to the 4-amino group of the inhibitor. The black bar represents the 1.1 Å shift. The water molecule bound to the nicotinamide ring of α-NADPH and Phe 92 is shown.

The presence of the Asn 30 mutation results in the re-organization of a water network between the active site residues and the inhibitor, effectively eliminating a hydrogen bond between the pyrimidine ring and protein. In the structure with wild-type SaDHFR, a critical water molecule bound to the N_2-amino group of the diaminopyrimidine (2.9 Å; cyan in Figure 1c) is involved in a water network with the backbone carbonyl of Tyr 109 (2.8 Å) and the imidazole side chain of His 30, effectively tying the diaminopyrimidine to two protein residues (Figure 4). In fact, the distance of this water molecule bound to His 30 is quite conserved, having an average value of 2.9 Å over several SaDHFR:PLA crystal structures. In the structures with the Asn 30 mutation, the water molecule (magenta in

Figure 4) more closely coordinates with the mutated Asn residue instead of the inhibitor, reducing the effective hydrogen bonding interactions of the inhibitor. Measurements of the distance of the water molecule to the 2-amino group show that the bonds are 3.4 Å and 3.5 Å in the SaH30N and Sa(F98Y/H30N) structures, respectively; these distances are too far to create effective hydrogen bonds. This disruption of the water network linking the inhibitor to the active site residues is similar to that reported in our earlier structure[7].

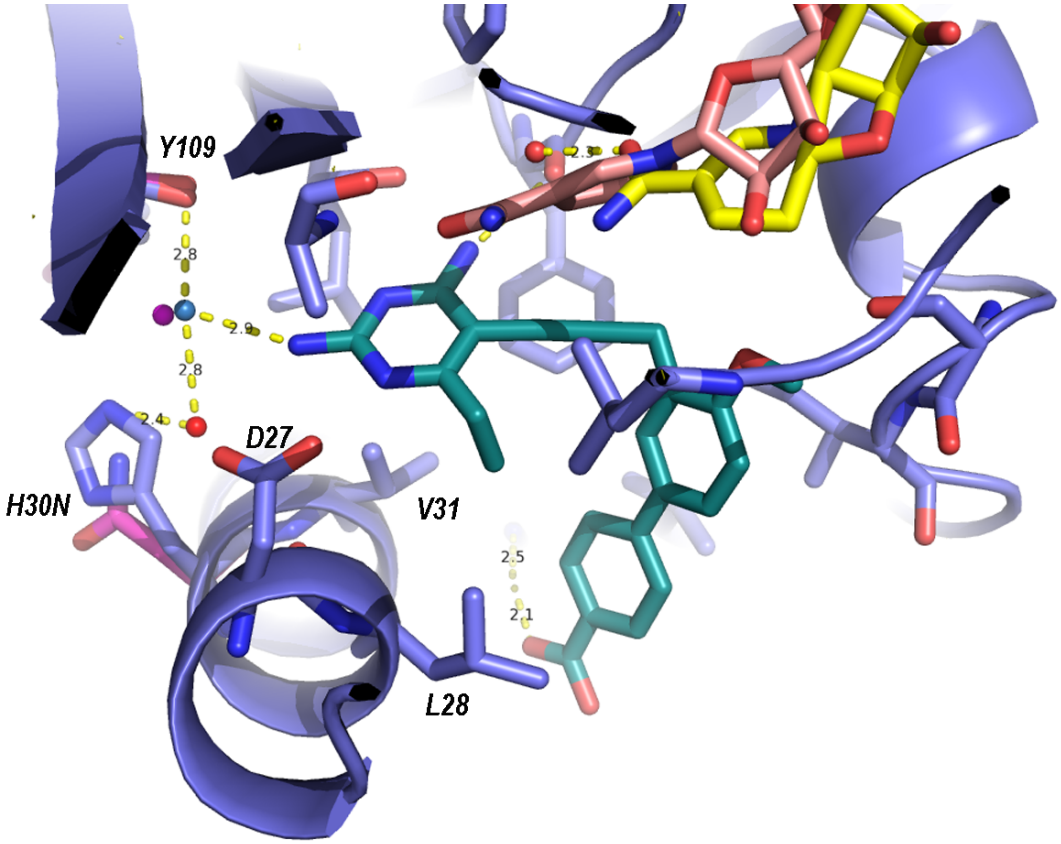

Figure 4 Two water molecules (blue and red) tie the pyrimidine ring to His 30 (wt) and Tyr 109. The H30N mutation (magenta) pulls one of the water molecules (magenta) 1 Å away from the 2-amino group, eliminating the hydrogen bond.

The double mutant enzyme, F98Y/H30N shows both the shifted carbonyl for Phe 92 as well as the altered water network at Asn 30, greatly decreasing the hydrogen bonding interactions of the 2- and 4-amino groups of the pyrimidine ring. There is a prominent

functional synergy between these two mutations. Not only does the second mutation further weaken inhibitor binding by disrupting contacts at the pyrimidine ring, but also restores the catalytic activity of the enzyme to near wild-type values (Table 2). The two cooperative effects provide a powerful mechanism for the organism to become drug resistant.

In general, the PLAs show significantly increased potency for the mutant enzymes relative to TMP. One reason for this increased potency is the coordination of a water molecule, observed in both the F98Y and F98Y/H30N structures, between the carboxylate group on UCP1106 and Arg 57 (2.5 Å) (Figure 5). The extra hydrogen bonds created by the coordinated water molecule and Arg 57 compensate for interactions lost by the pyrimidine ring. The presence of the tricyclic a-NADPH anomer indicates a potentical beneficial relationship between PLA activity and novel anomer. The displaced nicotinamide of tNADPH coordinates a water molecule (2.4 Å) that stabilizes the carbonyl of Phe 92 (3 Å), preserving the hydrogen bonding interactions between Phe 92 and the inhibitor (Figure 3). β-NADPH does not coordinate this water molecule, does not stabilize the Phe 92 carbonyl and effectively allows the loss of the hydrogen bond.

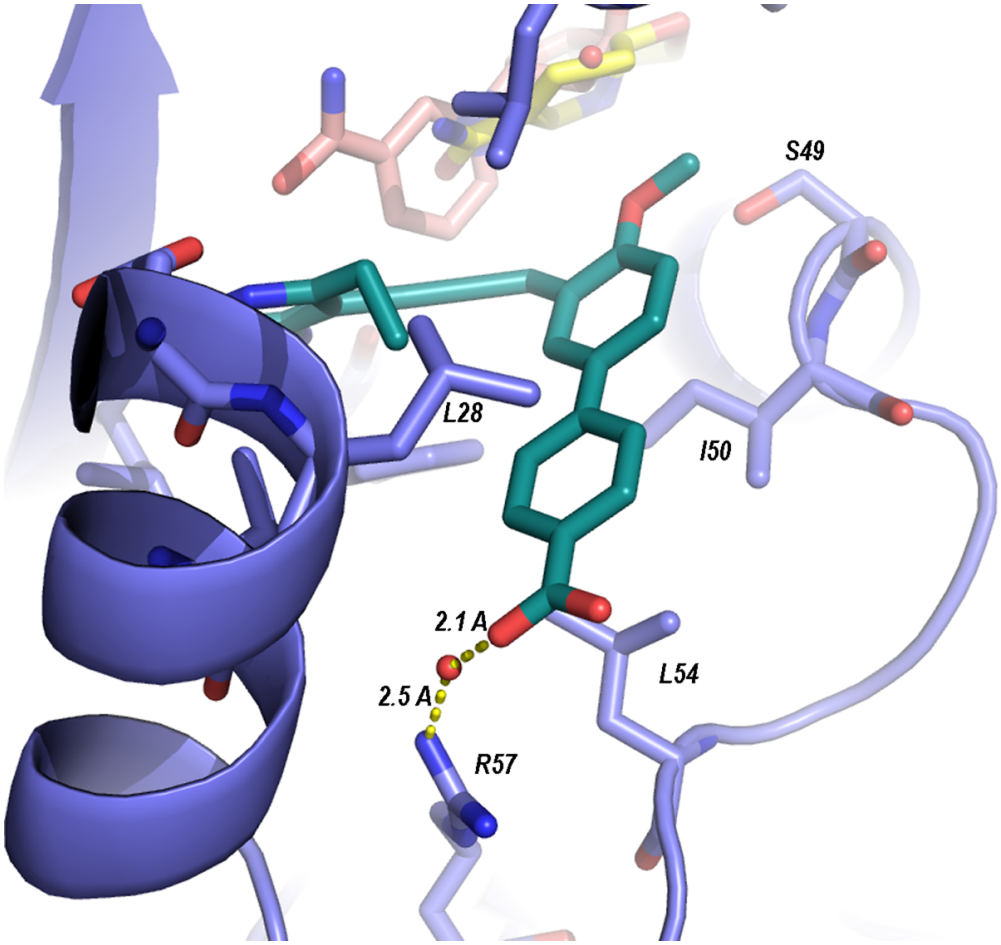

Figure 5 A water molecule forms hydrogen bonds between the carboxylate and Arg 57

4.6 Conclusions

Through generation, selection and analysis of UCP1006^{R} *S. aureus* mutants, the biochemical and molecular mechanisms of resistance via point mutations can be evaluated. By focusing on a panel of strains containing *dfrB* mutations that have clinically identified as TMP resistance determinants, discovery efforts can be focused on overcoming modifications that the enzyme has known to accommodate with minimal fitness losses. Overall, the mutation frequency for the PLAs is very low with frequencies between 10^{-10} and 10^{-11}. A series of fitness experiments show that the mutant enzymes and strains, especially double mutants, are as fit as wild-type. Evaluation of TMP and a

series of twelve PLAs shows that the PLAs are generally much more potent than TMP against both the mutant enzymes and strains. Specifically, the PLAs possessing a carboxylate moiety exhibited good potency against the difficult double mutant enzymes and strains.

Crystal structures of UCP1106 bound to NADPH and SaDHFR, Sa (F98Y), Sa (H30N) and Sa (F98Y/H30N) show that the mutations specifically diminish the binding of the 2- and 4-amino groups on the pyrimidine ring through nuanced changes in the water networks. The carboxylate moiety forms hydrogen bonds, water mediated in the case of UCP1106, with an active site arginine, compensating for some of the lost pyrimidine interactions and restoring affinity to the mutant enzymes. Overall, the PLA-COOH compounds appear to be excellent lead compounds that maintain potency for wild-type enzymes and strains while overcoming resistance features in mutant enzymes and strains, further indicating that optimization of this class of compounds can overcome future enzymatic modifications.

4.7 Acknowledgements

I would like to acknowledge Eric Scocchera, Dr. Naren G-Dayanadan and Dr. Santosh Keshipeddy for the synthesis of the PLA compounds presented here. I would also like to thank Jacob Ferreira for his assistance in preforming the enzymatic assays and growth of the crystals. Data collection for the crystal structures was preformed remotely at Stanford Synchrotron Radiation Lightsource (SSRL) with assistance from Clyde Smith.

4.8 References

1. Vickers, A.; Potter, N.; Fishwick, C.; Chopra, I.; O'Neill. A. Analysis of mutational resistance to trimethoprim in *Staphylococcus aureus* by genetic and structural modelling techniques. *J. Antimicrob. Chemother.* **2009***, 63*, 1112-1117.

2. Hampele, I. C., D'Arcy, A., Dale, G. E., Kostrewa, D., Nielsen, J., Oefner, C., Page, M. G., Schönfeld, H. J., Stüber, D., and Then, R. L. Structure and function of the dihydropteroate synthase from Staphylococcus aureus. *J. Mol. Biol.* **1997,** *268*, 21–30.

3. Schmitz, F.; Jones, M.; Hofmann, B.; Hansen, B.; Scheuring, S.; Luckefahr, M.; Fluit, A.; Verhoef, J.; Hadding, U.; Heinz, H.; Kohrer, K. Characterization of *grlA, grlB, gyrA* and *gyrB* Mutations in 116 Unrelated Isolates of *Staphylococcus aureus* and Effects of Mutations on Ciprofloxacin. *Antimicrob. Agents Chemother.* **1998,** *42*, 1249-1252.

4. Dale, G.; Broger, C.; D'Arcy, A.; Hartman, P.; DeHoogt, R.; Jolidon, S.; Kompis, I.; Labhardt, A.; Langen, H.; Locher, H.; Page, M.; Stuber, D.; Then, R.; Wipf, B.; Oefner, C., A single amino acid substitution in *Staphylococcus aureus* dihydrofolate reductase determines trimethoprim resistance. *J. Mol. Biol.* **1997**, *266*, 23-30.

5. Heaslet, H.; Harris, M.; Fahnoe, K.; Sarver, R.; Putz, H.; Chang, J.; Subramanyam, C.; Barreiro, G.; Miller, J. R., Structural comparison of chromosomal and exogenous dihydrofolate reductase from *Staphylococcus aureus* in complex with the potent inhibitor trimethoprim. *Proteins* **2009**, *76*, 706-717.

6. Frey, K.; Liu, J.; Lombardo, M.; Bolstad, D.; Wright, D.; Anderson, A., Crystal structures of wild-type and mutant methicillin-resistant *Staphylococcus aureus* dihydrofolate reductase reveal an alternative conformation of NADPH that may be linked to trimethoprim resistance. *J. Mol. Biol.* **2009**, *387*, 1298-1308.

7. Frey, K.; Lombardo, M.; Wright, D.; Anderson, A., Towards the understanding of resistance mechanisms in clinically isolated trimethoprim-resistant, methicillin-resistant *Staphylococcus aureus* dihydrofolate reductase. *J. Struc. Biol.* **2010**, *170*, 93-97.

8. Frey, K.; Viswanathan, K.; Wright, D.; Anderson, A., Prospectively screening novel antibacterial inhibitors of dihydrofolate reductase for mutational resistance. *Antimicrob. Agents and Chemother.* **2012**, *56*, 3556-3562.

9. Reeve, S.; Gainza, P.; Frey, K.; Georgiev, I.; Donald, B.; and Anderson, A., Protein design algorithms predict viable resistance to an experimental antifolate. Pr*oc. Natl. Acad. Sci. U. S. A.* **2014,** *112*, 749-754.

10. Keshipeddy, S.; Reeve, S.; Anderson, A.; Wright, D., Nonracemic antifolates stereoselectively recruit alternate cofactors and overcome resistance in *S. aureus*. *J. Am. Chem. Soc.* **2015**, *137*, 8983-8990.

11. Scocchera, E.; Reeve, S.; Keshipeddy, S.; Lombardo, M.; Hajian, B.; Sochia, A.; Alverson, J.; Priestley, N.; Anderson, A.; Wright, D. Charged non-classical antifolates with activity against gram-positive and gram-negative pathogens. *ACS Med. Chem. Lett.* **2016**, *7*, 692-696.

12. Molina, F.; Jimenez-Sanchez, A.; Guzman, E., Determing the optimal thymidine concentrations for growing Thy- *Escherichia coli* strains. *J. Bacteriol.* **1988**, *180*, 2992-2995.

Chapter 5

Understanding and Overcoming Clinical Trimethoprim Resistance

5.1 Clinical Trimethoprim/Sulfamethoxazole Resistance

Resistance to trimethoprim began developing over a decade after its introduction to the clinic in 1962[1,2]. A single TMP^R *S. aureus* strain from Switzerland revealed the first clinical TMP^R determinant, an innately resistant plasmid-acquired DHFR enzyme. The gene, *dfrA*, located on a mobile genetic element, encodes a highly resistant DHFR enzyme commonly referred to as S1 DHFR (here referred to as DfrA). DfrA is believed to originate from *Staphylococcus epidermidis,* as it contains three mutations: V31L, G43A and F98Y when compared to its TMP^S endogenous DHFR[2]. DfrA and DfrB share an 80% sequence similarity. In 1997, point mutations in the endogenous DHFR (DfrB), (including F98Y as well as H30N, F98Y and F98Y, H149R), discussed extensively in Chapter 5 were identified as clinical TMP^R determinants[3].

More recently, two additional TMP^R *dfr* isoforms were identified in *S. aureus* clinical isolates. The first gene, *dfrG*, encoding an innately resistant DHFR enzyme (DfrG), was initially identified in Thailand[4] followed by reports of its wide spread throughout sub-Sahara Africa[5]. This latter study monitored the import of the gene to Europe through people traveling from Africa. Finally, DfrK, encoded by the gene *dfrK*, were detected in farmers and children living near rural, highly agricultural regions in Ireland[6]. DfrK, which shares a 90% sequence identity with DfrG, had been widely reported in pathogenic strains of porcine and livestock *S. aureus*, prior to its identification in human pathogens[7,8]. DfrG and DfrK only share a 38% sequence identity to DfrA and 40% to DfrB. Like *dfrA*, *dfrK* and *dfrG* are located on highly mobile genetic elements and incorporated into the

chromosomes via horizontal gene transfer. Despite knowledge of the existence of the plasmid-encoded resistance elements *dfrG* and *dfrK*, their importance in clinical strains of MRSA and MSS Awas not thought to be significant. Therfore, antifolate development was more targeted toward the accumulation of resistant mutants of the chromosomal gene.

Recent surveillance reports indicate a regional variance in resistance rates for TMP, whereas US hospitals report rates of 2-3% for TMP/SMX[9], European travel clinics report rates of up to 50% for TMP and 19% for TMP/SMX[5]. There has be no recent survey of the molecular mechanism of resistance to TMP or TMP/SMX in United States hospitals. Until this point, we have been pursuing the design of inhibitors that overcome mutational resistance with the intentions of creating broad activity against current, clinically relevant TMP^R strains. Initial success of the class of carboxylate PLAs against series the TMP^R mutant enzymes and strains, specifically ones containing F98Y, validates these design efforts. As antibiotic resistance is constantly evolving, it is crucial to identify the contemporary mechanisms of resistance in order to further develop potent lead compounds. Presented in this chapter is the investigation into the molecular mechanisms of TMP resistance in *S. aureus* isolates from Connecticut hospitals and efforts to identify inhibitors that directly inhibit the predominating mechanisms of resistance.

5.2 Characterization of TMP^R Clinical Isolates

Over a two-year period, more than 30 TMP^R *S. aureus* isolates were obtained from the clinical microbiology laboratories at UConn Health/John Dempsey Hospital (UCH) and Hartford Hospital (HH). These strains were isolated in the course of routine clinical care and originally submitted for routine susceptibility testing. The strains were collected from different patients, were isolated from a variety of sources including blood, skin and soft

tissue (SSTI), sputum (lung) and the sinus cavity and feature diverse antibiotic resistance genotypes. The blood sample was derived from a hospitalized patient; the other isolates were outpatient derived. TMP/SMX resistance rates at UCH and HH are reported at $\leq$1 % and 2% for MSSA and 2-3% and 5% for MRSA isolates, respectively.

The first obtained clinical isolates, UCH MRSA 1-10, revealed high levels (MIC > 1mg/mL) of TMP resistance (Table 1). Initial investigations into the TMP^R mechanisms indicated that all strains contained a WT, TMP^S endogenous DHFR (*dfrB*) and the lack of the well-characterized *dfrA* gene was confirmed by PCR. In order to explore further, we initially conducted whole genome sequencing on a single strain, UCH MRSA 1. Genomic analysis revealed the presence of a second, chromosomally incorporated DHFR enzyme encoded by the gene, *dfrG* that had been integrated into the chromosome. To our knowledge, this is the first report of *dfrG* in North America. We then used PCR to evaluate the remaining strains for their *dfrB* sequences and the presence of *dfrG* as well as two other plasmid-encoded genes, *dfrA* and *dfrK*, known to occur in *S. aureus*[2,6,11]. Surprisingly, we found that all of the clinical isolates carried one of the plasmid-encoded genes, with *dfrG* predominating in 78% of strains. We also identified, for the first time in the United States, the presence of the *dfrK* gene. *dfrA* appeared in the remaining strains. Given the limited number of strains and hospitals represented here, the occurrence of these diverse, previously unreported resistance elements are striking.

Table 1 Characterization of All TMP^R Clinical MRSA Isolates

Strain	*Source*	*dfrB*	TMP^R element	Strain	*Source*	*dfrB*	TMP^R element
UCH 1	Blood	WT	*dfrG*	UCH124	Urine	WT	*dfrG*
UCH 2	Sputum	WT	*dfrG*	UCH 126	Wound	WT	*dfrG*
UCH 5	Sputum	WT	*dfrG*	UCH127	SSTI	WT	*dfrG**
UCH 6	Urine	WT	*dfrG*	UCH128	SSTI	WT	*dfrG*
UCH 7	Sputum	WT	*dfrG*	UCH129	Wound	WT	*dfrG*
UCH 8	Sputum	WT	*dfrG*	UCH130	SSTI	WT	*dfrG*
UCH 9	Feces	WT	*dfrG*	UCH131	Urine	WT	*dfrG*
UCH 10	Sputum	WT	*dfrG*	UCH132	Blood	WT	*dfrG*
UCH115	SSTI	WT	*dfrA*	HH553	Sputum	WT	*dfrA*
UCH116	SSTI	WT	*dfrA*	HH601	Blood	WT	*dfrG*
UCH117	Urine	WT	*dfrG*	HH714	SSTI	WT	*dfrG*
UCH118	SSTI	WT	*dfrA*	HH1144	SSTI	WT	*dfrA*
UCH119	SSTI	WT	*dfrG*	HH1155	Sputum	WT	*dfrG*
UCH120	Trachea	WT	*dfrG*	HH1184	Sputum	WT	*dfrK*
UCH121	Sputum	WT	*dfrG*	HH1251	SSTI	WT	*dfrA*
UCH123	Wound	WT	*dfrG*	MSSA 1	Sinus	WT	*dfrG*

* Strain is SMX^S, which presents as $Bactrim^S$ clinically

A panel of eight strains, based on their antibiotic phenotypes, was selected for a more in-depth microbiological, biochemical and genetic analysis. Seven of the selected strains were classified as MRSA and one additional was MSSA; the methicillin resistance classifications were based on clinically determined susceptibilities. All three of the innately resistant DHFRs are represented in the panel of isolates (Table 2, Figure 1). The fitness of the strains, as measured by doubling time, doesn't appear to be any affected by harboring these extra genes as the doubling times were generally shorter than the ATCC 43300 strain (Table 2).

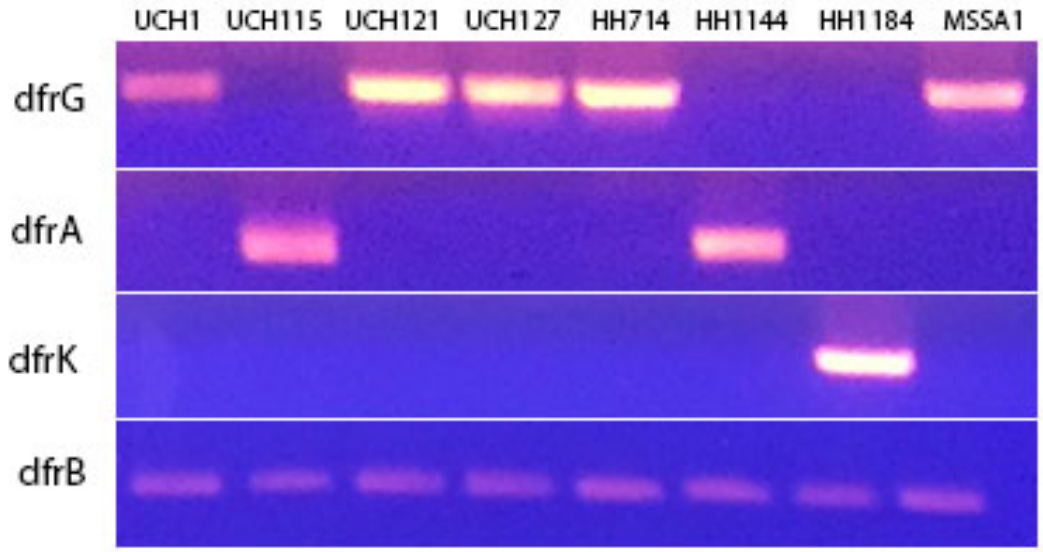

Figure 1 Composite gel showing PCR products depicting the presence of *dfrG*, *dfrA*, *dfrK* and *dfrB* in the UCH and HH strains.

While each of the strains is highly resistant to TMP, they have variable susceptibilities SMX, with MIC values between 250 and >1,000 μg/mL or 15-500 μg/mL, respectively. UCH MRSA 127, which contains *dfrG* but is SMX susceptible presents clinically as Bactrim^{S} with the MIC at the clinical breakpoint. This point can convolute the surveillance TMP^{R} statistics in clinical labs that only screen for Bactrim resistance. In addition to TMP and SMX, strains show varying resistance profiles to a wide range of commonly used antibiotics including erythromycin, fluoroquinolones, aminoglycosides and tetracycline (Table 3).

Table 2 Characterization of Select TMP^R Clinical Isolates

Strain Designation	Infection Source	TMP Resistant Gene	*dfrB*	TMP MIC (μg/mL)	SMX MIC (μg/mL)	Doubling Time (min)
UCH 1	Blood	*dfrG*	WT	>1,000	>500	40.33
UCH 115	SSTI	*dfrA*	WT	250	500	35.19
UCH 121	Sputum	*dfrG*	WT	>1,000	>500	28.17
UCH 127	SSTI	*dfrG*	WT	>1000	15.625	38.61
HH 714	SSTI	*dfrG*	WT	>1000	>500	27.39
HH 1144	SSTI	*dfrA*	WT	250	>500	32.54
HH 1184	Sputum	*dfrK*	WT	>1000	>500	29.38
UCH MSSA 1	Sinus Cavity	*dfrG*	WT	>1000	>500	36.49
Sa43300	ATCC	None	WT	0.3125	10	38.16

To better understand the possible relationships between these strains, the genetic diversity was determined through sequencing and typing of the *spaA* gene[12]. The analysis showed that five of the strains (UCH MRSA115, UCH MRSA121, UCH MSSA1, HH MRSA714 and HH MRSA1144), including strains from both hospitals and the MSSA strain, were clonally indistinguishable. However, UCH MRSA127, HH MRSA1184 and UCH MRSA1 are clonally distinct isolates. Importantly, within the group of five clonal isolates, *dfrA* and *dfrG* are represented and *dfrK* is found the distinct yet related strain, HH MRSA 1184, Figure 2. The appearance of the different *dfr* isoforms within the closely related cluster as well as more genetically distinct strains suggests that they are on potentially highly mobile resistance elements.

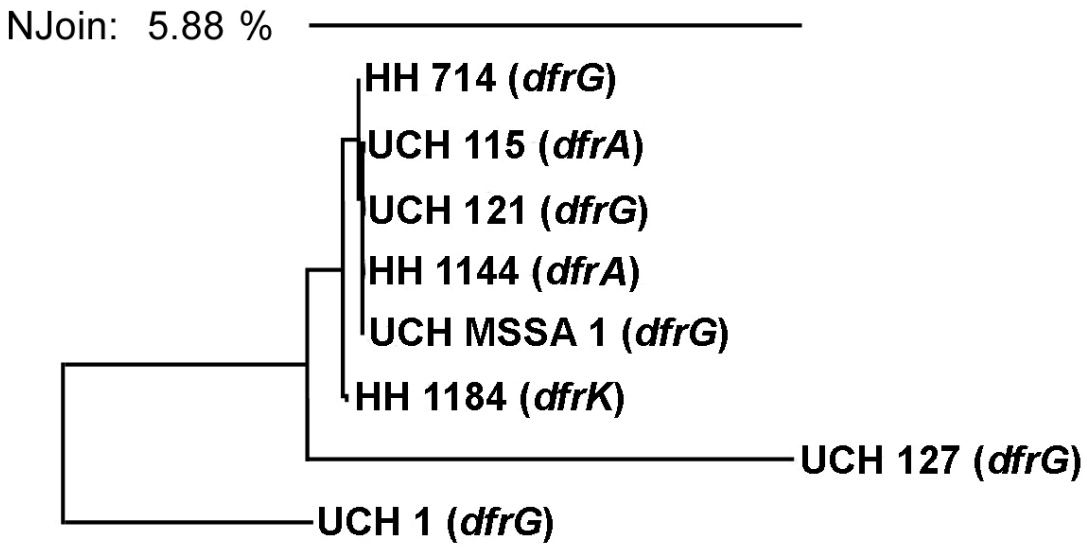

Figure 2 Clonal characterization of *S. aureus* strains by *spaA* sequencing

5.3 Clinical Isolates Exhibit a Range of Antibiotic Susceptibilities

The phenotypes to commonly prescribed non-TMP antibiotics were determined for the panel of isolates revealing diverse variability in susceptibilities. All strains were susceptible to vancomycin, linezolid, rifampin and daptomycin and have varied susceptibilities to sulfamethoxazole, erythromycin, clindamycin, tetracycline, gentamicin and a variety of fluoroquinolones, based on breakpoint MICs (Table 3). To better understand the diversity of the isolates, the remaining seven genomes were sequenced and the molecular mechanisms of resistances were identified. The only resistance mechanism that mirrors the clonality pattern is found with sulfamethoxazole; the group of five clonal strains contained five previously reported *folP* mutations (F17L, T28S, T59S, L64M, E205K) conferring high-level SMX resistance. Whereas, UCH 1 contains thirteen *folP* mutations (F17L, V30I, T31N, M37I, I58V, T59S, V60L, L64M, I110M, V117I, V126I,

E208K, F226L) and HH1184 contains nine (V30I, I58V, T59S,V60L, L64M, I100M, V117I, V126I, F226L)[13].

Table 3 Antibiotic Susceptibility Profiles of Clinical MRSA Isolates (μg/mL)

Strain	Erythromycin	Clindamycin	Tetracycline	Gentamicin	Levofloxicin
UCH 1	>4 (R)	≤0.12 (S)	≤2 (S)	≤2 (S)	64 (R)
UCH 115	<0.25 (S)	≤0.12 (S)	>16 (R)	>16 (R)	>64 (R)
UCH 121	>4 (R)	0.25 (S)	≤2 (S)	≤2 (S)	>64 (R)
UCH 127	>4 (R)	≤0.12 (S)	≤2 (S)	≤2 (S)	8 (R)
HH 714	2 (R)	≤0.12 (S)	≤2 (S)	≤2 (S)	>64 (R)
HH 1144	>4 (R)	>2 (R)	>16 (R)	>16 (R)	8 (R)
HH 1184	>4 (R)	0.25 (S)	≤2 (S)	≤2 (S)	0.25 (S)
UCH MSSA 1	>4 (R)	>2 (R)	≤2 (S)	≤2 (S)	8 (R)

TetM, a ribosome protection protein, is identified as the tetracycline resistance determinant observed in UCH115 and HH1144[14]. Gentamicin resistance in UCH115 and HH1144 is conferred by a plasmid borne AAC(6')-APH(2") aminoglycoside resistance enzyme[15]. Tetracycline and aminoglycoside resistance was only identified in strains containing *dfrA,* however these strains differ both in fluoroquinolone resistance mechanisms and macrolide susceptibility. *mphC*, a 2'-phosphotransferase which directly inactivates the macrolides via phosphorylation determines selective macrolide resistance (erythromycin) in UCH MRSA121, UCH MRSA127 and HH MRSA1184, all clonally distinct isolates[20,21]. *mphC* is not commonly reported to confer macrolide resistance in human *S. aureus* isolates, instead it is more frequently reported in agricultural studies[22]. *ermC*, a 23s rRNA methyl transferase, found in UCH MRSA 1, HH MRSA 1144 and UCH MSSA 1 confers resistance to both macrolides and lincosamines (clindamycin)[23].

Resistance to fluoroquinolone in all strains except HH MRSA1184 is conferred through a variety of mutations in the quinolone resistance-determining regions (QRDRs) of DNA gyrase subunit A (*gyrA)* and topoisomerase IV, subunits A and B (*grlA* and *grlB*). The combinations of mutations vary from single *gyrA* mutations to the accumulation of four mutations between *gyrA*, *grlA*, and *grlB* were observed[16,17]. NorA efflux activity in fluoroquinolone resistance was determined by MIC in the presence of reserpine, a NorA inhibitor. Minimal shifts in MIC for levofloxacin and up to 8-fold decrease in ciprofloxacin MIC indicate that NorA has minimal influence on fluoroquinolone resistance (Table 4)[18,19].

Table 4 Minimum Inhibitory Concentrations with 20 μg/mL Reserpine (μg/mL)

	Minimum Inhibitory Concentration		Minimum Inhibitory Concentration 20 μg/mL Reserpine	
Strain	Levofloxacin	Ciprofloxacin	Levofloxacin	Ciprofloxacin
UCH 1	64	>64	64 (1)	32 (≥2)
UCH 115	>64	>64	>64 (≥1)	32 (≥2)
UCH 121	>64	64	>64 (≥1)	32 (2)
UCH 127	8	32	4 (2)	8 (4)
HH 714	>64	64	>64 (≥1)	32 (2)
HH 1144	8	64	8 (1)	16 (4)
HH 1184	0.25	1	<0.125 (≥2)	<0.125 (>4)
UCH MSSA 1	8	64	8 (1)	32 (2)

Fold increases in MIC noted in parenthases

HH MRSA 1184 is the only strain to contain the Panton-Valenitine leukocidin, a virulence factor that produces a cytocoxin associated with tissue necrosis and leukocyte damage[24]. All strains clinically classified as 'methicillin resistant' via susceptibility are *mecA* positive. A full list of target mutations and resistance determinants are summarized in Table 5.

Table 5 Molecular Mechanisms of Antibiotic Resistance for Clinical Isolates

	Resistance Mechanism	MIC Range (ug/mL)	Strains
Trimethoprim	*dfrA*	250	UCH115, HH1144
	dfrG	>1000	UCH 1, UCH121, UCH127, HH714, UCH MSSA1
	dfrK	>1000	HH1184
Sulfamethoxazole	*folB*(F17L, V30I, T31N, M37I, I58V, T59S, V60L, L64M, I110M, V117I, V126I, E208K, F226L)	>500	UCH 1
	folB(F17L, T28S, T59S, L64M, E205K)	≥500	UCH 115, UCH 121, UCH127, HH714, HH1144, UCH MSSA1
	folB (V30I, I58V, T59S,V60L, L64M, I100M, V117I, V126I, F226L)	32	HH1184
Tetracycline	*TetM*	>16	UCH115, HH1144
Gentamicin	aac(2')-apc(6")	>16	UCH115, HH1144
Erythromycin	*mphC*	8-32	UCH121, UCH127, HH1184
	ermC	>64	UCH 1, HH 1144, UCH 1
Clindamycin	*ermC*	>64	UCH 1, HH 1144, UCH 1
Levofloxacin/ Ciproflxacin/ Gatifloxacin	*gryA*(S84R ,S85P), *grlA*(S80F), *grlB*(E471K)	64/ >64/>8	UCH 1
	gryA(S84L, S85P), grlA(S90K, E84K)	>64/>64/ >8	UCH115
	gryA(S84R ,S85P), *grlA*(S80F), *grlB*(D432V)	>64/64/>8	UCH121, HH714
	gyrA (S84L) and *grlA* (S80F), *grlB*(D432V, E596D*)	8/32/4	UCH127
	gyrA (S84L) and *grlA* (S80F)	8/64/4	HH1144
Levofloxacin/ Ciproflxacin	*gyrA*(S84L)	8/64	UCH 1

5.4 Propargyl-linked Antifolates Potently Inhibit Clinical Isolates

Whole genome sequencing of the clinical strains showed notable variation in the molecular basis of TMP resistance as well as several common antibiotics. This provided a useful panel of clinically relevant strains that can be used as an important tool for lead optimization. Therefore, we screened a variety of previously developed PLA lead compounds against the panel of TMP-resistant strains to identify candidates with broad activity. Excitingly, several of the compounds (UCP1039, UCP1164, UCP1172, UCP1173 and UCP1175; Table 5, Figure 3) showed very potent activity against these highly TMP-resistant strains. Although we observed activity with earlier generation inhibitors that contained a pyridyl C-ring (eg. UCP1039) the most potent activity was observed with a recently disclosed charged/zwitterionic series possessing an ionizable carboxylic acid on the distal C-ring (UCP1164, UCP1172, UCP1173 and UCP1175). Overall, the PLAs were most potent against strains carrying *dfrG* and *dfrK* with MIC values as low as 0.1563 *μ*g/mL, two-fold lower than the MIC for TMP against wild-type *S. aureus*. Compound UCP1173 showed the most potent activity against strains possessing *dfrA* with MIC values of 1.25 and 2.5 *μ*g/mL. Interestingly, compound UCP1172 is the antipode of UCP1173 but does not significantly inhibit *dfrA*-possessing strains.

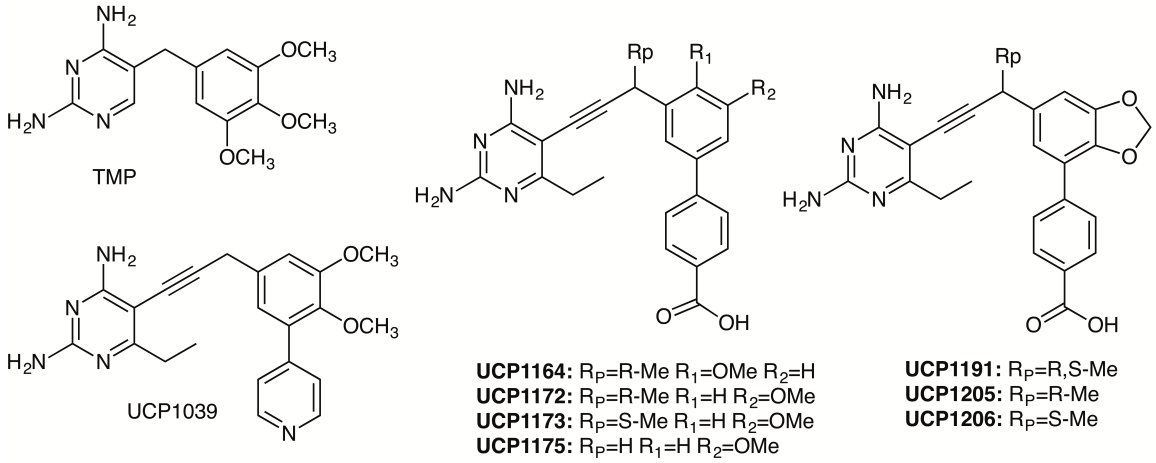

Figure 3 Structure of TMP and PLAs Described in this Chapter

Table 6 PLA Antibacterial Activity against Clinical Isolates (MICs in μg/mL)

Inhibitor	UCH 1 (*dfrG)*	UCH 115 (*dfrA)*	UCH 121 (*dfrG)*	UCH 127 (*dfrG)*	HH 714 (*dfrG)*	HH 1144 (*dfrA)*	HH 1184 (*dfrK)*	UCH MSSA 1 (*dfrG*)	ATCC 43300
UCP1039	1.25	>20	0.625	0.3125	1.25	>10	1.25	0.625	0.0391
UCP1164	2.5	10	5	2.5	5	5	0.625	5	0.0391
UCP1172	0.625	5	0.625	0.3125	0.625	5	0.3125	0.3125	0.0098
UCP1173	5	2.5	5	2.5	5	1.25	2.5	2.5	0.0098
UCP1175	2.5	>20	10	5	10	>20	5	10	0.0195
UCP1191	0.625	20	0.625	0.1563	0.625	10	0.1563	0.3125	0.0195
UCP1205	0.625	>10	0.625	0.3125	0.625	>10	0.3125	0.3125	0.0195
UCP1206	2.5	>10	2.5	1.25	2.5	>10	1.25	1.25	0.0098
UCP1191 +SMX[a]	0.0391	00.625	0.0781	0.3125	0.0391	0.625	≤0.0048	0.0098	≤0.0048

[a]MIC values with 100 μg/mL Sulfamethoxazole (SMX), ATCC 43300 and UCH 127 at 1 μg/mL SMX

It was noted that C3', C4' dioxygenation with a pyridyl C-ring (UCP1039) afforded some of the strongest activity in this series and as such, we investigated combining this pattern of functionality with the preference for a C-ring carboxylic acid. To explore this design, a dioxalane ring was chosen as a convenient isostere as it afforded antibacterial activity against strains that possessed a DHFR with the F98Y mutation[25]. The racemic inhibitor UCP1191 and the individual enantiomers, UCP1205 and UCP1206, were therefore synthesized and evaluated. We were delighted to see a significant increase in activity against both *dfrG*- and *dfrK*-possessing strains with MIC values of 0.1563-0.625 μg/mL. Interestingly, despite these strains also being SMX-resistant, an apparently strong synergistic interaction between the PLAs and SMX was observed (Tables 6 and 7).

Table 7 Minimum Inhibitory Concentrations with 100 μg/mL Sulfamethoxazole (μg/mL)

Strain		UCP1039	UCP1164	UCP1172	UCP1173	UCP1191	UCP1205	UCP1206
UCHC 115	*dfrA*	1.25	0.3125	1.25	0.1563	0.625	2.5	0.625
HH 714	*dfrG*	0.0391	0.3125	0.3125	0.3125	0.0391	0.0391	0.1563
HH 1184	*dfrK*	≤0.0048	≤0.0048	≤0.0048	≤0.0048	≤0.0048	≤0.0048	≤0.0048

Cloning, expressing, purifying and evaluating enzyme inhibition provided further validation that antibacterial activity of the PLAs in these resistant organisms was directly related to their ability to inhibit the resistance-conferring enzymes. The three genes, *dfrA*, *dfrG* and *dfrK* were cloned into expression vectors and the resulting proteins purified to homogeneity. The PLAs were evaluated for enzyme inhibition using standard assays that measure the oxidation of the NAPDH cofactor (Table 7)[25,26]. As expected, TMP exhibits high inhibition concentration 50 % (IC_{50}) values for all three TMP-resistant DHFRs.

Despite the fact that there has been no directed optimization of the PLAs against these TMP-resistant proteins, the PLAs showed relatively potent inhibition with the majority of IC_{50} values less than 100 nM, highlighting the value of our approach to use structure-based targeting of common resistance mechanisms in DHFRs[25,27]. Remarkably, this is an approximately 4400-, 55-, or 2000-fold increase in potency over TMP for the DfrG, DfrA and DfrK proteins, respectively. Although a variety of factors beyond target inhibition contribute to the overall antibacterial activity, there is a correlation between PLA activity against the TMP-resistant enzymes and the MICs against the corresponding strains. Additional validation that the PLAs exert their antibiotic effect through blockade of the folate pathway was provided by rescue experiments, where the culture media was supplemented with thymidine and MIC values rose by at least 8-fold (data not shown).

Table 8 Enzyme Inhibition (IC_{50} values shown in μM)

Inhibitor	DfrB	DfrG	DfrA	DfrK
TMP	0.023 $\pm$ 0.002	380 $\pm$ 12	15.1 $\pm$ 0.7	43 $\pm$ 2
UCP1039	0.014 $\pm$ 0.001	0.45 $\pm$ 0.02	0.36 $\pm$ 0.02	0.022 $\pm$ 0.003
UCP1164	0.037 $\pm$ 0.002	1.4 $\pm$ 0.1	8.8 $\pm$ 0.9	0.073 $\pm$ 0.002
UCP1172	0.0089 $\pm$ 0.0007	0.22 $\pm$ 0.02	0.41 $\pm$ 0.01	0.030 $\pm$ 0.001
UCP1173	0.014 $\pm$ 0.001	0.19 $\pm$ 0.01	0.27 $\pm$ 0.02	0.091 $\pm$ 0.008
UCP1175	0.0110 $\pm$ 0.0006	1.4 $\pm$ 0.2	0.98 $\pm$ 0.008	0.17 $\pm$ 0.01
UCP1191	0.010 $\pm$ 0.0002	0.087 $\pm$ 0.005	0.32 $\pm$ 0.03	0.041 $\pm$ 0.006
UCP1205	0.018 $\pm$ 0.003	0.159 $\pm$ 0.007	0.34 $\pm$ 0.01	0.10 $\pm$ 0.01
UCP1206	0.017 $\pm$ 0.002	0.19 $\pm$ 0.01	0.18 $\pm$ 0.03	0.054 $\pm$ 0.005

5.5 Structural Basis of Activity of PLAs in Clinical Isolates

Analysis of the crystal structures of the potent inhibitors, UCP1175 and UCP1191, complexed with DfrB and NADPH reveal a structural basis for activity of these inhibitors. It appears that the binding position of the inhibitors, influenced on substitutions at both the propargyl positions and the B-ring, is critical for achieving potent activity. The carboxylate moiety of UCP1191 forms one direct ionic bond to Arg 57 and one water-mediated hydrogen bond to Arg 57 and Lys 32, wherase UCP1175, which lacks the methyl substitution at the propargly position, forms an extensive water network with Arg 57 and carboxylate[28]. Furthermore, the structure of UCP1106, which retains no activity in these resistant enzyme shows a water mediated interaction between the PLA and the enzyme. In this structure, however, the water is more closely associated with the PLA and does not form a proper interaction with Arg 57.

It appears that the propargyl methyl of UCP1191 pushes the biphenyl system further into the active site and within bonding distance to Arg 57 and the lack of substitution at the propargyl position and 2' B-ring positions allows for the formation of an evenly dispersed water network, as there is a greater distance between Arg 57 and the carboxylate. UCP1106, which binds in an intermediate position, dictated by the 2-OMe B-ring substitution, does not allow for the even water formation and therefore forms a less stable complex with the enzyme (Figure 4). Arg 57 is conserved in all of the TMP-resistant enzymes (Figure 5) and forms a similar key contact with dihydrofolate, suggesting that this contact is less likely to mutate to cause resistance to the PLAs.

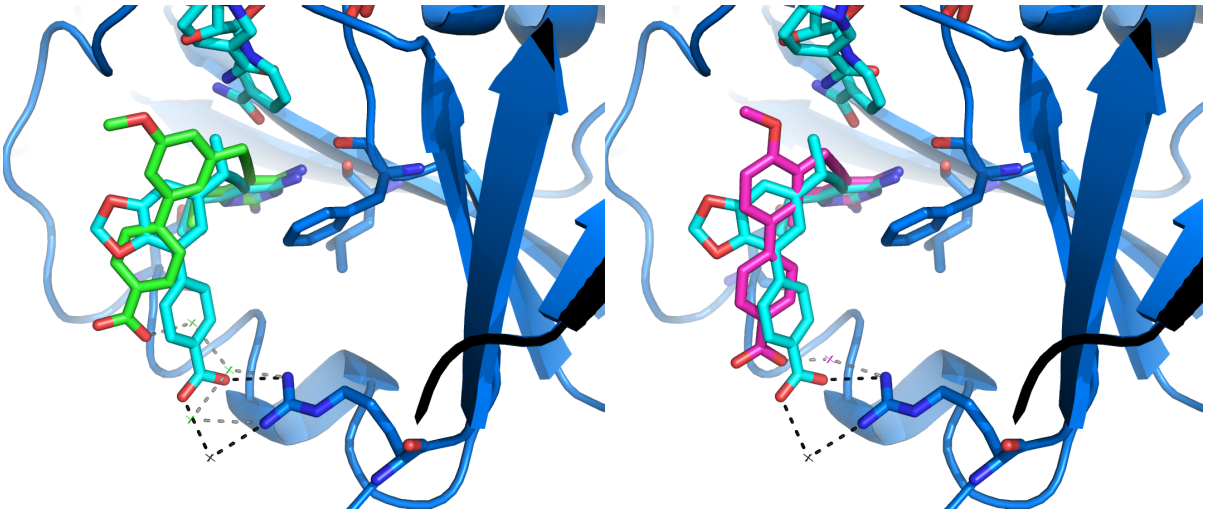

Figure 4 a) Water mediated binding interactions of UCP1175 (green) compared to the binding of UCP1191 (blue). b) Binding interactions of UCP1106 (magenta) compared to the binding of UCP1191 (blue). All inhibitors are co-crystallized with DfrB and NADPH.

The TMP-resistant enzymes tend to conserve their mechanisms of reducing TMP affinity (Figure 5). Leu 5 is an isoleucine in the TMP-resistant enzymes; this mutation would disturb Phe 92, which is critical both for hydrogen bonding to 4- amino group of the diaminopyrimidine as well as hydrophobic interactions with the linker. Leu 28 is a tyrosine in DfrG and DfrK and Val 31 is Ile in DfrA; these mutations also perturb Phe 92 (38). The Val 31 Ile mutation was predicted by K* in the OSPREY suite to cause resistance to an earlier PLA, and in fact reduced affinity by 60-fold[29]. Crystal structures of the double mutant enzyme, F98Y/V31I, show the perturbation of Phe 92. His 30 mutations have been observed clinically and studied extensively in the *dfrB* gene[3]. While the mutation His 30 Asn has been shown to disrupt the water network stabilizing the pyrimidine ring[27, 30], the TMP-resistant enzymes DfrK and DfrG carry a tyrosine at this position, which may achieve the same goal. Finally, all three TMP-resistant enzymes maintain a tyrosine at position 98 (wt Phe). The tyrosine has been shown to perturb NADPH binding[25,26] and to decrease synergistic binding between TMP and NADPH[31]. Previous design efforts

focused on achieving inhibitor potency against the mutations observed in the chromosomal copy, *dfrB*, such as the Phe98Tyr-mutated DHFR enzyme[25,27,31,32].

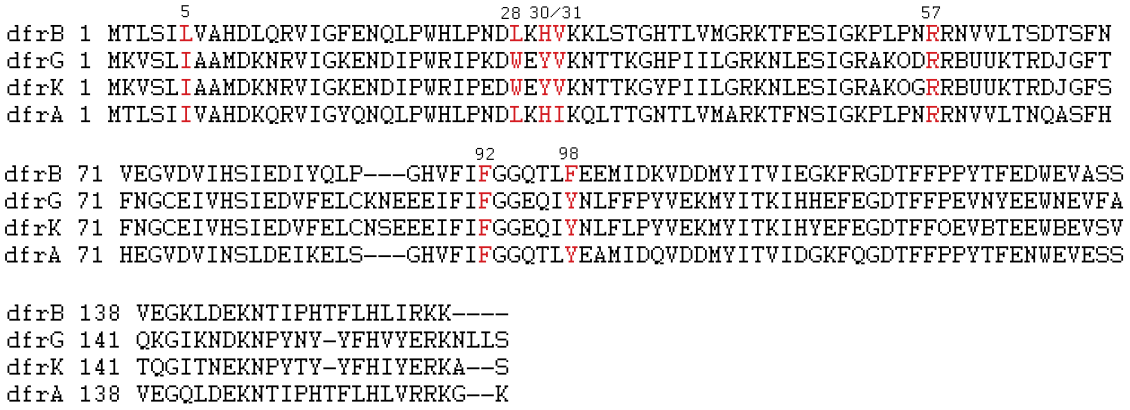

Figure 5 Protein sequence alignment of the *dfr* isoforms. Interesting amino acids are highlighted in red.

These efforts may prove valuable as the TMP-resistant enzymes DfrG, DfrK and DfrA all possess a tyrosine residue at position 98. As shown here, designing inhibitors against the F98Y chromosomal mutant provided a significant advantage in achieving superior potency against these resistant enzymes, as they appear to rely on common mechanisms. Recently, we described potent activity of the COOH-PLA series, specifically UCP1164, UCP1172, UCP1173 and UCP1175 against strains containing these clinically relevant point mutations in *dfrB*. Including F98Y, H30N/F98Y and F98Y/H149R. While the COOH-PLAs are more potent against the single F98Y mutant strain than the acquired *dfr* isoforms, UCP1164 and UCP1172 maintain superior activity against the acquired resistance elements over the double mutants[27]. The remaining compounds display similar inhibitory activity in the acquired and mutant DHFR enzymes. As the mutations that confer TMP resistance appear to belong to a conserved and relatively manageable group, future design efforts can capitalize on this group to optimize ligands that inhibit the majority of clinically observed TMP-resistant species.

5.6 Conclusions

By investigating the contemporary mechanisms of TMP resistance, we are able to show, within a small collection of clinical TMP^R *S. aureus* isolates, the surprising preponderance of TMP^R elements that have never been identified domestically. Genomic analysis of the strains indicates an even wider diversity of mechanisms and susceptibilities to commonly used antibiotics. This genetic analysis of the strains is representative of the extensive spread of antibiotic resistances and supports the thoughts that these elements are easily transferred between bacteria, suggesting that occurrence of these genes may be much wider than reported.

Only by understanding the structural mechanisms of TMP resistance are we able to continue design of propargyl-linked antifolates that potently inhibit both TMP-resistant enzymes and the strains harboring these elements. Here, the identification of the *dfrA*, *dfrG* and *dfrK* genes in clinical isolates has validated the efforts to design robust inhibitors that can overcome mutational changes in the enzyme. These efforts have yielded a class of carboxylate substituted PLAs that exhibit unprecedented activity directly against these highly resistant elements, resensitizing these antifolate resistant strains to PLAs. Furthermore, the clinical relevancy of the compounds remains acute as timely clinical data drive compound design.

5.7 Acknowledgments

I would like to thank Dr. Narendran G-Dayanadan, Eric Scocchera and Dr. Santosh Keshipeddy for the synthesis of compounds reported here. I would also like to recognize Jolanta Kruscinka for assisting in the expression and purification of DfrG and Behnoush Haijan for the expression and purification of DfrA. Dr. Jeff Aeschlimann provided clinical

strains from UCONN Health/ John Dempsey Hospital and Dr. Michael Nailor provided strains from Hartford Hospital. Finally, I would like to thank Lidia Beka and Dr. Joerg Graf, PhD for assistance in assembling the genomes and the UCONN MARS facilities, specifically Kendra Maas, for assistance with whole genome sequencing.

5.8 References

1. Houvinen, P. Increases in Rates of Resistance to Trimethoprim. *Clin. Infect. Dis.* **1997**, *24*, 63-66.
2. Dale, G. E., Broger, C., Hartman, P. G., Langen, H., Page, M. G. P., Then, R.;, D. Characterization of the gene for the chromosomal dihydrofolate reductase (DHFR) of Staphylococcus epidermidis ATCC 14990: The origin of the trimethoprim-resistant S1 DHFR from Staphylococcus aureus? *J. Bacteriol.* **1995**, *177*, 2965–2970.
3. Dale, G.; Broger, C.; D'Arcy, A.; Hartman, P.; DeHoogt, R.; Jolidon, S.; Kompis, I.; Labhardt, M.; Langen, H.; Locher, H.; et al. A single amino acid substitution in Staphylococcus aureus dihydrofolate reductase determines trimethoprim resistance. *J. Mol. Biol.* **2007**, *266*, 23–30.
4. Sekiguchi, J.; Tharavichitkul, P.; Miyoshi-Akiyama, T.; Chupia, V.; Fujino, T.; Araake, M.; Irie, A.; Morita, K.; Kuratsuji, T.; Kirikae, T. Cloning and characterization of a novel trimethoprim-resistant dihydrofolate reductase from a nosocomial isolate of Staphylococcus aureus CM. S2 (IMCJ1454). *Antimicrob. Agents Chemother.* **2005**, *49*, 3948–3951.
5. Nurjadi, D.; Olalekan, A.; Layer, F.; Shittu, A. O.; Alabi, A.; Ghebremedhin, B.; Schaumburg, F.; Hofmann-Eifler, J.; Van Genderen, P.; Caumes, E.; et al. Emergence of trimethoprim resistance gene *dfrG* in Staphylococcus aureus causing human infection and colonization in sub-Saharan Africa and its import to Europe. *J. Antimicrob. Chemother.* **2014**, *69*, 2361–8.
6. Brennen, G.; Yvonne, A.; Burns, A.; Leonard, F.; McManus, A.; O'Connell, B.; Coleman, D.; Shore, A. The Emergence and Spread of Multiple Live-Stock Associated Clonal Complex 398 Methicillin-Resistant and Methicillin-Susceptible *Staphylococcus aureus* Strains among Animals and Humans in the Republic of Ireland, 2010-2014. *Plos One,* **2016**, *11*, 1-11.
7. Kaldec ,K.; Schwarz, S. Identification of a Novel Trimethoprim Resistance Gene, *dfrK*, in a Methicillin-Resistant *Staphylococcus aureus* ST398 Strain and Its Physicla Linkage to the Tetracycline Resistance Gene *tet*(L). *Antimicrob. Agents Chemother.* **2009**, *53,* 776-778.
8. Kadlec, K.; Schwarz, S. Identification of a plasmid-borne resistance gene cluster comprising the resistance genes erm(T), dfrK, and tet(L) in a porcine methicillin-resistant Staphylococcus aureus ST398 strain. *Antimicrob. Agents Chemother*. **2010**, *54*, 915–918.

9. Sader, H.; Farrell, D.; Flamm, R.; Jones, R. Activity of ceftaroline and comparator agents tested against Staphylococcus aureus from patients with bloodstream infections in US medical centres (2009-13). *J. Antimicrob. Chemother.* **2015**, *70*, 2053–2056.
10. Pate, A.; Terribilini, R.; Ghobadi, F.; Azhir, A.; Barber, A.; Pearson, J.; Kalantari, H.; Hassen, G. Antibiotics for methicillin-resistant Staphylococcus aureus skin and soft tissue infections: the challenge of outpatient therapy. *Am. J. Emerg. Med.* **2014**, *32*, 135–138.
11. Bergmann, R.; Van Der Linden, M.; Chhatwal, G.; Nitsche-Schmitz, D. Factors that cause trimethoprim resistance in Streptococcus pyogenes. *Antimicrob. Agents Chemother.* **2014**, *58*, 2281–2288.
12. Petersson, A.; Olsson-Liljequist, B.; Miörner, H.; Haeggman, S. Evaluating the usefulness of spa typing, in comparison with pulsed-field gel electrophoresis, for epidemiological typing of methicillin-resistant Staphylococcus aureus in a low-prevalence region in Sweden 2000-2004. *Clin. Microbiol. Infect.* **2010**, *16*, 456–462.
13. Hampele, I. C.; D'Arcy, A.; Dale, G.; Kostrewa, D.; Nielsen, J.; Oefner, C.; Page, M.; Schönfeld, H.; Stüber, D.; Then, R. Structure and function of the dihydropteroate synthase from Staphylococcus aureus. *J. Mol. Biol.* **1997**, *268*, 21–30.
14. Trzcinski, K.; Cooper, B.; Hryniewicz, W.; Dowson, C. Expression of resistance to tetracyclines in strains of methicillin-resistant *Staphylococcus aureus*. *J. Antimicrob. Chemother.* **2000**, *45*, 763-770.
15. Daigle, D.; Hughes, D.; Wright, A. Prodigious substrate specificity of AAC(6')-APH(2"), an aminoglycoside antibiotic resistance determinant in enterococci and staphylococci. *Chem. Biol.* **1999**, *6*, 99-110.
16. Schmitz, F.; Jones, M.; Hofmann, B.; Hansen, B.; Scheuring, S.; Luckefahr, M.; Fluit, A.; Verhoef, J.; Hadding, U.; Heinz, H.; Kohrer, K. Characterization of *grlA, grlB, gyrA* and *gyrB* Mutations in 116 Unrelated Isolates of *Staphylococcus aureus* and Effects of Mutations on Ciprofloxacin. *Antimicrob. Agents Chemother*. **1998**, *42*, 1249-1252.
17. Pan, X.; Hamlyn, P.; Talens-Visconti, R.; Alovero, F.; Manzo, R.; Fisher L. Small-Colony Mutants of *Staphylococcus aureus* Allow Selection of Gyrase-Mediated Resistance to Dual-Target Fluoroquinolones*. Antimicrob. Agents Chemother.* **2002**, *46*, 2498-2506.
18. Kaatz, G.; Seo, S. Inducible NorA-Mediated Multidrug Resistance in *Staphylococcus aureus*. *Antimicrob. Agents Chemother.* **1995**, *39*, 2650-2655.
19. Aeschlimann, J.; Dresser, L.; Kaatz, G; Rybak, M. Effects of NorA Inhibitors on In Vitro Antibacterial Activities and Postantibiotic Effects of Levofloxacin, Cirpofloxacin and Norfloxacin in Genetically Related Strains of *Staphylococcus aureus. Antimicrob. Agents Chemother.* **1999**, *43*, 225-340.
20. Matsuoka, M.; Inoue, M.; Endo, Y.; Nakajima, Y. Characterization and expression of three genes, *msr*(A), *mph*(C) and *erm*(Y), that confer resistance to macrolide antibiotics in *Staphylococcus aureus*. *FEMS Micro. Lett.* **2003**, *220,* 287-293*.*
21. Juda, M.; Chudzik-Rzad, B.; Malm, A. The prevalence of genotypes that determine resistance to macrolides, lincosamides, and streptogramins B compared with

spiramyin susceptibility among erythromycin-resistant *Staphylococcus eidermidis*. *Mem Inst Oswaldo Cruz,* **2016**, *111*, 155-160.
22. Li, L.; Feng, W.; Zhang, Z.; Xue, H.; Zhao, X. Macolide-lincosamide-streptogramin resistance phenotypes and genotypes of coagulase-positive *Staphylococcus aureus* and coagulase-negative staphylococcal isolates from bovine mastitis. *BMC Vet, Res.* **2015**, *11*, 1-8.
23. Khan, S.; Nawasz, M.; Khan, A.; Cerniglia, C. Simultaneous detection of erythrmycin-resistant methylase genes *ermA* and *ermC* from *Staphylococcus* spp. by multiplex-PCR. *Mol. and Cell Probes* **1999**, *13*, 381-387.
24. Lina, G.; Piemont, Y.; Godail-Gomot, F.; Bes, M.; Peter, M.; Gauduchon, V.; Vandenesch, F.; Etienne, J. Panton-Valenitine Leukocidin in Staphylococcal Infections. *Clin. Infect. Dis.* **1999**, *29*, 1128-1132.
25. Keshipeddy, S.; Reeve, S.; Anderson, A.; Wright, D. Non-racemic Antifolates Stereo-selectively Recruit Alternate Cofactors and Overcome Resistance in S. aureus. *J. Am. Chem. Soc*. **2015**, *137*, 8983-8990.
26. Frey, K.; Liu, J.; Lombardo, M.; Bolstad, D.; Wright, D.; and Anderson, A. Crystal Structures of Wild-type and Mutant Methicillin-resistant Staphylococcus aureus Dihydrofolate Reductase Reveal an Alternate Conformation of NADPH That May Be Linked to Trimethoprim Resistance. *J. Mol. Biol.* **2009**, *387*, 1298–1308.
27. Reeve, S.; Scocchera, E.; Ferriera, J.; Dayanadan, N.; Keshipeddy, S.; Wrght, D.; Anderson, A. Charged Propargyn-LInked Antifolate Reveal Mechaninisms of Antifoalte Resistance and Inhibit Trimethoprim-Resistant MRSA Strains Possessing Clinically Relevant Mutations. *J. Med. Chem.* ***2016****, 59*, 6493-6500.
28. Scocchera, E.; Reeve, S.; Keshipeddy, S.; Lombardo, M.; Hajian, B.; Sochia, A.; Alverson, J.; Priestley, N.; Anderson, A.; Wright, D. Charged Nonclassical Antifolates with Activity Against Gram-Positive and Gram-Negative Pathogens. *ACS Med. Chem. Lett.* **2016**, *7*, 692-696.
29. Reeve, S.; Gainza, P.; Frey, K.; Georgiev, I.; Donald, B.; Anderson, A. Protein design algorithms predict viable resistance to an experimental antifolate. *Proc. Natl. Acad. Sci. U. S. A.* **2014**,*112*, 749-754.
30. Frey, K.; Lombardo, M; Wright, D.; Anderson, A. Towards the understanding of resistance mechanisms in clinically isolated trimethoprim-resistant, methicillin-resistant Staphylococcus aureus dihydrofolate reductase. *J. Struct. Biol.* **2010,** *170*, 93–97.
31. Heaslet, H.; Harris, M.; Fahnoe, K.; Sarver, R.; Putz, H.; Chang, J.; Subramanyam, C.; Barreiro, G.; Miller, J. Structural comparison of chromosomal and exogenous dihydrofolate reductase from Staphylococcus aureus in complex with the potent inhibitor trimethoprim. *Proteins Struct. Funct. Bioinforma*. **2009**, *76*, 706–717.
32. Oefner, C.; Bandera, M.; Haldimann, A.; Laue, H.; Schulz, H.; Mukhija, S.; Parisi, S.; Weiss, L.; Lociuro, S.; Dale, G. Increased hydrophobic interactions of iclaprim with Staphylococcus aureus dihydrofolate reductase are responsible for the increase in affinity and antibacterial activity. *J. Antimicrob. Chemother.* **2009,** *63*, 687-698.

Chapter 6

Final Analysis and Future Directions

6.1 Continued Development of Propargyl-linked Antifolates

Through the process of structure based drug design, a class of novel antifolates has been optimized against *S. aureus* DHFR enzymes. Adding an acetylene linker and building the compounds from simple trimethoprim derivatives and exploiting crucial enzymatic interactions through rational inhibitor modifications has lead to a diverse library of propargyl-linked antifolates. It is shown that combination of R_P, B-ring and C-ring substitutions can lead to highly favorable interactions that translate into increased cellular and enzymatic potency. Specifically, compounds with R_1-OMe substitutions on the carboxylate PLA scaffold results in reduced potency compared to the R_2 and R_2/R_3 positions when a R_P methyl is present. Crystal structures indicate that the R_P methyl dictates the binding position when no R_1 substituent is present and provides an optimal orientation for direct ionic interactions with Arg 57. Currently, the most potent compounds in this class make one direct and one water mediated interaction with Arg 57. Additional modifications to the compounds, including exploring C-ring substituents and B-/C-ring linkers can optimize the interaction between the carboxylate and Arg 57 guanidinium to better mimic DHF. Overall, these compounds are selective for the pathogenic enzymes over the human isoform and maintain activity regardless in *S. aureus* associated DHFR enzymes regardless of their identity.

A single crystal structure of UPC1191, a R_P-methyl substituted *p*-COOH indicates the important role of the propargylic methyl in the carboxylate series of PLAs. Comparisons of this structure with structures co-crystallized with UCP1106 and UCP1175 (hydrogen-substituted R_P) indicates that this substituent is crucial for optimized interactions with the

enzyme. Additional crystal structures of an enantiomer pair, for example UCP1172 and UCP1173 or UCP1205 and UCP1206, would elucidate differences in the pyridine and carboxylate substituted enantiomers. It is believed that the presence of the carboxylate and its hydrogen bonding abilities will dictate the binding position of the biaryl system as opposed to the distinct binding of the pyridine enantiomers. In this case, enantiomerically pure compounds would not be necessary for optimized potency, reducing both costs and time during PLA development.

In addition to being potential therapeutic candidates, these small molecule inhibitors can also be used as probes into the structure and function of the DHFR enzymes. Specifically, stereospecific modifications to the propargylic position can influence both the cofactor and biphenyl system binding. Through investigations with these compounds, it has been discovered that the cofactor-binding site can accommodate an alternative configuration, indicating plasticity and flexibility of the protein. Continued investigations to the mechanism by which this alternate cofactor is generated and its biological relevance should be pursued. The β- to α-NADPH anomerization requires a ring opening and ring closing mechanism, which occurs at an equilibrium that heavily biases the β-anomer. However, the tautomerization of the α-NADPH to the closed-ring tricyclic NADPH analogue does not occur under typical thermodynamic and chemical environments.

It is believed that the extended α-NADPH binds the tertiary PLA/ enzyme complex and PLA binding induces the reorientation of the internals NAPDH phosphates stabilizing the tricyclic NADPH intermediate. Once stabilized, the enzyme can facilitate the cyclization reaction if oriented correctly with charged side chains[1]. Conversely, t-NADPH might be generated in solution under crystallization conditions and recruited to the active site,

however due to variances in the crystallography conditions this option is less likely. Crystal structures indicate that shifts in the acetylene linker binding position correlates with identity of NADPH recruited to the active site. Understanding whether or not the PLA binding positions and alternative NADPH is an artifact in crystallography or a product of PLA binding should be investigated. Experiments that quantitatively look for the conversion of β-NADPH to t-NADPH in solution with the enzymes and PLA can be designed, following standard biotransformation protocols and measured using analytical methods[2].

6.2 Understanding Antifolate Resistance

A comprehensive evaluation of resistance during the development of PLAs against trimethoprim resistant *S. aureus* lead to a better understanding of antifolate resistance. These efforts include prediction and prospective mutational resistance and determination of the contemporary mechanisms of clinical TMP resistance. During these studies we identified a series of mutations the enzyme can make to evade inhibition to a lead PLA and determined that these mutations are common among endogenous and acquired TMP resistance mechanisms. These studies also allowed us to understand the molecular mechanisms of resistance and not only design inhibitors that show potent activity across TMP^R enzymes but that are also less susceptible to developing mutational resistance.

The discovery of the DfrG and DfrK enzymes in clinical MRSA isolates from Connecticut hospitals and lack of point mutations resulted in the reevaluation of clinical antifolate resistance. Until this point, compounds were designed with the understanding that DfrA and mutations in DfrB were responsible for clinical resistance. However, just because point mutations weren't identified in the TMP^R enzymes, doesn't mean that they can't

arise in response to antibiotic pressure and later confer resistance. This study indicated large diversity in the molecular mechanisms of resistance, even among clonal isolates, for trimethoprim as well as other common and important antibiotics. In fact, no two strains shared the same resistances for the antibiotics evaluated. Importantly, the design of PLAs inhibitors to overcome point mutations resulted a series of compounds that are show superior potency against these resistant strains, despite their diversity.

It is important to determine the prevalence of these TMP resistance elements. While unlikely, it is possible that they are contained within these two Connecticut hospitals. By acquiring TMP^R *S. aureus* isolates from around the country, we can evaluate the distribution and relevance of these genes. A more comprehensive, nation-wide epidemiological study would allow for more accurate overall TMP^R and specific TMP^R gene clinical frequencies. Due to the ease and accessibility of whole genome sequencing, it is plausible to sequence and evaluate a sample of isolates for antifolate and other antibiotic resistances. Additionally, the PLA susceptibiliites can be screened against a much larger bank of TMP^R *S. aureus isolates.*

The development of the enantio-pure COOH-PLAs, specifically UCP1172, UCP1173, UCP1205 and UCP1206, showed high potency against TMP^R mutants and acquired DHFR enzymes and are promising lead compounds for continued pre-clinical evaluations. Prospective mutational resistance of this class should be evaluated against the endogenous DHFR as well as the plasmid acquired *dfrA, dfrG,* and *dfrK* genes. Because activity of these PLAs largely relies on the ionic interaction between the carboxylate and Arg57, mutations at this position would likely result in decreased potency of the inhibitor. However, Arg 57 is crucial for the binding of DHF and mutation of this position would

likely result in a significant loss in enzymatic fitness. Experiments generating mutations to these inhibitors against the panel of *dfr* isoforms would further elucidate their potential evolution. Additionally, the frequency at which resistance develops *in-vitro* to these inhibitors would confirm or reject the design principles of exploiting non-mutational interactions to avoid resistance generation, especially when compared to their pyridine counterparts. In these studies, the over expression of DHFR should also be evaluated as the continued accumulation of mutations would likely result in unfit enzymes; a second resistance mechanisms would likely arise in this case.

Of the top 25 mutations predicted by K*, the acquired DHFR enzymes contain five of the predicted resistance conferring amino acids for DfrA, DfrG and DfrK. These mutations include L5I and V30I for DfrA and L5I, L28W, L20I and V6A for DfrG and DfrK. Interestingly, the resistance associated amino acids identified by K* in DfrA are both in top three ranked mutations and the PLAs are much less active against this enzyme. Not only does this indicate that there are only few modifications that the enzyme can make to confer resistance, but it also validates the use of these algorithms in early stage drug discovery efforts.

Unlike DfrA, little is known about DfrK and DfrG. Until these studies, only the crude K_M and TMP IC_{50} values were previously described[3,4]. Efforts into determining the structures of these enzymes in complex with TMP and potent PLAs can be used to elucidate both the mechanism of resistance for the enzymes against TMP and the mechanism of action of PLAs. DfrA is less susceptible to TMP (although it confers high levels of resistance) and less affected by the PLAs, compared to DfrG and DfrK. A biochemical and structural understanding of these enzymes would greatly aid in the development of antifolates and

elucidate DfrA's unique mechanism of PLA resistance allowing for the generation of inhibitors with potent activity against this stubborn enzyme.

6.3 Conclusions

Structure based drug design efforts for a novel class of antifolates resulted in a series of potent inhibitors that exhibit selectively potency against antifolate resistant and susceptible *S. aureus.* These efforts required understanding of the enzymatic and cellular structure activity relationship of the PLAs with the including the importance of enantio-pure inhibitors. Designing the inhibitors to overcome known clinical DfrB mutations resulted in a class of compounds that restore antifolate susceptibility to highly TMP^R *S. aureus* strains. In doing this, we discovered that plasticity in the cofactor-binding site and identified a novel NADPH configuration believed to exist in response to PLA binding.

In order to develop PLAs to overcome TMP^R, a comprehensive of understanding of clinical antifolates was required. In doing this, we isolated a panel of strains containing mutations common to both PLAs and TMP. Investigations into these strains resulted in a molecular understanding in their mechanisms of resistance as well as the mechanism of action of a potent PLA. Until this point, point mutations and the acquisition of a single innately resistant DHFR enzyme were believed to confer clinical resistance. However, our investigations indicate that a novel gene, *dfrG*, never previously reported in the United States, is responsible for the majority of clinical TMP resistance; we were also able to identify *dfrK* for the first time as well as the previously described *dfrA* gene, both of which occurred as minor determinants. PLAs designed to overcome the point mutations showed

potent activity against both the resistant enzymes and *S. aureus* strains, resulting in a promising class of inhibitors.

6.4 Acknowledgments

None of the work presented here would have been possible without the guidance and mentorship of Dr. Amy Anderson and Dr. Dennis Wright, the support of current and past graduate students and numerous collaborators; specifically, Dr. Kathleen Frey for her initial work in PLA development and resistance evaluations and Dr. Janet Paulsen for her technical guidance and mentorship. I would also like to thank current and past students and research faculty Dr. Mike Lombardo, Dr. Wangda Zhou, Jacob Ferreira, Eric Scocchera, Dr. Narendran G-Dayanan, Dr. Santosh Keshipeddy, Dr. Kishore Viswanathan, Behnoush Hajian and Jolanta Krusckina for their experimental support, scholarly discussions and friendships. I would also like to thank Dr. Bruce Donald, Dr. Eric May, Dr. Michael Nailor, Dr. Jeffrey Aeschlmann and their students Dr. Pablo Gainza, Lidia Beka and Jason Pattis for their collaborations, scientific contributions and their academic insights. Additionally, I would like to thank Dr. Jeffrey Aeschlimann and Dr. Marcy Balanus for their service on my Dissertation Committee. I would like to recognize Dr. Victoria Robinson and Dr. Celia Schiffer for their mentorship, scholarly discussions and investment into my academic success and future. Finally, I would like to acknowledge the support of the University of Connecticut's School of Pharmacy, its staff and National Institutes of Health for their financial contributions to this work.

6.5 References

1) Oppenheimer, N. J.; Kaplan, N. O. Structure of the Primary Acid Rearrangement Product of Reduced Nicotinamide Adenine Dinucleotide (NADH). *Biochemistry* **1974**, *13* (23), 4675–4685.

2) Brandon, E. F. A.; Raap, C. D.; Meijerman, I.; Beijnen, J. H.; Schellens, J. H. M. An Update on in Vitro Test Methods in Human Hepatic Drug Biotransformation Research: Pros and Cons. *Toxicol. Appl. Pharmacol.* **2003**, *189* (3), 233–246.

3) Sekiguchi, J.; Tharavichitkul, P.; Miyoshi-Akiyama, T.; Chupia, V.; Fujino, T.; Araake, M.; Irie, A.; Morita, K.; Kuratsuji, T.; Kirikae, T. Cloning and Characterization of a Novel Trimethoprim-Resistant Dihydrofolate Reductase from a Nosocomial Isolate of Staphylococcus Aureus CM.S2 (IMCJ1454). *Antimicrob. Agents Chemother.* **2005**, *49* (9), 3948–3951.

4) López, M.; Kadlec, K.; Schwarz, S.; Torres, C. First Detection of the Staphylococcal Trimethoprim Resistance Gene *dfrK* and the *dfrK* -Carrying Transposon Tn *559* in Enterococci. *Microb. Drug Resist.* **2012**, *18* (1), 13–18.

Appendices
Table of Contents

Appendix A Primary Citations

The work presented in this dissertation were adapted from the following publications:

Chapter 1

Reeve, S. M.; Lombardo, M. N.; Anderson, A. C. Understanding the Structural Mechanisms of Antibiotic Resistance Sets the Platform for New Discovery. *Future Microbiol.* **2015,** *10* (11), 1727-1733. **DOI:** 10.2217/fmb.15.78

Chapter 2

Keshipeddy, S.; Reeve, S. M.; Anderson, A. C.; Wright, D. L. Non-Racemic Antifolates Stereo-Selectively Recruit Alternate Cofactors and Overcome Resistance in S. Aureus. *J. Am. Chem. Soc.* **2015,** *137* (28), 8983-8990. **DOI:** 10.1021/jacs.5b01442

Scocchera, E.; Reeve, S. M.; Keshipeddy, S.; Lombardo, M. N.; Hajian, B.; Sochia, A. E.; Alverson, J. B.; Priestley, N. D.; Anderson, A. C.; Wright, D. L. Charged Nonclassical Antifolates with Activity Against Gram-Positive and Gram-Negative Pathogens. *ACS Med. Chem. Lett.* **2016,** *7* (7), 692-696. **DOI:** 10.1021/acsmedchemlett.6b00120

Chapter 3

Reeve, S. M.; Gainza, P.; Frey, K. M.; Georgiev, I.; Donald, B. R.; Anderson, A. C. Protein Design Algorithms Predict Viable Resistance to an Experimental Antifolate. *Proc. Natl. Acad. Sci. U. S. A.* **2014**,*112* (3), 749-754. **DOI**: 10.1073/pnas.1411548112

Chapter 4

Reeve, S. M.; Scocchera, E.; Ferreira, J. J.; G-Dayanandan, N.; Keshipeddy, S.; Wright, D. L.; Anderson, A. C. Charged Propargyl-Linked Antifolates Reveal Mechanisms of Antifolate Resistance and Inhibit Trimethoprim-Resistant MRSA Strains Possessing Clinically Relevant Mutations. *J. Med. Chem.* **2016,** *59* (13), 6493-6500. **DOI**: 10.1021/acs.jmedchem.6b00688

Chapter 5

Reeve, S. M.; Scocchera, E.; G-Dayanandan, N.; Keshipeddy, S.; Krucinska, J.; Hajian, B.; Ferreira, J.; Nailor, M.; Aeschlimann, J.; Wright, D. L.; Anderson, A. MRSA Isolates from United States Hospitals Carry *dfrG* and dfrK Resistance Genes and Succumb to Propargyl-Linked Antifolates. *Cell Chem. Biol.* **2016,** *23* (12), 1458-1467. **DOI**: 10.1016/j.chembiol.2016.11.007

Appendix B Materials and Methods

B.1 Construction, Expression and Purification of Dihydrofolate Reductase

B.1a Generation of Staphylococcus aureus and Mutant Expression Vectors

The generation, expression and purification of DfrB (wild-type *S. aureus* DHFR), DfrB(F98Y), DfrB (H30N) and DfrB (F98Y, H30N) DHFR enzymes have been previously reported[1-3]. DfrA in pET-41a(+), DfrG in pET-41a(+) and DfrK in pET-24a(+) were purchased from Genscript. DfrB(WT) and DfrB(F98Y) in pET-41a(+) constructs were used for the generation of DfrB(H149R) and DfrB(F98Y, H149R) DHFR plasmids via QuikChange Lightening Site-Directed Mutagenesis Kit (Stratagene) using sense primer 5'- CTAGATGAGAAAAATACAATTCCACGTAC-3' and anti-sense primer 5'-CGAATTAAATGTAGAAAGGTACGTGGAAT-3' following the manufacturer's instructions. Mutagenesis was confirmed via Sanger sequencing using primers specific to the T7 promoter.

B.1b Expression and Purification of Dihydrofolate Reductase

The expression and purification of DfrB, DfrB(F98Y), DfrB(H30N), DfrB (F98Y, H30N) in pET-41a(+) has been previously described[1-3].

Expression and Purification of DfrB (H149R) and DfrB (F98Y, H149R)

BL21 (DE3) cells (Invitrogen) were transformed with DfrB (mutants) in pET-41a(+). The cells were grown to mid-log phase (OD_{600}=0.8-1.0) at 37^{o}C, induced with 1 mM IPTG and were allowed to grow for an additional 8 hours at 30^{o}C. One liter cell pellets were lysed using 1x BugBuster (Novagen) and DNase A (ThermoFisher Scientific). Protein was purified using Ni-NTA agarose using a wash buffer containing 25 mM Tris, pH 8.0, 0.4 M KCl, 5 mM Imidazole, 5 mM beta-mercaptoethanol and 5% glycerol and protein was eluted using a buffer containing 25 mM Tris pH 8.0, 0.3 M KCl, 20% glycerol, 0.1 mM

EDTA, 250 mM imidazole and 5 mM beta-mercaptoethanol. Clean protein was pooled and desalted using PD-10 columns (GE Healthcare) into a buffer containing 20 mM Tris pH 8.0, 20% glycerol, 0.1 mM EDTA and 2 mM DTT. Protein was flash frozen and stored at -80^{o}C.

Expression and Purification of DfrA

BL21 (DE3) cells (Invitrogen) were transformed with *dfrA* in pET-41a(+). The cells were grown to mid-log phase (OD_{600}=0.8-1.0) at 37^{o}C, induced with 1 mM IPTG and were allowed to grow for an additional 18 hours at 20^{o}C. Cells were pelleted and resuspended to 30 mL using a buffer containing 0.4 M KCl, 25 mM Tris, pH 8.0, 5 mM beta-mercaptoethanol, 5% glycerol, 100 μg/mL lysozyme, 5 mM imidazole and DNase (Fisher Scientific) and lysed via sonication. Protein was purified using Ni-NTA agarose using a wash buffer containing 25 mM Tris, pH 8.0, 0.4 M KCl, 5 mM Imidazole, 5 mM beta-mercaptoethanol and 5% glycerol and protein was eluted using a buffer containing 25 mM Tris pH 8.0, 0.3 M KCl , 20% glycerol, 0.1 mM EDTA, 250 mM imidazole and 5 mM beta-mercaptoethanol. Clean protein was pooled and desalted into a buffer containing 25 mM Tris pH 8.0, 0.1 mM KCl, 15% glycerol, 0.1 mM EDTA and 2 mM DTT. Protein was flash frozen and stored at -80^{o}C.

Expression and Purification of DfrG

DfrG in pET-41a(+), synthesized by Genscript, was transformed into BL21 (DE3) cells (Invitrogen). The cells were grown to mid-log phase (OD_{600}= 0.8-1.0), induced with 1 mM IPTG and were allowed to grow for an additional 18 hours at 20^{o}C. Cells were pelleted and resuspended to 30 mL using a buffer containing 0.5 M KCl, 50 mM Tris, pH 8.0, 5 mM beta-mercaptoethanol, 5% glycerol, 0.8 mg/mL lysozyme, 5 mM imidazole and a

protease inhibitor tablet (Life Technologies) and lysed with two passes through a French Press. After lysis, the lysate was incubated with DNase and RNase. Protein was purified using Ni-NTA agarose using a wash buffer containing 25 mM Tris, pH 8.0, 0.4 M KCl, 5 mM Imidazole, 5 mM beta-mercaptoethanol and 5% glycerol and protein was eluted using a buffer containing 25 mM Tris pH 8.0, 0.3 M KCl, 20% glycerol, 0.1 mM EDTA, 250 mM imidazole and 5 mM beta-mercaptoethanol. Clean protein was pooled and desalted into a buffer containing 20 mM Tris pH 8.0, 20% glycerol, 0.1 mM EDTA and 2 mM DTT. Protein was flash frozen and stored at -80^{o}C.

Expression and Purification of DfrK

dfrK in pET-24-a(+) was transformed in BL21 (DE3) cells (Invitrogen). The cells were grown to mid-log phase (OD_{600}=0.8-1.0) at 37^{o}C, induced with 1 mM IPTG and were allowed to grow for an additional 18 hours at 20^{o}C. Cells were pelleted and resuspended to 30 mL using a buffer containing 0.4 M KCl, 25 mM Tris, pH 8.0, 5 mM beta-mercaptoethanol, 5% glycerol, 100 μg/mL lysozyme, 5 mM imidazole and DNase (Fisher Scientific) and lysed via sonication. Protein was purified using Ni-NTA agarose using a wash buffer containing 25 mM Tris, pH 8.0, 0.4 M KCl, 5 mM Imidazole, 5 mM beta-mercaptoethanol and 5% glycerol and protein was eluted using a buffer containing 25 mM Tris pH 8.0, 0.3 M KCl , 20% glycerol, 0.1 mM EDTA, 250 mM imidazole and 5 mM beta-mercaptoethanol. Clean protein was pooled and desalted into a buffer containing 25 mM Tris pH 8.0, 0.1 mM KCl, 15% glycerol, 0.1 mM EDTA and 2 mM DTT. Protein was flash frozen and stored at -80^{o}C.

B.2 Biochemical and Inhibitory Evaluation of DHFR Enzymes

B.2a Michaelis-Mentin Kinetics

The Michaelis-Mentin constant (K_M) and V_{max} values for DHF and NADPH were determined by Lineweaver- Burke plots generated by the monitoring the rate of NADPH oxidation by DHFR via absorbance at 340 nm. The reaction was performed at room temperature in buffer containing 20 mM TES pH 7.0, 50 mM KCl, 0.5 mM EDTA, 10 mM beta-mercaptoethanol and 1 mg/mL BSA, and 2 μg/mL enzyme. For DHF, the enzymatic activities were measured using 12.5-100 μM DHF with 20 μM NADPH and for NADPH, the reactions were run with12.5-100 μM NADPH and a constant 50 μM DHF. K_M and V_{max} values were determined by non-linear regression analysis using GraphPad. K_{cat} was determined from V_{max} using Equation 1.

$$K_{cat}=V_{max}/[E_t] \quad (1)$$

$[E_t]$= total enzyme concentration

B.2b IC_{50} Value Determination

IC_{50} values were determined by enzyme inhibition assays via the monitoring the rate of NADPH oxidation by DHFR via absorbance at 340 nm. The reaction was performed at room temperature in buffer containing 20 mM TES pH 7.0, 50 mM KCl, 0.5 mM EDTA, 10 mM beta-mercaptoethanol and 1 mg/mL BSA, 0.1 mM NADPH and 2 μg/mL enzyme. Inhibitor in DMSO was added to the enzyme/NADPH mixture and incubated for 5 minutes prior to the addition of 0.1 mM DHF in 50 mM TES inhibitor volume and concentration is based on conditions at which activity is reduced by 50%. Alternate IC_{50}s (Chapter 2, Table 1) were determined using the same procedure however the 5 minute protein: NADPH: inhibitor incubation was removed. The IC50s were determined using Equations 2 -4.

$$\text{Enzyme Activity } (\mu M/min) = (\Delta A_{340} * 0.041) / (\Delta t \text{ (sec)}/60) \quad (2)$$

$$IC_{50} (\mu M) = (\text{inh vol. } (\mu L) / \% \text{ Inhibition}) * 50/550) * \text{inh conc. (mM)} * 1000 \quad (3)$$

$$\% \text{ inhibition} = 1 - (\text{Activity}_{inh} / \text{Actvity}_{Enz}) * 100 \quad (4)$$

IC50s were converted to K_I through use of Equation 5.

$$K_i = IC_{50} / (100/K_M + 1) \quad (5)$$

B.2c Dissociation Experiments

Steady-state NADPH turnover rate was determined by performing enzyme inhibition assays following 18h of 4°C incubation with 2 μg/mL purified enzyme, 100 μM NADPH and 50 μM inhibitor in buffer containing 20 mM TES, 50 mM KCl, 0.5 mM EDTA, 10 mM beta-mercaptoethanol and 1 mg/mL BSA. The reaction was initiated with 0.1 mM DHF and monitored at an absorbance of 340 nm. The steady-state NADPH rate was extrapolated from data by converting the slope of A_{340} vs time to change in NADPH concentration using a molar extinction coefficient of 6.2x103 $Lmol^{-1}cm^{-1}$.

B.3 Antibacterial Evaluation of Antifolates and Antibiotics

B.3a Minimum Inhibitory Concentration Determination

Minimum Inhibitory Concentrations (MICs) were determined according to the Clinical and Laboratory Standards Institute Guideline's Standard[4] micro-dilution broth assay using a final inoculum of 5×10^5 cfu/mL in Isosensitest Broth (Oxoid) using half-area 96-well plates. The 96-well plate was set-up so that the highest inhibitor, 20μg/mL inhibitor in Isosensitest broth, was loaded into the first column and then a series of 2-fold dilutions were preformed. The final volume of compound in the 96-well plate is 50μL. The inoculum prepared was by diluting the bacteria to an A_{600} =0.130 followed by a 1:100 dilution into sterile isosensitest broth. 50μL of the diluted inoculum was added to each well and the

plate was covered and placed in the incubator for 37°C for 18 hours. MICs were defined as the lowest concentration to visually inhibit bacterial growth and are confirmed by use of Alamar Blue (Life Technologies). UCP compounds (PLAs), trimethoprim, sulfamethoxazole, levofloxacin and linezolid are kept in DMSO, whereas erythromycin was dissolved in ethanol and ciprofloxacin in 0.1N HCl.

B.3b Thymidine Rescue Minimum Inhibitory Concentration Determination

Minimum Inhibitory Concentrations (MICs) were determined according to the Clinical and Laboratory Standards Institute Guideline's Standard micro-dilution broth assay using a final inoculum of 5×10^5 cfu/mL in Isosensitest Broth (Oxoid) using half-area 96-well plates. The 96-well plate was set-up so that the highest inhibitor, 20 μg/mL inhibitor in Isosensitest broth, was loaded into the first column and then a series of 2-fold dilutions were preformed. The final volume of compound in the 96-well plate is 50μL. The inoculum was prepared by diluting the bacteria to an A_{600} =0.130 followed by a 1:100 dilution into sterile isosensitest broth containing 20μg/mL of thymidine (Sigma Aldrich, in water). 50μL of the diluted inoculum was added to each well so that the final thymidine concentration is 10μg/mL and the plate was covered and placed in the incubator for 37°C for 18 hours. MICs were defined as the lowest concentration to visually inhibit bacterial growth and are confirmed by use of Alamar Blue (Life Technologies)

B.3c Sulfamethoxazole Synergy Minimum Inhibitory Concentration Determination

Minimum Inhibitory Concentrations (MICs) were determined according to the Clinical and Laboratory Standards Institute Guideline's Standard micro-dilution broth assay using a final inoculum of 5×10^5 cfu/mL in Isosensitest Broth (Oxoid) using half-area 96-well plates. The 96-well plate was set-up so that the highest inhibitor, 20 μg/mL inhibitor in

Isosensitest broth, was loaded into the first column and then a series of 2-fold dilutions were preformed. The final volume of compound in the 96-well plate is 50μL. The inoculum was prepared by diluting the bacteria to an A_{600} =0.130 followed by a 1:100 dilution into sterile isosensitest broth containing 200 μg/mL or 2 μg/mL of sulfamethoxazole (SMX) for SMX resistant and susceptible strains, respectively (Sigma Aldrich, in DMSO). 50μL of the diluted inoculum was added to each well so that the final thymidine concentration is 100 μg/mL or 1 μg/mL and the plate was covered and placed in the incubator for 37^{o}C for 18 hours. MICs were defined as the lowest concentration to visually inhibit bacterial growth and are confirmed by use of Alamar Blue (Life Technologies)

B.4 UCP1006 Resistance Mutant Generation and Characterization

B.4a Resistance Generation and Selection

Resistant strains were selected by plating 100 μL of overnight culture (approx. 10^{12} CFU/mL) of progenitor strain on Isosensitest (Oxoid) agar plates containing 6x MIC of UCP1006 (MIC=0.0781) and incubated at 37 °C for 18 hours. Single colonies were isolated and the *dfrB* gene was identified by directly sequencing the colony PCR product.

B.4b Direct Colony PCR

The colony was isolated via inoculating loop and lysed using a solution of 1 mg/mL lysostaphin (Sigma Aldrich, in water) and 20 μg/mL proteinase K (Sigma Aldrich, in 0.1 M Tris, pH 7.5). The gene was amplified using:

Forward primer (5'-ATGACTTTATCCATTCTAGTTGC-3')

Reverse: primer (5'-TTATTTTTTACGAATTAAATGTAG-3')

and rTaq Polymerase (Takara) using the following PCR procedure: 2 min denaturation at 95^{o}C, 30 cycles of 95^{o}C denaturation for 30 sec, 55^{o}C annealing for 30 sec, 1 min 72^{o}C

extension followed by a final 10 minute extension at 72°C. PCR products were purified using Promega Wizard SV Gel and PCR Clean Up system, following manufacturers protocol, confirmed on a 1.2% w/v agarose gel visualized with ethidium bromide and sequenced using the sense primer.

B.4c Mutational Frequency Determination

The mutational frequency of UCP1006 was determined by the number of resulting colonies divided by the total inoculum ($1x10^{11}$ CFU/mL) for each progenitor strain. The frequency of the specific mutations was determined by multiplying the mutational frequency for the inhibitor-strain pair by the frequency of sequenced colonies containing the specific mutation.

B.4d Pair-wise Fitness Assay

Relative strain fitness was determined by pair-wise competition assays[5] with trimethoprim as the selective agent. Cell growth was monitored every 20 minutes via A_{600} and the doubling time of the strains was determined by monitoring cell growth in the log phase at an absorbance of 600 nm every 15 minutes for a total of 180 minutes. Fitness was calculated using the following Equation 6.

$$Fitness = \frac{\ln\left(R(24)/R(0)\right)}{\ln\left(S(24)/S(0)\right)} \quad (6)$$

B.4e Doubling-time Growth Curves

1 mL of overnight culture was used to inoculate 50 mL of LB media. Culture was grown at 37°C at 225 RPM and growth was monitored at A_{600} every 30 minutes. The doubling time was determined from the linear portion of the growth curve using Equation 7.

$$Doubling\ Time = \frac{\Delta Time * log2}{\log(Final\ Conc.) - \log(Inital\ Conc.)} \quad (7)$$

B.5 Clinical Strain Characterization

B.5a Clonal Analysis

SpaA-typing was performed by Charles River using Accugenix's AccuGENX-ST service to identify clonality among isolates.

B.5b Genomic DNA Extraction and Next Generation Genomic Sequencing

Genomic DNA was isolated using Promega Wizard Genomic DNA Isolation kit. DNA extracts were quantified using the Quant-iT PicoGreen kit (invitrogen, ThermoFisher Scientific). One ng of genomic DNA was fragmented, adapter sequences attached, size selected and cleaned using the Nextera XT Library Preparation kit (Illumina, Inc.) according to the manufacturer's protocol. Libraries were validated and mean insert length was calculated using a Bioanalyzer High Sensitivity chip (Agilent Technologies). The libraries were sequenced on the MiSeq using v2 2x250 base pair kit (Illumina, Inc). The genome was assembled using CLC Workbench and annotated using the Rast Server[6-8].

B.5c PCR Identification and Sequencing

PCR on gel purified genomic and plasmid DNA was performed to detect the presence of *dfrB*, *dfrA*, *dfrG* and *dfrK* genes.

Table 1 TMP^S and TMP^R DHFR PCR Primers[9]

Enzyme	Primer (5'-3')	Annealing Temp (^oC)
DfrB- Forward	ATGACTTTATCCATTCTAGTTGC	55
DfrB- Reverse	TTATTTTTTACGAATTAAATGTAG	
DfrA-Forward	ACTGACCACTGGGAATACACT	52
DfrA-Reverse	CGACTTCCCAGTTTTCGAATGT	
DfrG-Forward	TTTCTTTGATTGCTGCGATG	55
DfrG-Reverse	CCCTTTTTGGGCAAATACCT	
DfrK-Forward	GAGAATCCCAGAGGATTGGG	55
DfrK-Reverse	CAAGAAGCTTTTCGCTCATAAA	

PCR was performed using rTaq Polymerase (Takara), following standard PCR procedures. PCR product was purified using Promega SV Gel and PCR Clean-Up System, following manufacturers procedures. Purified PCR reactions were run on 1.2% agarose gels and visualized with ethidium bromide using 2-Log Ladder as a size comparator (Thermo Scientific). The sequences were confirmed via Sanger Sequencing using the corresponding forward primer as the sequencing primer.

B.5d Clinical Antibiotic Susceptibility Determination

Susceptibilities were determined using Sensititre Gram Positive plates (Remel, ThermoFisher Scientific) using Mueller-Hinton Broth and an inoculum of $1x10^5$ CFU/mL. The plates were incubated for 18 hours at 37^oC and MICs were colorimetrically determined using Alamar Blue (ThermoFisher Scientific). Susceptible/Intermediate/Resistant designations were made based on CLSI breakpoint standards.

B.6 Crystal Growth Conditions and Protein Crystallography

B.6a Wild-type DHFR Crystal Structures

DfrB: NADPH: UCP1061

Purified SaDHFR at 17 mg/mL was co-crystallized with 2mM NADPH and 1mM UCP1061 in DMSO via hanging drop method. The protein, cofactor and inhibitor mix was incubated on ice for 2 hours. Equal volumes of protein solution were added to an optimized buffer solution containing 0.1M MES, pH 6.5, 0.1M sodium acetate, 13% PEG 10,000 and 12.5% gamma-butrylactone. When stored at 4^{o}C, crystals typically formed within 7 days. Crystals were harvested and frozen in cryo-protectant buffer containing 25% glycerol. Data were collected remotely on beamline X25A at Brookhaven National Laboratories. Data were indexed and scaled using HKL2000. Phaser was used to identify molecular replacement solutions using PDB ID: 3F0Q[10] as a probe. Coot[11] and Phenix[12] were used for structure refinement until acceptable R_{Work} and R_{Free} were achieved.

DfrB: NADPH: UCP1062

Purified SaDHFR at 21 mg/mL was co-crystallized with 2mM NADPH and 1mM UCP1062 in DMSO via hanging drop method. The protein, cofactor and inhibitor mix was incubated on ice for 2 hours. Equal volumes of protein solution were added to an optimized buffer solution containing 0.1M MES, pH 6.0, 0.1M sodium acetate, 13% PEG 10,000 and 12.5% gamma-butrylactone. When stored at 4^{o}C, crystals typically formed within 7 days. Crystals were harvested and frozen in cryo-protectant buffer containing 25% glycerol. Data were collected at the Rigaku HighFlux HomeLab Protein Crystallography X-Ray system at the University of Connecticut. Data was indexed and scaled using d*TREK. Phaser was used to identify molecular replacement solutions for the structures of

Sa(F98Y):NADPH using PDB: 3F0Q as a probe. The programs Coot and Phenix were used for structure refinement until acceptable R_{work} and R_{free} were achieved.

DfrB: NADPH: UCP1070

Purified SaDHFR at 21 mg/mL was co-crystallized with 2mM NADPH and 1mM UCP1070 in DMSO via hanging drop method. The protein, cofactor and inhibitor mix was incubated on ice for 2 hours. Equal volumes of protein solution were added to an optimized buffer solution containing 0.1M MES, pH 6.0, 0.3M sodium acetate, 13% PEG 10,000 and 12.5% gamma-butrylactone. When stored at 4^{o}C, crystals typically formed within 7 days. Crystals were harvested and frozen in cryo-protectant buffer containing 25% glycerol. Data were collected at the Rigaku HighFlux HomeLab Protein Crystallography X-Ray system at the University of Connecticut. Data was indexed and scaled using d*TREK. Phaser was used to identify molecular replacement solutions for the structures of Sa(F98Y):NADPH using PDB: 3F0Q as a probe. The programs Coot and Phenix were used for structure refinement until acceptable R_{work} and R_{free} were achieved.

DfrB: NADPH: UCP1106

Purified SaDHFR at 18 mg/mL was co-crystallized with 2mM NADPH and 1mM UCP1106 in DMSO via hanging drop method. The protein, cofactor and inhibitor mix was incubated on ice for 3 hours. Equal volumes of protein solution were added to an optimized buffer solution containing 0.1M MES, pH 5.5, 0.2M sodium acetate, 17% PEG 10,000 and 12.5% gamma-butrylactone. When stored at 4^{o}C, crystals typically formed within 7 days. Crystals were harvested and frozen in cryo-protectant buffer containing 25% glycerol. Data were collected remotely on beamline 7-1 at Stanford Synchrotron Radiation Lightsource, SLAC National Accelerator Laboratory. Data were indexed and scaled using

HKL2000. Phaser was used to identify molecular replacement solutions using PDB ID: 3F0Q as a probe. Coot and Phenix were used for structure refinement until acceptable R_{Work} and R_{Free} were achieved.

DfrB: NADPH: UCP1175

Purified SaDHFR at 18mg/mL was co-crystallized with 2mM NADPH and 1mM UCP1175 in DMSO via hanging drop method. The protein, cofactor and inhibitor mix was incubated on ice for 3 hours. Equal volumes of protein solution were added to an optimized buffer solution containing 0.1M MES, pH 5.5, 0.2M sodium acetate, 17% PEG 10,000 and 12.5% gamma-butrylactone. When stored at 4^{o}C, crystals typically formed within 7 days. Crystals were harvested and frozen in cryo-protectant buffer containing 25% glycerol. Data were collected remotely on beamline 7-1 at Stanford Synchrotron Radiation Lightsource, SLAC National Accelerator Laboratory. Data were indexed and scaled using HKL2000. Phaser was used to identify molecular replacement solutions using PDB ID: 3F0Q as a probe. Coot and Phenix were used for structure refinement until acceptable R_{Work} and R_{Free} were achieved.

DfrB: NADPH: UCP1191

Purified SaDHFR at 13 mg/mL protein was co-crystallized with 2 mM NADPH and 1 mM UCP1191 in DMSO via the hanging drop method. The mixture of protein and cofactor was incubated on ice for 3 hours. Equal volumes of protein solution were added to an optimized buffer solution containing 0.1 M MES, pH 5.0, 0.3 M sodium acetate, 17% PEG 10,000 and 12.5% gamma-butyrolactone. Crystals were harvested and frozen in cryo-protectant buffer containing 25% glycerol. Data were collected remotely on beamline 14-1 at Stanford Synchrotron Radiation Lightsource, SLAC National Accelerator Laboratory.

Data were indexed and scaled using HKL2000. Phaser was used to identify molecular replacement solutions using PDB ID: 3F0Q as a probe. Coot and Phenix were used for structure refinement until acceptable R_{Work} and R_{Free} were achieved.

B.6b S. aureus F98Y Mutant DHFR Crystal Structures

DfrB (F98Y): NADPH Apo

Sa(F98Y)DHFR was co-crystallized with NADPH using the hanging drop vaporization method. Purified protein (20 mg/mL) was incubated with 2 mM NADPH (Sigma-Aldrich) and for 2h on ice. Equal volumes of the protein: cofactor solution were mixed with an optimized crystallization solution containing 13 % PEG 10,000, 0.1 M sodium acetate, 0.1-0.2 M MES pH 6.0 and 5% gamma-butyrolactone. When stored at 4^{o}C, conditions typically yielded crystals within 7 days. Crystals were frozen in cyro-protectant buffer containing 25 % glycerol. Data were collected at the Rigaku HighFlux HomeLab Protein Crystallography X-Ray system at the University of Connecticut. Data was indexed and scaled using d*TREK. Phaser was used to identify molecular replacement solutions for the structures of Sa(F98Y):NADPH using PDB: 3FQO as a probe. The programs Coot and Phenix were used for structure refinement until acceptable R_{work} and R_{free} were achieved.

DfrB (F98Y): NADPH: UCP1106

DfrB (F98Y) DHFR was co- crystallized with NADPH and UCP1106 using the hanging drop vaporization method. Potein at 14.25 mg/mL was incubated with 1 mM UCP1106 and 2 mM NADPH (Sigma Aldrich) for three hours. It was crystallized in a solution containing 0.1 M MES pH 6.0, 0.2 M Sodium acetate, 13% PEG 10,000 and 20% gamma-butyrolactone. Crystals were frozen with well solution containing 25% glycerol. Data were

collected remotely at Stanford Synchrotron Radiation Lightsource on beamline 7-1. Data was indexed and scaled using HKL2000. Phaser was used to identify molecular replacement solutions for the structures of Sa(F98Y):NADPH:UCP1106 using PDB: 3F0Q as a probe. The programs Coot and Phenix were used for structure refinement until acceptable R_{work} and R_{free} were achieved.

B.6c S. aureus H30N Mutant DHFR Crystal Structures

DfrB (H30N): NADPH: UCP1106

DfrB(H30N) DHFR at 14.25 mg/mL was incubated with 1 mM UCP1106 and 2 mM NADPH for three hours. It was crystallized using the hanging drop method in solution containing 0.1 M MES pH 5.75, 0.3M Sodium acetate, 17% PEG 10,000 and 20% gamma-butyrolactone. Crystals were frozen with well solution containing 25% glycerol.. Data were collected remotely at Stanford Synchrotron Radiation Lightsource on beamline 7-1. Data was indexed and scaled using HKL2000. Phaser was used to identify molecular replacement solutions for the structures of Sa(H30N):NADPH:UCP1106 using PDB: 3F0Q as a probe. The programs Coot and Phenix were used for structure refinement until acceptable R_{work} and R_{free} were achieved.

B.6d S. aureus H30N, F98Y Mutant DHFR Crystal Structures

DfrB (H30N, F98Y): NADPH: UCP1106

Sa(F98Y/H30N) DHFR at 21 mg/mL was incubated with 1 mM UCP1106 and 2 mM NADPH for three hours. It was crystallized using the hanging drop vaporization method in a solution containing 0.1 M MES, pH 6.0, 0.2 M Sodium acetate and 13% PEG 10,000 and 20% gamma-butyrolactone. Crystals were frozen using well solution containing 25% glycerol. Data were collected remotely at Stanford Synchrotron Radiation Lightsource on

beamline 7-1 and indexed and scaled using HKL2000. Phaser was used to identify molecular replacement solutions for the structures of Sa(H30N, F98Y):NADPH:UCP1106 using PDB: 3F0Q as a probe. The programs Coot and Phenix were used for structure refinement until acceptable R_{work} and R_{free} were achieved.

B.6e S. aureus V31L, F98Y Mutant DHFR Crystal Structures

DfrB (V31L, F98Y):NADPH: UCP1021

Sa(V31L, F98Y)DHFR was co-crystallized with NADPH and UCP1021 using the hanging drop vaporization method. Purified protein (20 mg/mL) was incubated with 2 mM NADPH (Sigma-Aldrich) and 1 mM inhibitor in DMSO for 2h on ice. Equal volumes of the protein: cofactor: inhibitor solution were mixed with an optimized crystallization solution containing 13 % PEG 10,000, 0.1 M sodium acetate, 0.1-0.2 M MES pH 6.0 and 5% gamma-butyrolactone Crystals were frozen in cyro-protectant buffer containing 25 % glycerol. High-resolution data were collected on the X4A Beamline at Brookhaven National Laboratories. Data for Sa(V31L, F98Y)DHFR:NADPH were indexed and scaled using HKL2000. Phaserwas used to identify molecular replacement solutions for the structures of Sa(V31L, F98Y)DHFR:NADPH and Sa(F98Y):NADPH using PDB: 3F0U The programs Coot and Phenix were used for structure refinement until acceptable R_{work} and R_{free} were achieved.

B.7 References

1. Frey, K. M.; Liu, J.; Lombardo, M. N.; Bolstad, D. B.; Wright, D. L.; Anderson, A. C. Crystal Structures of Wild-Type and Mutant Methicillin-Resistant Staphylococcus Aureus Dihydrofolate Reductase Reveal an Alternate Conformation of NADPH That May Be Linked to Trimethoprim Resistance. *J. Mol. Biol.* **2009**, *387* (5), 1298–1308.
2. Frey, K. M.; Lombardo, M. N.; Wright, D. L.; Anderson, A. C. Towards the Understanding of Resistance Mechanisms in Clinically Isolated Trimethoprim-Resistant, Methicillin-Resistant Staphylococcus Aureus Dihydrofolate Reductase. *J. Struct. Biol.* **2010**, *170* (1), 93–97.
3. Frey, K.; Viswanathan, K.; Wright, D.; Anderson, A., Prospectively Screening Novel Antibacterial Inhibitors of Dihydrofolate Reductase for Mutational Resistance. *Antimicrob. Agents and Chemother.* **2012**, *56*, 3556-3562.
4. Wayne, P. A. (2014). CLSI Performance standard of Antimicrobial Susceptibility Testing: Twenty-fourth International Supplement. CLSI Doc. M100-S24. Clin. Lab. Stand. Inst.
5. Lenski, R. Experimental studies of pleiotropy and epistasis in *Escerichia coli.* I. Variation in competitive fitness among mutants resistant to virus T4. *Evolution*. **1988**, *42* (3), 425-32.
6. Aziz, R. K.; Bartels, D.; Best, A. A.; DeJongh, M.; Disz, T.; Edwards, R. A.; Formsma, K.; Gerdes, S.; Glass, E. M.; Kubal, M.; et al. The RAST Server: rapid annotations using subsystems technology. *BMC Genomics*. **2008** *9*, 75.
7. Brettin, T.; Davis, J. J.; Disz, T.; Edwards, R. A.; Gerdes, S.; Olsen, G. J.; Olson, R.; Overbeek, R.; Parrello, B.; Pusch, G. D.; et al. RASTtk: a modular and extensible implementation of the RAST algorithm for building custom annotation pipelines and annotating batches of genomes. *Sci. Rep.* **2015**, *5*.
8. Overbeek, R., Olson, R., Pusch, G. D., Olsen, G. J., Davis, J. J., Disz, T., Edwards, R. A., Gerdes, S., Parrello, B., Shukla, M., et al. (2014). The SEED and the Rapid Annotation of microbial genomes using Subsystems Technology (RAST). Nucleic Acids Res. *42*, D206–D214.
9. Bergmann, R.; Van Der Linden, M.; Chhatwal, G. S.; and Nitsche-Schmitz, D. P. Factors that cause trimethoprim resistance in Streptococcus pyogenes. *Antimicrob. Agents Chemother.* **2014** *58*, 2281–2288.
10. Frey, K. M.; Georgiev, I.; Donald, B. R.; Anderson, A. C. Predicting Resistance Mutations Using Protein Design Algorithms. *Proc. Natl. Acad. Sci. U. S. A.* **2010**, *107* (31), 13707–13712.
11. Emsley, P., and Cowtan, K. Coot: model-building tools for molecular graphics. *Acta Crystallogr. Sect. D Biol. Crystallogr*. **2004**, *60*, 2126–2132.
12. Adams, P. D., Afonine, P. V, Bunkóczi, G., Chen, V. B., Davis, I. W., Echols, N., Headd, J. J., Hung, L.-W., Kapral, G. J., Grosse-Kunstleve, R. W., et al. PHENIX: a comprehensive Python-based system for macromolecular structure solution. *Acta Crystallogr. Sect. D Biol. Crystallogr.* **2010**, *66*, 213–221.

Appendix C Crystallographic Data Collection and Refinement Statistics

C.1 Structures Presented in Chapter 2

Table C1 Data Collection and Refinement Statistics for Pyridine PLAs

	Sa(WT):NADPH: UCP1061	Sa(WT):NADPH: UCP1062	Sa(WT):NADPH: UCP1070
PDB ID	4XEC	4TU5	N/A
Space group	*$P6_122$*	*$P6_122$*	*$P6_122$*
No. monomers in asymmetric unit	1	1	1
Unit cell (*a, b, c* in Å)	78.90, 78.90, 108.12	79.14, 79.14, 108.99	79.048, 079.048, 109.04
Resolution (Å)	31.89-2.69	58.02-2.16	50-1.66
Completeness % (last shell, %)	99.97 (98.6)	99.8 (100)	99.08
Unique reflections	5,929	11,493	34, 438
Redundancy (last shell)	18.2 (17.4)	12.94 (13.26)	14.3 (14.1)
Rsym, (last shell)	0.160 (0.428)	0.154 (0.437)	0.109(0.699)
$\langle I/\sigma \rangle$ (last shell)	38.6 (9.0)	8.8 (3.6)	35.1 (4.5)
R-factor/Rfree	0.1564, 0.2327	0.1990 , 0.2495	0.2241, 0.2384
No. of atoms (protein, ligands, solvent)	1,398	1,496	1,517
Rms deviation bond lengths (Å), angles (deg)	0.008, 1.343	0.008, 1.248	0.011, 1.980
Average B factor for protein ($Å^2$)	30.22	30.75	24.17
Average B factor for ligand ($Å^2$)	26.89 (NADPH) 33.49 (DRG)	25.64 (NADPH) 35.86 (DRG)	16.92 (NADPH) 23.89 (DRG)
Average B factor for solvent molecules ($Å^2$)	28.17	39.06	27.13
Residues in most favored regions (%)[a]	96.79	97.44	98.75
Residues in additional allowed regions (%)[a]	3.21	2.56	1.25
Residues in disallowed regions (%)[a]	0	0	0
Collection Location	Brookhaven National Lab NSLS X25 Beamline	Rigaku HighFlux HomeLab	

Table C2 Data Collection and Refinement Statistics for Carboxylate PLAs

	Sa(WT):NADPH: UCP1006	Sa(WT):NADPH: UCP1175	Sa(WT):NADPH: UCP1191
PDB ID	5HF0	5HF2	5JG0
Space group	*$P6_122$*	*$P6_122$*	*$P6_122$*
No. monomers in asymmetric unit	1	1	1
Unit cell (*a, b, c* in Å)	79.09, 79.09, 107.93 90.0, 90.0, 120.0	79.02, 79.02, 108.25 90.0, 90.0, 120.0	78.86, 78.86, 106.43 90.0, 90.0, 120.0
Resolution (Å)	32.65-2.24 (2.28-2.24)	25.15-1.81 (1.87-1.81)	39.44-1.88 (1.91-1.88)
Completeness % (last shell, %)	100 (99.9)	99.8 (100)	99.75 (97.0)
Unique reflections	10,059	18,798	16, 498
Redundancy (last shell)	14 (14.2)	12.32 (12.03)	16.7 (17.4)
Rsym, (last shell)	0.055 (0.144)	0.110 (0.644)	0.107 (0.483)
$<I/\sigma>$ (last shell)	68.5 (31.9)	11.7 (2.3)	41.2 (5.52)
R-factor/Rfree	0.1703/ 0.2167	0.1991/0.2322	0.1765/ 0.2172
No. of atoms (protein, ligands, solvent)	1,499	1,489	1,458
Rms deviation bond lengths (Å), angles (deg)	0.008, 1.912	0.009. 1.810	0.007, 1.238
Average B factor for protein ($Å^2$)	22.34	28.01	29.54
Average B factor for ligand ($Å^2$)	17.46 α-NADPH 16.91 β-NADPH 31.29 Inhibitor	24.65 α-NADPH 24.93 Inhibitor	25.34 β-NADPH 34.66 Inhibitor
Average B factor for solvent molecules ($Å^2$)	25.25	35.10	35.74
Residues in most favored regions (%)[a]	96.86	98.73	98.12
Residues in additional allowed regions (%)[a]	3.14	1.27	1.88
Residues in disallowed regions (%)[a]	0	0	0
Collection Location	SSRL Beamline 7-1	Rigaku HighFlux-007	SSRL Beamline 7-1

C.2 Structures Presented in Chapter 3

Table C3 Data Collection and Refinement Statistics for K* Predicted Mutants

	Sa(V31L,F98Y) Apo	Sa (F98Y) Apo
PDB ID		
Space group	*P6$_1$22*	*P6$_1$22*
No. monomers in asymmetric unit	1	1
Unit cell (*a, b, c* in Å)	79.335, 79.335, 107.553	79.26, 79.26, 107.42
Resolution (Å)	68.706- 1.559	42.30-2.04 (2.51-2.04)
Completeness % (last shell, %)	99.8 (98.6)	98.7 (98.5)
Unique reflections	29,153	13,132
Redundancy (last shell)	13.7 (13.5)	10.22 (10.44)
Rsym, (last shell)		0.070 (0.340)
$\langle I/\sigma \rangle$ (last shell)	31.7 (20.0)	16.9 (5.6)
R-factor/Rfree	0.1993/ 0.2221	0.1752/ 0.2330
No. of atoms (protein, ligands, solvent)	1,524	1,446
Rms deviation bond lengths (Å), angles (deg)	0.007, 1.275	0.007, 1.205
Average B factor for protein (Å^2)	20.68	28.75
Average B factor for ligand (Å^2)	13.14 (NADPH)	21.11 (NADPH)
Average B factor for solvent molecules (Å^2)	32.08	35.18
Residues in most favored regions (%)[a]	98.15	98.10
Residues in additional allowed regions (%)[a]	1.85	1.90
Residues in disallowed regions (%)[a]	0	0
Collection Location	BNL X4A	Rigaku MicroMax HomeFlux

C.3 Structures Presented in Chapter 4

Table C4 Data Collection and Refinement Statistics for Mutant DHFR with UCP1106

	Sa(F98Y):NADPH: UCP1106	Sa(H30N):NADPH: UCP1106	Sa(H30N, F98Y): NADPH: UCP1106
PDB ID	5ISP	5IST	5ISQ
Space group	*$P6_122$*	*$P6_122$*	*$P6_122$*
No. monomers in asymmetric unit	1	1	1
Unit cell (*a, b, c* in Å)	79.13, 79.13, 107.41	79.07, 79.07, 108.42	78.99, 78.99, 108.69
Resolution (Å)	28.85-1.84	31.96-1.72	28.95-1.90
Completeness % (last shell, %)	99.9 (100)	99.05	99.95
Unique reflections	17,979	21,572	16,379
Redundancy (last shell)	8.2 (8.3)	9.3 (9.1)	9.1 (9.1)
Rsym, (last shell)	0.105 (0.516)	0.108 (0.590)	0.095 (0.400)
$\langle I/\sigma \rangle$ (last shell)	48.4 (5.16)	36.0 (4.36)	44.6 (7.82)
R-factor/Rfree	0.1803/ 0.2096	0.1872/ 0.2305	0.1798/ 0.2219
No. of atoms (protein, ligands, solvent)	1508	1576	1478
Rms deviation bond lengths (Å), angles (deg)	0.08, 1.251	0.07, 1.872	0.008, 1.239
Average B factor for protein ($Å^2$)	29.39	20.62	25.64
Average B factor for ligand ($Å^2$)	21.64 NADPH 39.87 Inhibitor	14.89 tNADPH 14.38 β-NADPH 26.46 Inhibitor	18.97 NADPH 31.28 Inhibitor
Average B factor for solvent molecules ($Å^2$)	36.36	29.22	31.72
Residues in most favored regions (%)[a]	97.56	98.15	98.10
Residues in additional allowed regions (%)[a]	2.44	1.85	1.90
Residues in disallowed regions (%)[a]	0	0	0
Collection Location	SSRL 7-1	SSRL 7-1	SSRL 7-1